

Editorial Board of the
International Journal of Mechanics and Control

Published by Levrotto&Bella – Torino – Italy E.C.

Honorary editors

Guido Belforte

Kazy Yamafuji

Editor: Andrea Manuello Bertetto

General Secretariat: Elvio Bonisoli

Atlas Akhmetzyanov
*V.A.Trapeznikov Institute of Control Sciences
of Russian Academy of Sciences
Moscow – Russia*

Domenico Appendino
*Prima Industrie
Torino – Italy*

Kenji Araki
*Saitama University
Shimo Okubo, Urawa
Saitama – Japan*

Guido Belforte
*Technical University – Politecnico di Torino
Torino – Italy*

Bruno A. Boley
*Columbia University,
New York – USA*

Marco Ceccarelli
*LARM at DIMSAT
University of Cassino
Cassino – Italy*

Amalia Ercoli Finzi
*Technical University – Politecnico di Milano
Milano – Italy*

Carlo Ferraresi
*Technical University – Politecnico di Torino
Torino – Italy*

Anindya Ghoshal
*Arizona State University
Tempe – Arizona – USA*

Nunziatino Gualtieri
*Space System Group
Alenia Spazio
Torino – Italy*

Alexandre Ivanov
*Technical University – Politecnico di Torino
Torino – Italy*

Giovanni Jacazio
*Technical University – Politecnico di Torino
Torino – Italy*

Takashi Kawamura
*Shinshu University
Nagano – Japan*

Kin Huat Low
*School of Mechanical and Aerospace Engineering
Nanyang Technological University
Singapore*

Andrea Manuello Bertetto
*University of Cagliari
Cagliari – Italy*

Stamos Papastergiou
*Jet Joint Undertaking
Abingdon – United Kingdom*

Mihailo Ristic
*Imperial College
London – United Kingdom*

János Somló
*Technical University of Budapest
Budapest – Hungary*

Jozef Suchy
*Faculty of Natural Science
Banska Bystrica – Slovakia*

Federico Thomas
*Instituto de Robótica e Informática Industrial
(CSIC-UPC)
Barcelona – Espana*

Furio Vatta
*Technical University – Politecnico di Torino
Torino – Italy*

Vladimir Viktorov
*Technical University – Politecnico di Torino
Torino – Italy*

Kazy Yamafuji
*University of Electro-Communications
Tokyo – Japan*

*Official Torino Italy Court Registration
n.5390, 5th May 2000*

*Deposito presso il Tribunale di Torino
numero 5390 del 5 maggio 2000*

Direttore responsabile:

Andrea Manuello Bertetto

International Journal of Mechanics and Control

Editor: Andrea Manuello Bertetto

***Honorary editors: Guido Belforte
Kazy Yamafuji***

General Secretariat: Elvio Bonisoli

The Journal is addressed to scientists and engineers who work in the fields of mechanics (mechanics, machines, systems, control, structures). It is edited in Turin (Northern Italy) by Levrotto&Bella Co., with an international board of editors. It will have not advertising.

Turin has a great and long tradition in mechanics and automation of mechanical systems. The journal would will to satisfy the needs of young research workers of having their work published on a qualified paper in a short time, and of the public need to read the results of researches as fast as possible.

Interested parties will be University Departments, Private or Public Research Centres, Innovative Industries.

Aims and scope

The *International Journal of Mechanics and Control* publishes as rapidly as possible manuscripts of high standards. It aims at providing a fast means of exchange of ideas among workers in Mechanics, at offering an effective method of bringing new results quickly to the public and at establishing an informal vehicle for the discussion of ideas that may still in the formative stages.

Language: English

International Journal of Mechanics and Control will publish both scientific and applied contributions. The scope of the journal includes theoretical and computational methods, their applications and experimental procedures used to validate the theoretical foundations. The research reported in the journal will address the issues of new formulations, solution, algorithms, computational efficiency, analytical and computational kinematics synthesis, system dynamics, structures, flexibility effects, control, optimisation, real-time simulation, reliability and durability. Fields such as vehicle dynamics, aerospace technology, robotics and mechatronics, machine dynamics, crashworthiness, biomechanics, computer graphics, or system identification are also covered by the journal.

Please address contributions to

Prof. Guido Belforte
Prof. Andrea Manuello Bertetto
PhD Eng. Elvio Bonisoli

*Dept. of Mechanics
Technical University - Politecnico di Torino
C.so Duca degli Abruzzi, 24.
10129 - Torino - Italy - E.C.*

www.jomac.it
e_mail: jomac@polito.it

Subscription information

Subscription order must be sent to the publisher:

*Libreria Editrice Universitaria
Levrotto&Bella
C.so Luigi Einaudi 57/c – 10129 Torino – Italy*

www.levrotto-bella.net
e_mail: info@levrotto-bella.net
ph.: +39 011 4275423
mob.: +39 328 5369063
fax: +39 011 4275425

AN EXPERIMENTAL TEST VALIDATION OF A NEW PLANETARY TRANSMISSION

Gani Balbayev * Marco Ceccarelli ** Konstantin Ivanov *

* Almaty University of Power Engineering and Telecommunication, Kazakhstan

** University of Cassino and South Latium, Italy

ABSTRACT

This paper presents experimental tests of a planetary gear transmission with two degrees of freedom. The aim of the paper is to outline experimentally output characteristics of a planetary gear transmission. The experimental set up consists of torsionmeters, encoder, amplifiers, and acquisition cards with proper virtual instruments in Lab View Software. Results are discussed to characterize typical outputs of the investigated gearing system with planetary gear transmission.

Keywords: Transmissions, Gears, Planetary Gearbox, Experimental Tests, Performance Analysis

1 INTRODUCTION

The paper presents an experimental test with a prototype of a new planetary gear transmission. The gear mechanism is designed to obtain smooth reduction ratio depending of a load on the output shaft. Planetary transmissions can be used in a large variety of mechanical systems, since they can generate variable gear ratio as useful in mechanisms where smoothly changing reduction ratio is required, like for example in tractors, automatic equipments, textile industries, wind turbines, automobile industries, conveyors, draglines, bridges and many other machineries.

It offers you a template for paper layout, and describes points you should notice before you submit your papers. Planetary gear transmissions are commonly used in applications where a large speed reduction is required as pointed out in [6] and [7]. Several design solutions have been proposed in the literature, like for example in [1], [4], [5] and [10]. For example a cam-based infinitely variable

transmission can be used for continuously variable transmission, which can also achieve any transmission ratio, [3]. This transmission consists of two main parts, namely a cam mechanism and a planetary gear set. Theoretical and experimental study of pushing CVT dynamics is presented in [1], where the work is focused to design advanced CVT systems with improved efficiency. A mechanism with a planetary gear set and a torque converter is designed as a continuously variable transmission in [2]. This mechanism has two degrees of freedom and makes use of an external torque to start the movement, [2].

A theoretical and experimental investigation of sidebands of planetary gear sets is described in [8]. Here the validity is demonstrated through an experimental study. In this study an experimental set up and measurement system are developed to perform sideband measurements by using gear sets that are qualitatively different in terms of their predicted sideband outcome.

An experimental test methodology for measurement of spur gear efficiency under high-speed and variable torque conditions is described in [9]. In this study test methodology has been developed with a precision torque system.

In this paper an experimental test is considered for a planetary gear set which can generate a smooth reduction ratio. The contribution of this paper is on the study of the effect of the output parameters of planetary gear train through experimental tests.

Contact author: Gani Balbayev

Almaty University of Power Engineering and
Telecommunication, Baitursynov str.,126, Almaty,
Kazakhstan

E-mail: gani_b@mail.ru

2 EXPERIMENTAL LAYOUT

A scheme for the proposed test-bed and experimental test-bed with a planetary transmission is presented in Figure 1 and 2. In Figure 2 and 3 (a, b) views of system set up are shown together with a planetary gear transmission. The planetary gear transmission is a new solution with two degrees of freedom. Each gear in the planetary transmission has same module of 1 mm. The output and input shafts have same diameter of 14 mm. The overall planetary transmission is sized with a high of 130 mm and a longitudinal size of 180 mm. The motor, torsiometers, encoder, inverter, amplifiers, data acquisition cards and gearbox with braking system have been used for experimental tests.

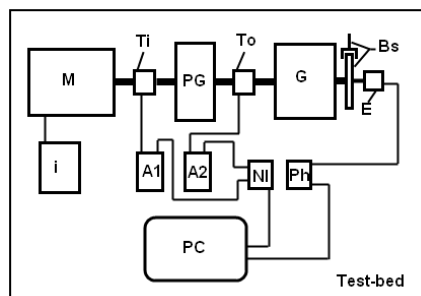


Figure 1 A scheme for the test-bed with planetary transmission, Figure 2 and Table I: (M-motor; Ti and To-torsiometer; PG-planetary gearbox; G-gearbox; Bs-braking system; E-encoder; i-inverter; A1 and A2-amplifier; NI and Ph-data acquisition card).

A scheme of the experimental lay-out is shown in Figure 1. For experimental tests Lab View software has been used with NI USB 6009 acquisition card, [12]. Torsiometer Ti with the amplifier have been used in order to determine torque changes on the input shaft. Torsiometer To with the amplifier A2 have been used in order to monitor torque on the output shaft. The motor with the inverter have been used in order to give the motion to the system. An encoder with Phidget 1047 acquisition card has been used to monitor the angle of the shaft, [11]. A gear box G with the braking system Bs have been used in order to give a load to the system. Reduction ratio of the gearbox G is 10:1. Main characteristics of the components in this test-bed are given in Table I.

Table I Characteristics of the components of the test-bed in Figures 1 and 2.

Components	Characteristics
Motor	1.5 watt
Torsiometer	Range from +/-5 to +/-7000 Nm
Planetary gearbox	Two DOFs
Gear box	Reduction ratio 10:1
Braking system	Hydraulic
Encoder	360 ^o Continuous
Data acquisition cards	NI USB 6009; Phidget 1047
Inverter	3-phase 200-240V, 50/60Hz
Amplifier	220V, out-5v
Software	Lab View 2010
Components	Characteristics



Figure 2 A view of the test-bed for mechanical transmission: (a) general view (1-motor; 2 and 4- torsiometer; 3-planetary transmission; 5-gearbox; 6-brake disk; 7-brake caliper; 8-encoder; 9-inverter; 10 and 11-amplifier; 12-NI data acquisition card; 13-Phidget data acquisition card; 14-brake lever).

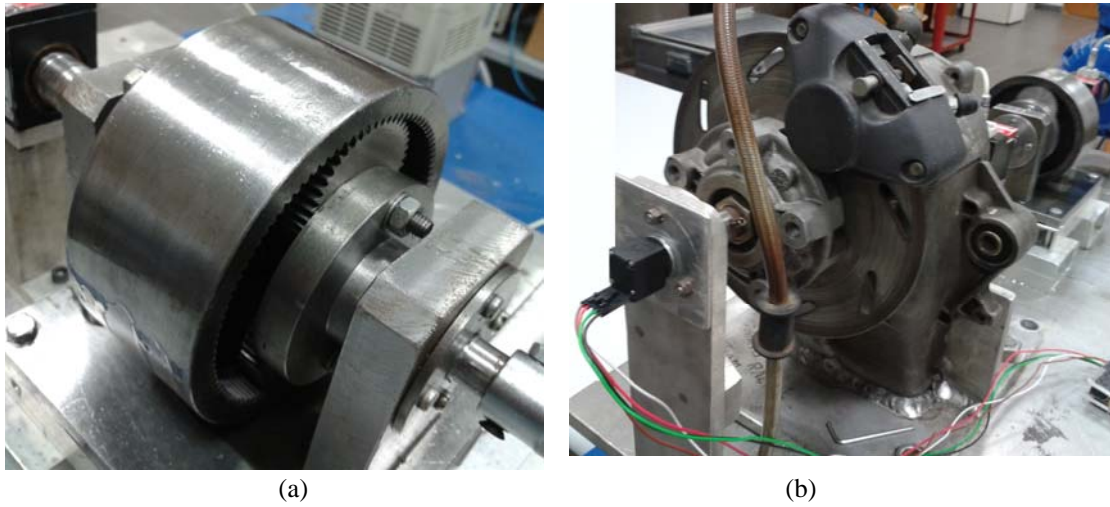


Figure 3 A view of the test-bed: (a) planetary gear box in zoomed view;
(b) braking system with encoder in zoomed view.

3 EXPERIMENTAL RESULTS

Experimental tests have been carried out on the mechanical test-bed in Figures 2 and 3 (a, b). In this paper several cases of experimental tests are reported. An experimental test has been done by braking the output shaft in order to give different values of loads from 0 up to full braking of shaft. Results of tests are reported in Figures 3-6. An input constant speed has been given to the system during the test. The value of the speed is approximately 460 rpm. The torque of the motor is 3.5 Nm. Different values of torques have been applied to the output shaft of the planetary transmission by using a braking system.

Figure 3 shows the torque changes on the input shaft. The experimental test has been started at 6 sec. up to 13 sec. the system has been worked without any load. The small torque approximately of 0.1 Nm is appeared due to due mainly to friction at gear teeth contacts. When to the system has been given a torque, from 13 sec. up to 22 sec., the torque on the input shaft increased up to 0.4 Nm. In the next step of the test, the output shat is stopped by giving a maximum load. The torque on the input shaft is increased approximately up to 0.7 Nm. The peak at 22 sec. on the plot in Figure 3 shows a shock due to a rapid variation of load.

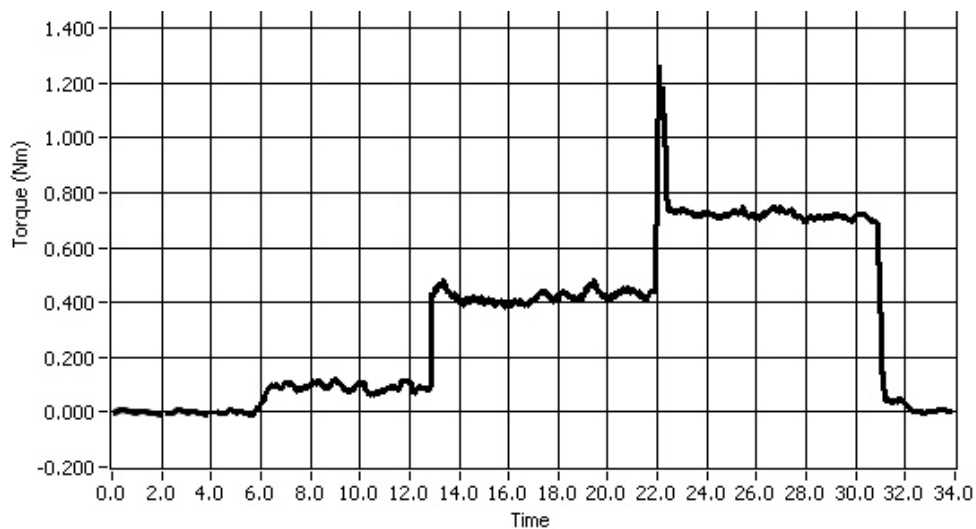


Figure 4 Measured torque on the input shaft during a test.

In Figure 4 is shown a plot of the measured torque on the output shaft. From 6 sec. to 13 sec. the system worked without applying a load. The torque of 0.5 Nm is appeared due to friction at gear teeth contacts. From 13 sec. up to 22.5 sec. to the system has been given the output constant torque of 1.5. From 22.5 sec. up to 31 sec. to the system has been given a maximum torque of 2.5 Nm and the output shaft stops, but input shaft can rotate due to the two degrees of freedom. The peaks on the plot in Figure 4 shows a shock due to a rapid variation of the load. The angular velocity of the output shaft is presented in Figure 5. The maximum speed is reached value of 460 rpm in 2 seconds. This is, because the test-bed joints have backlash and the test-bed gearbox (No 5, Figure 2 a) with gear ratio 10:1 also has backlash. The speed decreased up to 130 rpm at 13 sec., when to the system has been given an output torque of 1.5 Nm. In the plot speed with 0 rpm shows that the output shaft is stopped by giving the maximum torque of 2.5 Nm. Considering these results the output speed depends on the applied torque to the output shaft and input shaft can be continuously in rotation due to the two degrees of freedom. The plot in Figure 6 gives clear picture of the work of transmission with two degrees of freedom which can change reduction ratio depending on the output load. In Figure 6 the marked points with letters A, B and C correspond to the output torques in Figure 5 0.5, 1.5 and 2.5 Nm and to the angular speeds in Figure 5 460, 130 and 0 rpm relatively. The curve in Figure 6 shows the smoothly changing reduction ratio depending on the output load.

CONCLUSION

A planetary gear transmission with two degrees of freedom has been studied through experimental tests. Experiments have been carried out to measure the angular velocity of the output shaft, torques on the input and output shafts by braking the output shaft in order to give different values of load. The transmission with two degrees of freedom can save motor from suddenly change of output torques. The motor works with constant speed at any external applied torque. The results also show that the gear box smoothly changes the reduction ratio at constant input speed. This mechanism can be used in applications where it is necessary to reduction ratio.

ACKNOWLEDGMENTS

The first author acknowledges JSC Center of International Program "Bolashak" of Republic of Kazakhstan for supporting his PhD study and research at LARM in Cassino in A.Y. 2012-2013.

REFERENCES

- [1] Carbone G., Mangialardi L., Bonsen B., Tursi C. and Veenhuizen P. A., CVT dynamics: Theory and Experiments. *Mechanism and Machine Theory*, Vol. 1, No. 4, pp. 409-428, 2007.
- [2] Crockett J. S., Shiftless continuously-aligning transmission, U.S. 4,932,928, Cl. F16H 47/08U.S.Cl. 475/51; 475/47, 1990.
- [3] Derek F. L. and Dennis W. H., The Operation and Kinematic Analysis of a Novel Cam-based Infinitely Variable Transmission. *ASME 2006 International Design Engineering Technical Conferences and Information in engineering conference*, Vol. 1, Philadelphia, pp. 469-474. 2006.
- [4] Ivanov K., Design of Toothed Continuously Variable Transmission in the Form of Gear Variator. *Balkan Journal of Mechanical Transmissions (BJMT)*. Vol. 2, No. 1, pp. 11-20. 2012.
- [5] Ivanov K. *Force Adaptation of Two-Mobile Gear Mechanisms*. Almaty Kazgos INTI Publications, (in Russian), 2001.
- [6] Kaharman A. and Ding H. A Methodology to Predict Surface Wear of Planetary Gears under Dynamic Conditions. *Mechanics Based Design of Structures and Machines*, Vol. 38No. 4, pp. 493-515 2010.
- [7] Patel, P., *Design and Analysis of Differential Gearbox*. U.V. Patelcollege of Engineering, Kherva: Ganpat University Publications, 2009.
- [8] Inalpolat M. and Kahraman A., A theoretical and Experimental Investigation of Modulation Sidebands of Planetary Gear Sets. *Science Direct, Journal of Sounds and Vibration*, Vol. 323, No. 3, pp. 677-696, 2009.
- [9] Petry-Johnson T., Kahraman A., Anderson E. and Chase D., Experimental Investigation of Spur Gear Efficiency. *Proceedings of the ASME 2007 International Design Engineering Technical Conferences and Computers and Information in Engineering Conference*, Las Vegas, Vol. 7, pp. 747-758, 2007.
- [10] Yaghoubi M. and Mohtasebi S., Design and Simulation of a New Bevel Multi-Speed Gear box for Automatic Gearboxes. *Science Journal Report and Opinion*, Vol. 2, No. 3, pp. 1-7. 2010.
- [11] EN - Rotary Optical Encoder, Bourns, Datasheet. Available from <http://www.bourns.com> Accessed: 2013-03-12.
- [12] NI USB-6008/6009 User Guide and Specifications, National Instruments. Available from <http://www.ni.com/manuals> Accessed: 2013-03-12.

DESIGN AND SIMULATION OF AN ARTICULATED LEG FOR HEXAPOD ROBOTS

Nestor Eduardo Nava Rodríguez * Giuseppe Carbone** Marco Ceccarelli**

*Robotics Lab.

Carlos III University, Calle Universidad, 30, 28911 Leganes (Madrid), Spain

**LARM: Laboratory of Robotics and Mechatronics

DiMSAT – University of Cassino, Via Di Biasio 43 - 03043 Cassino (Fr), Italy

ABSTRACT

This paper presents a new design solution of a robotic leg for hexapod robots with low-cost easy-operation features. The leg design is based on a linkage mechanism, which operation feasibility has been analyzed through dynamic simulation of basic operation modes. The new leg design is characterized by bio-inspired operation and a linkage-based driving mechanism that gives versatility in terms of operation modes by using only few actuating motors. The mechanical design has been completed by addressing attention to robot operation, in particular control system design and operation programming. Results of simulation of controlled motions are reported to show feasibility and peculiarities of the proposed design.)

Keywords: Robotics, Mobile Robots, Hexapod, Design, Simulation.

1 INTRODUCTION

Walking machines have been proposed as alternative transportation machines with the aim to overpass the limits of wheeled systems by looking at legged solutions in nature, [1-3]. Nevertheless, only in a recent past efficient walking machines have been conceived, designed, and built with performances that are suitable for practical applications, for example [4-8]. Biped, quadruped and hexapod as well as humanoid robots have been developed in research centres and universities around the world in the last part of 20-th century.

These apparatus have been conceived as machines that can help human beings in dangerous or tedious tasks, such as, for example transportation of military equipment, [9], mine detection and grass cutting, [10-11], in-pipe inspection, [12-13], or planetary exploration, [14].

Mobile robots present different architectures since they can be designed either with crawlers, wheels or with biologically inspired legs, [15-17]. The legged walking machines can be slow and present more difficulty to design and operate than the wheeled or crawled. Nevertheless, legged robots perform suitable operations in rough terrains exploration, where obstacles of any size can appear, as outlined in [18]. In fact, the use of wheels or crawlers limits the size of the obstacle that the robot can overcome while legged machines can overcome obstacles that are comparable with the leg sizes.

There is also a third type of walking machine, which is called hybrid robot because its mechanism contains both legs and wheels. This type of walking machine may range from wheeled devices to true walking machines with a set of wheels. Therefore, legs are used to overcome particularly difficult obstacles and wheels are used to enhance the speed when moving on flat terrain. Moreover, the leg mechanisms can provide robot suspension during wheeled operation by applying a proper control loop.

A hexapod robot is a mechanical vehicle that walks by means of six legs. Some examples are considered in the following significant prototypes of hexapod robots.

Contact author: Nestor Eduardo Nava Rodríguez¹

¹ Calle Universidad, 30, 28911 Leganes (Madrid), Spain

Email: nnavar@arquimea.com
carbone@unicas.it
ceccarelli@unicas.it

A multi-legged robot with articulated body that is named as SLAIR2, has been developed at the Fraunhofer Institute for Factory Operation Ottovon-Guericke University in Magdeburg, Germany [19]. This robot consists of three modular segments that are linked through two degrees of freedom (DOF) joints and 6 legs. Based on anatomy of ants and leg coordination of stick insects, a BILL-Ant-p robot was designed by William Lewinger [20]. This is an actively compliant 18-DOF hexapod robot with six force-sensing feet; a 3-DOF neck with head; and actuated mandibles with force-sensing for a total of 28 degrees of freedom. RHex robot has been developed at Boston Dynamics, [21]. RHex platform includes six legs that are equipped with a single rotary actuator at each hip. Legs are made of compliant materials to produce running gaits. The leg modules are controlled from a central computer, which elaborates user commands or sensor feedback to decide how the legs will move. It is capable of achieving a wide variety of dynamically dexterous tasks, such as walking, running, leaping over obstacles, climbing stairs. Two on-board batteries allow a continuous operation of about 10 min. Then, the project has been mostly focused on higher order autonomy for a RHex robot, incorporating additional sensors for robust state estimation, visual navigation, and obstacle avoidance, as well as greater dexterity in controlling its legs to climb over and through obstacle fields. Odex 1 is a six-legged walking robot, whose weight is only 300 pounds. Its onboard computer could be operated remotely and the robot moves under its own power. It is capable of reconfiguring its shape to be tall and slender or short and squat, and it is able to walk in either configuration or anywhere between two of them. Each leg is able to lift 400 lbs and it is versatile enough to be used as manipulator as well. Odex is capable of lifting over 2,100 lbs vertically, or carrying over 900 lbs at a normal walking speed. As an example of Odex 1 agility, this robot was able to walk to a truck, get on the truck, then get off, and move the truck itself, [22]. Additional references to other prototypes of walking robots from a rich literature can be found for example in [7-8].

In this paper design issues are reported for a new six-leg walking robot named Cassino Hexapod robot. The new design has been conceived with commercial components that decrease cost and control complexity for the robot system. An articulated mechanism has been considered as driving mechanism for the leg structure with the aim of performing a suitable pitch movement with only 1 DOF. In addition, actuated wheels have been proposed at leg tips both for wheeled operation and regulating contact force with the ground. Indeed, a wheeled foot gives the possibility of elaborating a strategy for the contact control between robot foot and floor. For example, the hybrid mobile robot named "Roller-Walker" uses a similar solution of the proposed hexapod for the robot mechanism, [23]. It is a vehicle with a special foot mechanism, which changes operation between feet operation mode for the

walking and passive wheels for the wheel operation mode for fast motion. The wheeled locomotion is based on the same principle of roller-skating, [24]. Passive wheels were equipped on tips of each leg and also they installed small actuators for the ankle change.

The proposed design has been validated through dynamic simulations of basic robot operations in terms of components efficiency, motor synchronizations, and operation versatility during legged and wheeled performances under dynamic conditions. In addition, a suitable control architecture, that includes a space-state control strategy, is developed to achieve a proper hexapod gait.

2 THE DESIGN PROBLEM FOR LEG MECHANISMS

Stable, efficient and fast robots are needed to operate in uneven terrains that can be the environments in missions of demining, pipe inspection, inspection and restoration of archaeological sites, and interplanetary exploration, as indicated in [7-25]. The locomotion of hexapod living beings has been studied in order to recognize suitable walking gaits for implementing in the robot locomotion. Similar studies have been developed, for example, in [26] for comparing a bio-inspired robot operation with the cockroach performance.

Since a robot can be statically stable when three or more legs are in contact with the terrain, a hexapod robot has great stability capabilities during its motion. In fact, it can achieve statically stable walking even if one or two legs are out of order or not properly working. Frequently, hexapods are programmed for specific gaits, which allow the robot to move forward, turn, and side-step, [6]. Several hexapod gaits can be considered such as alternating tripod gait, quadruped gait, and one leg at a time. These gaits are typically stable, even in slightly rocky and uneven terrains. However, coordinating a large number of motors for even simple tasks can be very complex and expansive in resulting hexapod robots unsuitable for practical applications. Therefore, it is advisable to design hexapod robots having easy-operation low-cost features.

A low-cost hexapod robot prototype with legs and wheels has been developed at LARM in Cassino named as Cassino Hexapod, which characteristics are reported in [27-30]. A novel design has been conceived with the aim of developing a walking leg by using mainly low-cost industrial components with the following basic requirements:

- to have a robust mechanical design;
- to have a modular design that can be used for robots even with different number of legs;
- to be easily operated with an easy flexible programming;
- to have low-cost both in design and operation.

Those requirements can be achieved in a very practical way by using commercial low-cost components for a suitable design of the whole system. Since planning the movement of one leg is very important for the successful performance of the robot, suitable walking gaits must be implemented for hexapod locomotion by maintaining a static stability of the robot with at least three legs in contact with the ground [4-5]. Figure 1 shows a scheme with movements of six legs with a footfall formula representation. The legs that are in contact with the ground surface are indicated as black circles in a table in which the entries represent the possible foot contacts with the ground. In particular, Figure 1(a) shows a scheme in which the hexapod gait is given by one leg in contact with the floor and Figure 1(b) shows a scheme in which the hexapod gait is given by three legs in contact with floor. In a tripod gait, the front and rear leg of one side and the middle leg of another side perform their swing movements at the same time. Thus, the swings of right and left tripods have to be synchronised by properly setting a time delay among the leg swings. Each leg of the Cassino Hexapod has been designed as actuated by a DC motor which is activated by a controller, based on a digital logic. The strategy is generally based on actuating joints stopping as soon as it reaches its extreme position, which is detected by a limit switches, and continuing the movement in opposite sense.

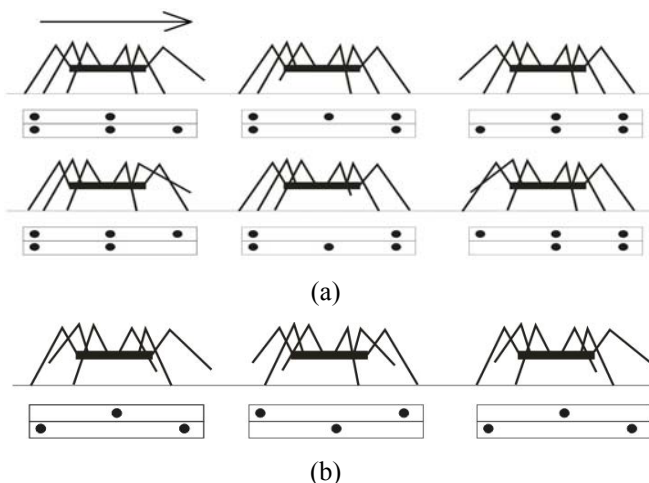


Figure 1 Footfall formulas representation of movements for six legs: (a) one-legs gait; (b) three-leg gait. (Black circles stands for the legs in contact with the ground surface; arrow indicates the moving forward direction).

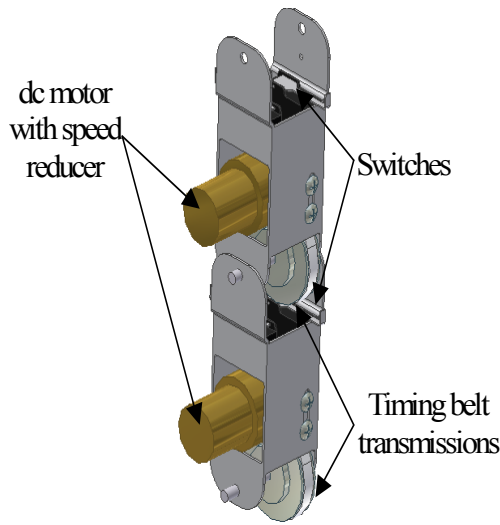
The attached problem in this paper is how to achieve a feasible movement for a hexapod gait with a mechanical structure composed of commercial components, mechanical pieces with no complex features and suitable mechanisms. In addition, a wheel has been installed in the robot foot in order to obtain higher versatility through wheeled

operations as well as including force and velocity control at the contact point with the ground.

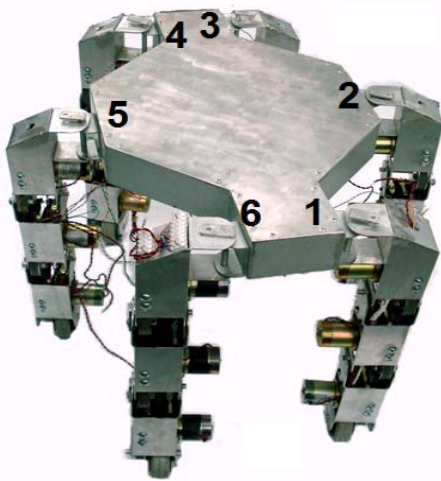
In the past, active wheels were often used for wheeled locomotion, [25]. However installation of active wheels can limit walking machine's ability, since active wheels need actuators, brake mechanisms and steering mechanisms. This equipment is heavy and bulky so that it cannot be a practical solution for a walking robot with many degrees of freedom, [23-25]. Nevertheless, the proposed Cassino Hexapod has just one DOF for performing the two-DOF movement of each leg. Therefore, an additional actuator can be conveniently installed to operate a wheel.

3 THE PROPOSED DESIGN

A modular mechanical design has been achieved by defining a single link module, which can be easily connected with other modules, with the needed actuators, transmissions and sensors inside the link body. Figure 2(a) shows the proposed design for a single link module in the first prototype, [20], and Figure 2(b) shows a built prototype of Cassino Hexapod that is based on this link module. The walking machine can fit a cuboid of 60 cm x 60 cm x 50 cm without any payload or PLC installation, its weight is of 18 kg, and with the PLC it has an overall weight of 22 kg. The operation of the Cassino Hexapod is achieved by using a PLC to control all the motors. A Siemens PLC Simatic S7-200 has been used and installed on board. The program for the hexapod operation has been written in STEP-7/Micro WIN 32 environment. The operation program can be downloaded from a PC into the flash memory of the PLC by using a RS 232/PPI cable. An external DC Power Supply is used to provide power to the hexapod but a battery can be also installed on the robot platform. A study of feasibility of using the proposed hexapod has been investigated for analysis and survey of historical architecture site in [27] by referring to the Basilica of Montecassino Abbey that was built between 1066 and 1071. Other leg design solutions are still under investigation at LARM with the aim to further reduce complexity and costs as well as to improve overall performance [28]. Proper movement of a hexapod robot is possible by properly synchronising the motion of the six legs. Therefore, a new solution for a Cassino Hexapod Robot is based on millipede anatomy and walking. When a millipede walks, each leg takes a step that consists of two stages [15-17, 20]. The first phase is when the claw is in contact with the ground and moves backward while the animal body moves forward. The second phase is the recovery stage when the leg moves forward in the air. In millipedes, the propulsive stage is longer than the recovery stage since larger is the thrust for pushing.



(a)



(b)

Figure 2 Cassino Hexapod, [18]: (a) a 3D model of a modular leg; (b) Cassino Hexapod prototype at LARM.

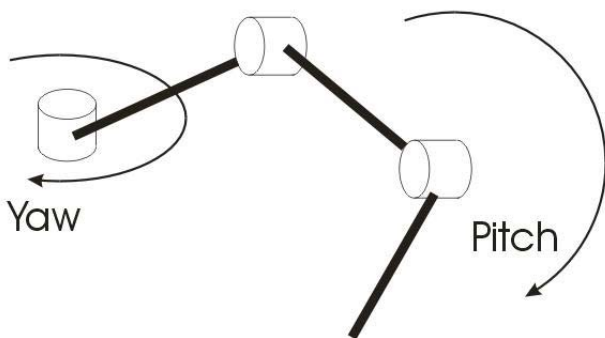


Figure 3 A kinematic scheme of operation motion for a millipede-like leg in a hexapod robot.

Based on the millipede locomotion, the proposed hexapod leg must perform mainly pitch and yaw movements for walking, as shown in the kinematic scheme of Figure 3. An articulated mechanism has been used as design solution for the leg driving mechanism. It drives the pitch leg movement through the cross-four-bar linkage mechanism of Figure 4. A first cross-four linkage mechanism is given by the links l_{11} , l_{21} ; l_{31} ; l_{41} and a second -four linkage mechanism is given by the links l_{12} , l_{22} ; l_{32} ; l_{42} . This second mechanism is actuated by the link l_{41} of the first cross-four linkage mechanism. Then, the link l_{42} operates the link that is connected to the wheel, as shown in Figure 4.

The proposed driving mechanism allows the two DOFs movement of a hexapod leg with only one actuator by reducing power consumption and structure weight. A similar driving mechanism has been used also in robotic hand design solutions at LARM [32], since the mechanism characteristics allow to perform a three DOF movement with only one actuator for anthropomorphic grasping. The mechanism of Figure 4 has been properly designed in order to obtain a feasible leg configuration so that downward and upward movements can be performed for walking. Table 1 lists values of the leg mechanism parameters that have been sized after a proper synthesis procedure for obtaining overall robot dimensions similar to the prototype of Figure 2. Note that θ_{ij} ($i = 1, 2, 3$ and $j = 1, 2$) in Table I are variable angles because they represent driven angles of the mechanism in Figure 4. The other fixed values are the sizes of mechanism links. The yaw movement is performed by actuating directly the hip joint with a commercial DC motor in a robust assembly, as shown in Figure 5. Finally, a wheel has been installed in the robot foot, as recognized in the end-effector of Figure 5, with the aim of increasing versatility and controlling contact with the ground. Figures 5 and 6 show 3D CAD models of the new design of the Cassino hexapod robot as obtained in Pro-Engineer environment.

Figure 5 shows leg structure, in which the mechanism of Figure 4 can be recognized. In the leg base-frame, a yaw joint is equipped with a DC motor in vertical position with proper ball bearings for reducing friction and achieving a compact suitable assembly.

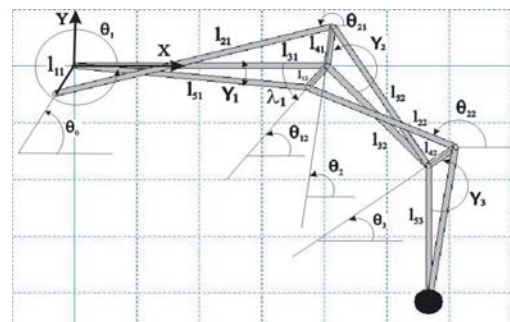


Figure 4 A kinematic model of a new leg for the Cassino Hexapod Robot with design and operation parameters.

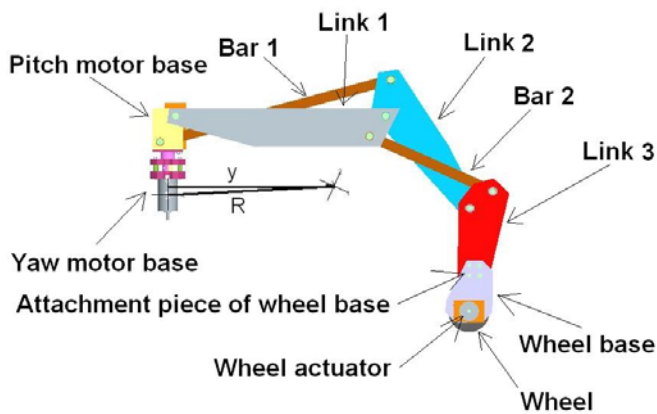


Figure 5 A 3D CAD model of the new design for Cassino Hexapod leg.

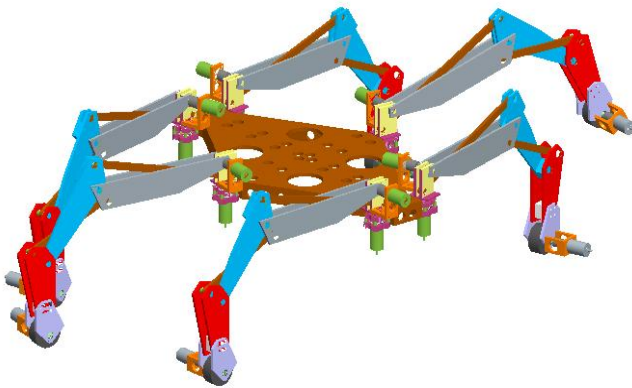


Figure 6 A 3D CAD model of the new Cassino Hexapod assembly.

Table I - Sizes for kinematic parameters of the leg mechanism in Figs. 4 and 5.

Links [mm]		Angles [deg]	
l_{11}	58.3	θ_1	Input angle
l_{51}	375.0	θ_0	59.1
l_{21}	460.0	γ_1	5.9
l_{12}	50.0	λ_1	50.2
l_{31}	405.0	θ_{21}	Variable angle
l_{41}	70.0	θ_{12}	Variable angle
l_{32}	240.0	γ_2	130.0
l_{22}	260.0	θ_2	Output angle
l_{52}	290.0	θ_{22}	Variable angle
l_{42}	55.0	θ_3	Output angle
l_{53}	198.4	γ_3	127.2

A similar DC motor assembly has been used for the foot joint, in which the actuator is directly installed on the wheel axis. Finally, Figure 6 shows an overview of the whole hexapod model. The body platform of the new design is similar to the first Cassino Hexapod prototype of Figure 2 since this hexagonal-like shape provides a leg location that keeps the operating leg close to the robot support area.

4 ADAMS MODEL FOR DYNAMIC SIMULATION

An ADAMS model of the new Cassino Hexapod has been developed in order to study task performances and operation feasibility. MSC.ADAMS® is software that permits to obtain realistic simulations of full-motion behaviour of complex mechanical systems, as outlined in [33]. Figure 7(a) shows a model of the new hexapod robot that has been implemented in ADAMS environment. A model in ADAMS environment can take into account several aspects, such as external forces, gravity, contact constraints, friction, inertia properties and reference frames whose high number, as shown in Figure 7. Those can make difficult and complex a dynamic simulation. Moreover, ADAMS creates several local coordinate frames during the modelling of parts, as shown in Figure 7. These frames are significant since the simulation rely on the location of these coordinate frames for the numerical computations.

Dynamic simulations of the new hexapod robot in ADAMS environment have been carried out in order to investigate the operation capability and more in general the feasibility of the proposed structure. The ADAMS model of Cassino Hexapod has been elaborated by introducing each component with its specific characteristics in terms of material, mass, density, shape and mechanical design. Almost all components have been considered as made of aluminum alloy and commercial components have been modelled by representing their material properties as accurate as possible, as reported in Table II. A proper dynamic walking for the robot requires setting of proper values of friction coefficients between ground and feet. Thus, static and dynamic coefficients of friction between feet and floor have been carefully selected as average friction values for a contact between rubber and concrete. In particular, friction coefficients have been chosen as equal to 0.7 for the static condition and 0.5 for the dynamic condition, in agreement with suggestions in [34]. Friction effects have been considered also for joint operation as equal to 0.5 for static coefficient and equal to 0.3 for dynamic coefficient that are default values in ADAMS environment, [33]. Differential equations of a dynamic problem can be solved over an interval of time during a simulation by using a suitable integrator algorithm. The used integrator for simulation has been Gear Stiff integrator (GSTIFF) that is the standard integrator in ADAMS, [33]. The GSTIFF integrator uses a backwards differentiation formula to integrate differential and algebraic equations.

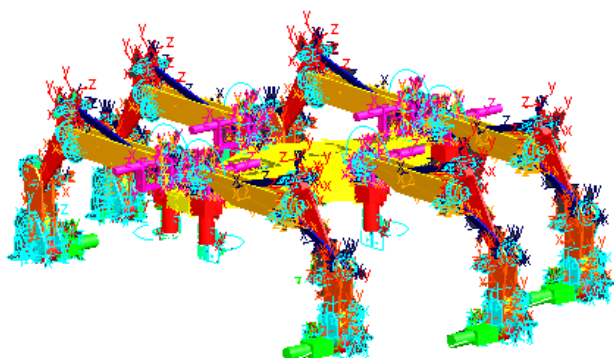


Figure 7 An ADAMS model of the New Cassino Hexapod with all structural constraints.

Table II - Main inertia data for the new hexapod leg in Figure 5.

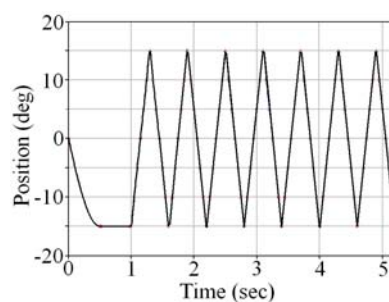
Module	Weight [N]	Ixx [kg-m ²]	Iyy [kg-m ²]	Izz [kg-m ²]
Bar 1	2.28	4.18E03	4.18E03	9.18E00
Bar 2	3.06	5.82E02	1.35E04	1.39E04
Pitch motor base	11.11	3.41E03	2.89E03	9.62E02
Wheel base	1.76	1.76E02	9.63E01	2.70E02
Yaw motor base	9.93	1.11E03	2.75E02	1.12E03
Link 1	5.91	2.52E02	7.64E03	7.89E03
Link 2	9.94	7.04E03	1.51E04	2.19E04
Link 3	3.18	1.81E02	9.90E02	1.17E03
Wheel base attachment	1.84	2.04E03	1.30E04	1.49E04
Wheel actuator	9.16	6.68E03	1.84E04	2.11E04
Wheel	2.23	1.14E02	1.82E02	1.14E02
Body	76.4	4.05E05	1.11E05	5.13E05

A time interval 0.01 (100 intervals in 1 sec) has been selected after several attempts for developing the dynamic simulation of the new Cassino Hexapod in order to obtain numerical results with reasonable computational efforts. Three modes of operation have been analyzed in ADAMS environment in order to check and characterize operation performances of the new hexapod, namely straight walking, obstacles overpassing and wheeled operation. A first simulated operation mode is related to the straight walking operation with a millipede-like motion at a velocity of 1 m/sec on a flat terrain. Figure 8 shows the motion inputs for the legs starting after 1 sec with suitable gait. The input curves for all six hexapod legs are the same of Figure 8, for

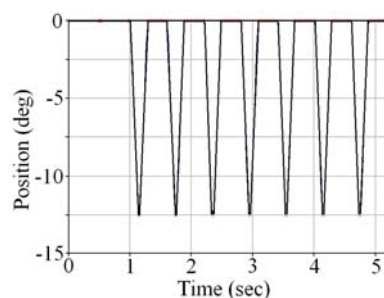
both yaw and pitch joints, but with different start time. During the simulated walking operation, the leg wheel remains blocked but it can be actuated in any instant in order to combine walking and wheeled operation. The total simulation time for walking operation has been 5 sec.

A second dynamic simulation is related to obstacle overpassing. This operation consists in the hexapod capability of avoiding obstacles by moving the platform body vertically. For this task all legs perform the same pitch movement in upward and downward directions while yaw joints are not actuated. Figure 9 shows the input for the pitch joints of the new hexapod legs that with 15 deg of peak amplitude and a frequency of 0.25 Hz. For a practical application of obstacle overpassing, the wheel shaft can be actuated together with the leg pitch movement or it can be left free to move by a clutch mechanism. In the reported simulation, the wheel has been considered free to move, since this case reduces power consumption. The simulation for the obstacle overpassing has been computed an operation of 4 sec.

A third dynamic simulation for the new hexapod has considered as operation of the leg wheels only. Figure 10 shows the input for the wheel actuator on each leg. The wheeled simulations have consisted in a combined lateral and forward robot displacement. The lateral movement can be recognized in Figure 10 from 1 to 5 sec when the angular velocity has been increasing from 0 to 2000 deg/sec. Then, after 3 sec (from 5 to 8 sec), the robot stays in a fixed position changing the leg configuration. Then, from 8 to 12 sec the robot moves each wheel forward at 2000 deg/sec. The total simulation time for wheeled operation has been 12 sec.



(a)



(b)

Figure 8 Motion inputs for a walking simulation: (a) leg yaw input, (b) leg pitch input.

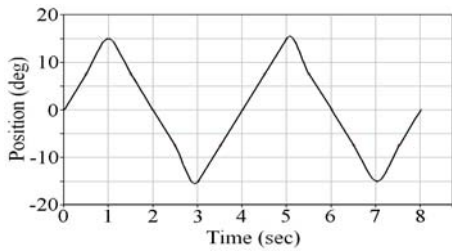


Figure 9 Input of the leg pitch for obstacle overpassing.

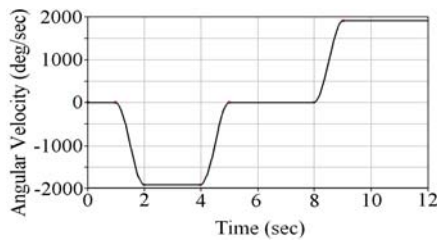


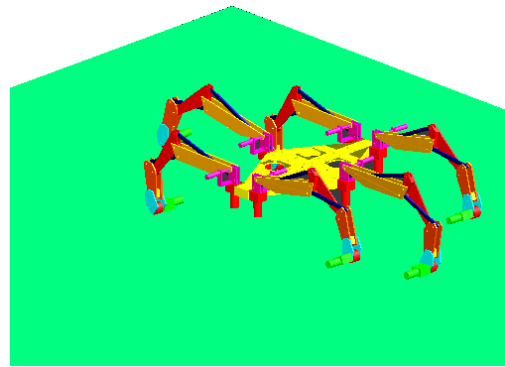
Figure 10 Wheel motor inputs for wheeled operation simulation.

5 SIMULATION RESULTS

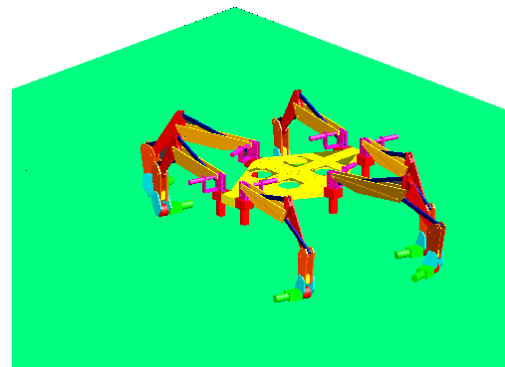
5.1 STRAIGHT WALKING

Figure 11 shows a sequence of the simulated straight on walking of the new Cassino Hexapod. Figure 12 shows the computed angular velocities and actuating torques for all pitch and yaw actuators. In particular, in Figure 12(a) the yaw torque shows an average value of about 50 Nm and a maximum value of about 100 Nm. Peaks of actuating torque with values larger than 100 Nm have not been considered in the design process, since they have been considered as errors of the numerical solutions of differential equations within ADAMS.

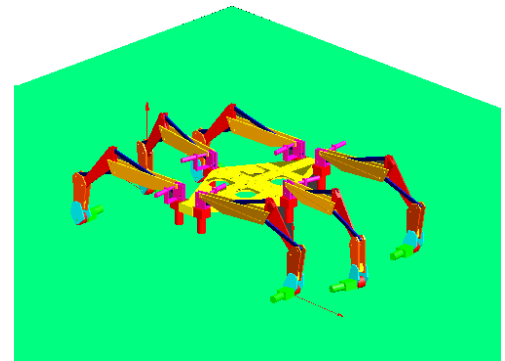
The average value of angular velocity has been computed as about 100 deg/sec and the maximum value has been about 130 deg/sec. Figure 12(b) shows results of actuating torque and angular velocity for leg pitch. The maximum values of pitch torque of about 25 Nm, which is notable lower than the yaw torque because the pitch function during walking is aimed to just lifting and releasing robot leg. The maximum value of angular velocity has been as about 125 deg/sec with 3.33 Hz of frequency. Figure 13 shows results of contact force between hexapod feet and floor. The maximum force value of about 950 N has been computed at about 3 sec during the contact of front left leg and floor. The maximum body platform velocity has been defined as equal to 1 m/s². This velocity can be considered a quite high dynamic behavior. For example, the well known Bigdog robot has set the world land speed record for legged robots as 6 m/sec, [9]. Then, the maximum leg acceleration for achieving the above-mentioned desired body platform velocity has been computed as equal to about 13.7 m/sec².



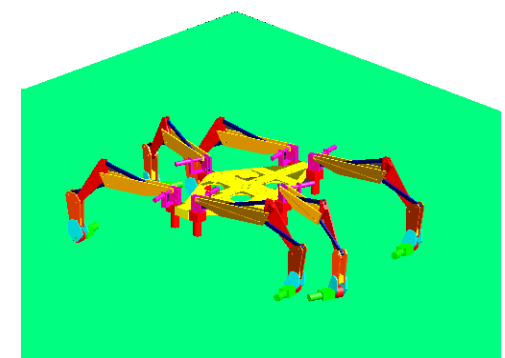
(a)



(b)



(c)



(d)

Figure 11 Sequence of the simulated straight walking of the new hexapod with 1m/s: (a) initial position; (b) after 1 sec; (c) after 3 sec; (d) final position.

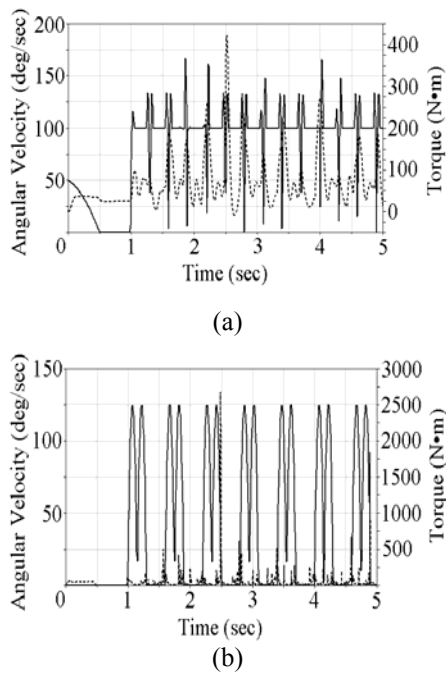


Figure 12 Computed results of angular velocity and torque at actuating joints of the robot leg during the simulated straight walking operation in Figure 11: (a) yaw; (b) pitch. (Torque is in dashed line and angular velocity is in solid line).

Figure 14 shows plots of position, velocity and acceleration of the body platform. In particular, Figure 14(a) shows the body platform position and Figure 14(b) shows the body platform velocity in solid line and acceleration in dashed line. Zero values from 0 to 1 sec are related to a steady state of the hexapod before motion starts.

5.2 OBSTACLE OVERPASSING

Figure 15 shows a sequence of the dynamic simulation of obstacle overpassing by moving the robot body platform vertically. Figure 16 shows computed results for angular velocity and actuating torque of pitch joints in the hexapod legs. Note that pitch joint is operated in the same way for all legs during vertical movement. Thus, Figure 16 represents the results for all hexapod legs. The maximum peaks of torque in Figure 16 can be recognized at 1 and 3 sec when the hexapod body platform reaches the highest and lowest positions, respectively. The maximum of actuating torque has been computed as about 9 Nm. The maximum of angular velocity has been obtained as 23 deg/sec. Figure 17 shows the contact force between robot feet and floor for all six legs. The maximum value of contact force has been computed as about 140 N just after hexapod body platform reaches the highest position at 1.3 sec. Finally, Figure 18 shows plots of position, velocity and acceleration of the centre of mass of the hexapod body platform during the vertical movement.

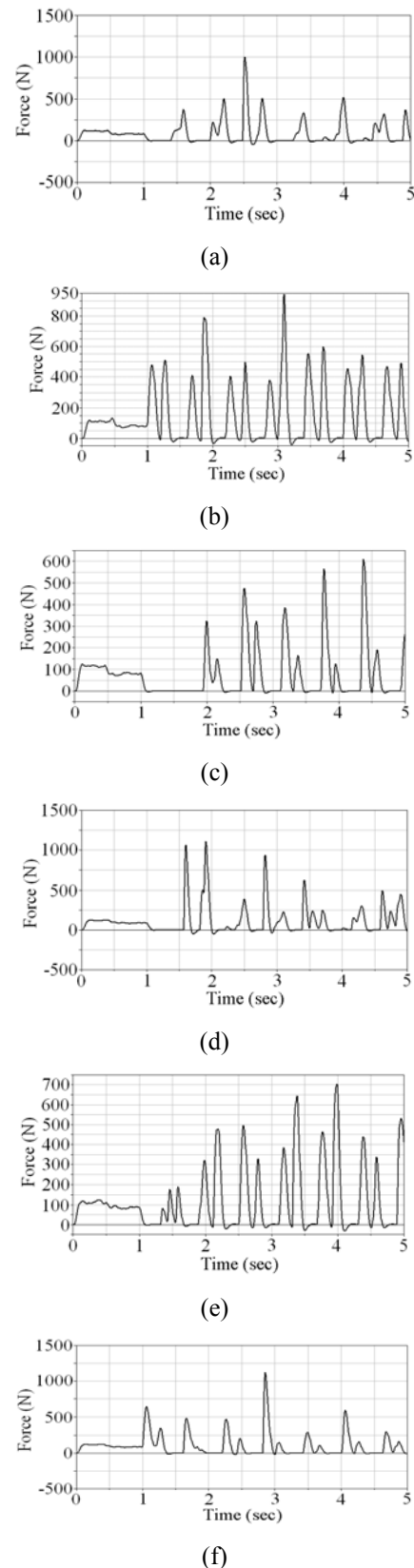


Figure 13 Contact force between feet and floor during straight walking simulation: (a) front right leg; (b) front left leg; (c) middle right leg; (d) middle left leg; (e) back right leg; (f) back left leg.

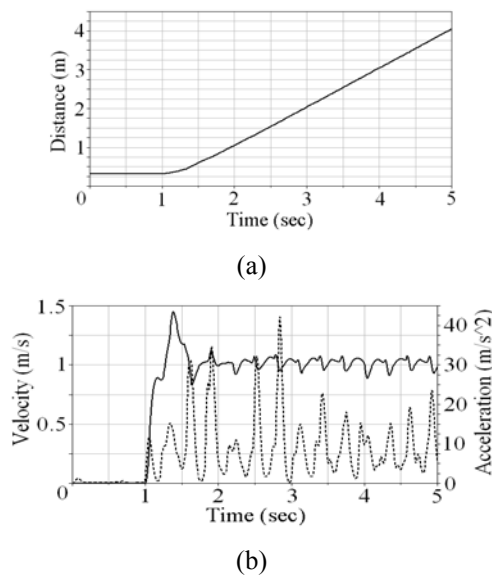


Figure 14 Computed results for the motion of the hexapod body platform during straight walking operation: (a) position; (b) velocity and acceleration (velocity in solid line and acceleration in dashed line).

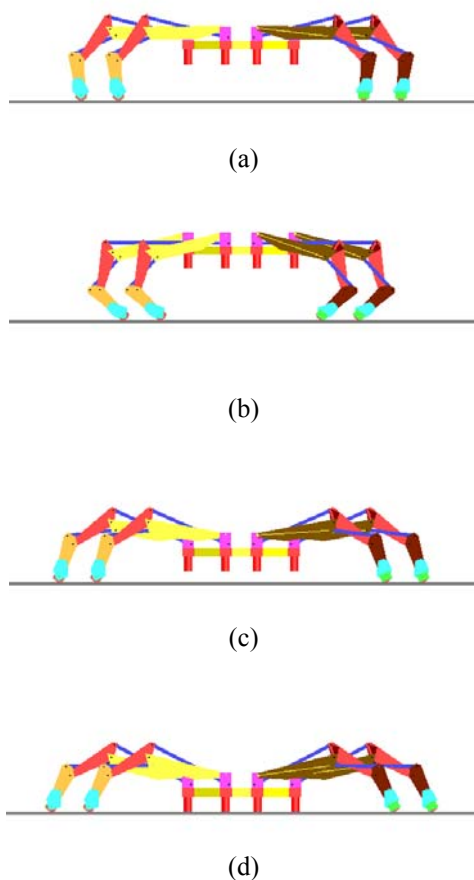


Figure 15 Sequence of obstacle overpassing of the Cassino Hexapod: (a) initial position (c) highest position reached; (d) downward movement; (e) lowest position reached.

In particular, Figure 18(a) shows the time evolution of body platform position in which the initial position can be recognized as about 0.33 m above floor, highest position as about 0.44 m and lower position as about 0.12 m. Figure 18(b) shows plots of velocity in solid line and acceleration in dashed line. The maximum acceleration magnitude has been about 13 m/sec² and the maximum velocity value has been about 0.25 m/sec.

5.3 WHEELED OPERATION

Figure 19 shows a dynamic simulation of a hexapod operation using just the wheel actuators. Figure 20 reports results of angular velocity, in solid line, and actuating torque, in dashed line, of wheel motors of all six hexapod legs. The robot performs combined lateral and forward movements that can be clearly recognized in the angular velocity curve of Figure 20. The wheel velocity increases initially from 0 to about 1900 deg/sec that is related with the lateral movement. Then, the velocity value goes to 0 deg/sec, from about 5 sec to about 8 sec, that represents a stationary position during the legs are undergoing reconfiguration. Finally, after about 8 sec the velocity is again increased until about 1900 deg/sec that represents the forward movement. The maximum actuating torque has been about 5 Nm with an average of about 2.3 Nm.

Figure 21 shows the plot of contact force between robot feet and floor for all six legs. The maximum contact force between wheels and floor has been computed as about 150 N with an average value of about 50 N during whole simulation time.

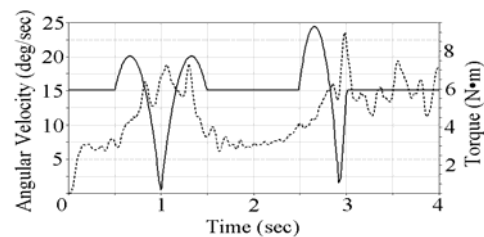


Figure 16 Computed results of angular velocity and torque at pitch joint of robot leg during the obstacle avoiding movement in Fig.15. (Torque in dashed line and angular velocity in solid line)

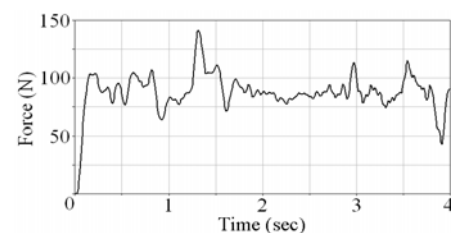
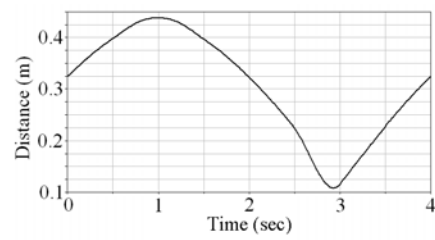
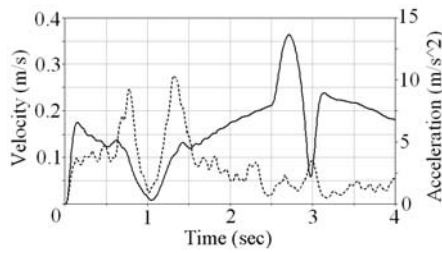


Figure 17 Computed contact force between feet and floor during the obstacle avoiding movement.

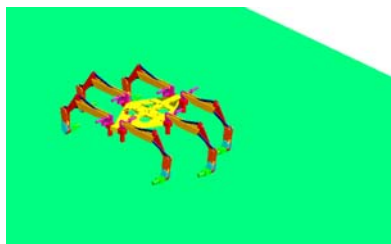


(a)

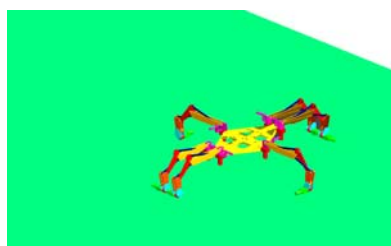


(b)

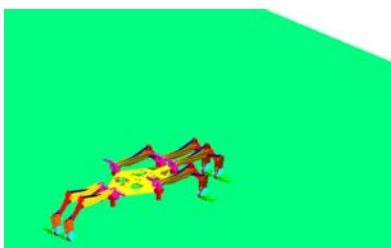
Figure 18 Computed results for the motion of the platform body during the obstacle avoiding movement: (a) position; (b) velocity and acceleration (velocity in solid line and acceleration in dashed line).



(a)



(b)



(c)

Figure 19 A sequence of wheeled operation of the proposed new hexapod: (a) lateral movement; (b) changing leg configuration; (c) straight wheeled movement.

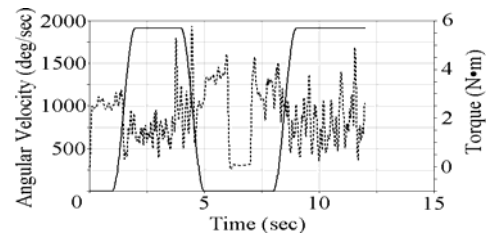


Figure 20 Computed results of angular velocity and torque at wheel joint during the wheeled operation in Figure 19. (Torque in dashed line and angular velocity in solid line)

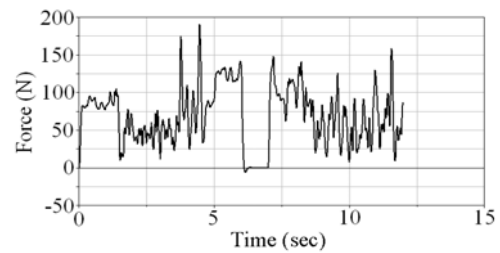
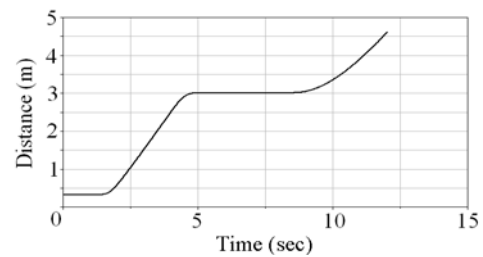
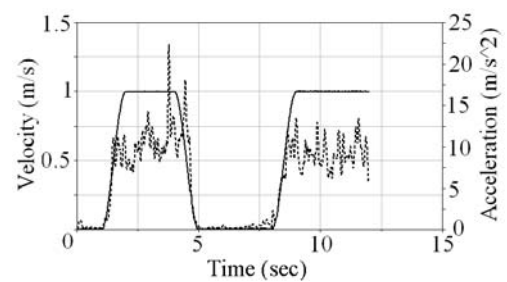


Figure 21 Computed contact force between feet and floor during the wheeled operation in Figure 19.



(a)



(b)

Figure 22 Computed results for the motion of the hexapod body platform during wheeled operation: (a) position; (b) velocity and acceleration (velocity in solid line and acceleration in dashed line).

Note similar time evolutions for actuating torque curve of Figure 20 and contact force curve of Figure 21 since the leg wheel are actuated by a DC motor directly installed at the wheel joint. Therefore, the actuation requirements for the wheel motor are basically based on overcoming the friction at floor contact. Finally, Figure 22 shows plots of position,

velocity and acceleration of body platform during the wheeled simulation. In particular, Figure 22(a) shows the curve of body platform position in which the two ramps represent lateral and forward displacements and the horizontal curve represents the stationary position. Figure 22(b) shows plots of velocity in solid line and acceleration in dashed line.

6 A DESIGN FOR A CONTROL ALGORITHM

Suitable control architecture has been designed by considering the results of operation simulations of the Cassino Hexapod robot. Dynamic analyses have been carried out for the operation of pitch and yaw leg motors. Leg motors move the whole leg structure that can be considered as a mass concentrated in the centre of mass of leg. Figure 23 shows a block diagram of a feed-back control strategy in the space state [35] for an accurate leg movement according to the simulation results. From Figure 23 and using the dynamics of leg mechanism, the differential equations for the motor circuits and torques can be expressed as

$$\begin{aligned} P \sin(\theta_p)R + J \frac{\partial \theta_1}{\partial t} &= K_{21}i_{a1} \\ L_{a1} \frac{\partial i_{a1}}{\partial t} + R_{a1}i_{a1} + K_{31} \frac{\partial \theta_1}{\partial t} &= K_{11}e_{v1} \\ P y + J \frac{\partial \theta_2}{\partial t} &= K_{22}i_{a2} \\ L_{a2} \frac{\partial i_{a2}}{\partial t} + R_{a2}i_{a2} + K_{32} \frac{\partial \theta_2}{\partial t} &= K_{12}e_{v2} \end{aligned} \quad (1)$$

where P is the leg weight, J is the leg moment of inertia, R is the distance from frame to leg centre of mass; K_{21} and K_{22} are the torque constants of pitch and yaw motors, respectively; i_{a1} and i_{a2} are the currents of pitch and yaw motors, respectively, L_{a1} and L_{a2} are the inductances of pitch and yaw motors, respectively, R_{a1} and R_{a2} are the resistances of pitch and yaw motors, respectively, K_{31} and K_{32} are the constants of the electromotive force of pitch and yaw motors, respectively, K_{11} and K_{12} are gains of pitch and yaw motors, respectively, and e_{v1} and e_{v2} are the input voltages of pitch and yaw motors, respectively. θ_p and θ_y represent the system outputs and e_{v1} and e_{v2} represent the system inputs. The constants K_{31} and K_{32} of motor electromotive force have been computed as a ratio between the angular velocities ω_p and ω_y and input voltage e_{v1} and e_{v2} of pitch and yaw motors, respectively. The new hexapod design has been conceived by assuming both pitch and yaw motors as DC motors RS 235-7780 [36], whose parameters are listed in Table III.

A linearization of Equation (1) is necessary for the proposed analysis in order to implement the control strategy of Figure 23. For this aim a state-space feedback linearization [35] can be computed as

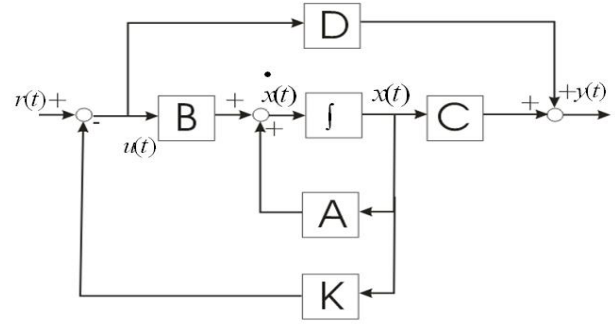


Figure 23 A proposed control scheme for the New Cassino Hexapod [25].

Table III - Parameter values of DC motors RS 235-7780 for leg design.

Parameter	Value
P	69.3 N
R	0.32 m
J	2.79e-2 kg*m ²
K_{21} ; K_{22}	31.10e-3 N*m/A
i_{a1} ; i_{a2}	64.31 A
L_{a1} ; L_{a2}	0.95e-3 H
R_{a1} ; R_{a2}	7.40 Ω

$$\begin{aligned} \dot{X}_1 &= X_2 \\ \dot{X}_2 &= \frac{K_{21}}{J} X_3 - \frac{P_T R}{J} \sin X_1 \\ \dot{X}_3 &= \frac{K_{11}}{L_{a1}} u_1 - \frac{R_{a1}}{L_{a1}} X_3 - \frac{K_{31}}{L_{a1}} X_2 \\ \dot{X}_4 &= X_5 \\ \dot{X}_5 &= \frac{K_{22}}{J} X_6 \\ \dot{X}_6 &= \frac{K_{12}}{L_{a2}} u_2 - \frac{R_{a2}}{L_{a2}} X_6 - \frac{K_{32}}{L_{a2}} X_5 \end{aligned} \quad (2)$$

where X_1 is the pitch angular displacement θ_p , X_2 is the pitch angular velocity ω_p , X_3 is the pitch motor current i_{a1} , u_1 is the pitch motor input e_{v1} , X_4 is the yaw angular displacement θ_y , X_5 is the yaw angular velocity ω_y , X_6 is the yaw motor current i_{a2} and u_2 is the yaw motor input e_{v2} . Making a variable change of X_1 to Z_1 yields to the expressions of the state-space representation in the form

$$\begin{bmatrix} \dot{Z}_1 \\ \dot{Z}_2 \\ \dot{Z}_3 \\ \dot{Z}_4 \\ \dot{Z}_5 \\ \dot{Z}_6 \end{bmatrix} = \begin{bmatrix} 0 & 1 & 0 & 0 & 0 & 0 \\ 0 & 0 & 1 & 0 & 0 & 0 \\ 0 & -\frac{K_{31}K_{21}}{JL_{a1}} & -\frac{R_{a1}}{L_{a1}} & 0 & 0 & 0 \\ 0 & 0 & 0 & 0 & 1 & 0 \\ 0 & 0 & 0 & 0 & 0 & 1 \\ 0 & 0 & 0 & 0 & -\frac{K_{32}K_{22}}{JL_{a2}} & -\frac{R_{a2}}{L_{a2}} \end{bmatrix} \begin{bmatrix} Z_1 \\ Z_2 \\ Z_3 \\ Z_4 \\ Z_5 \\ Z_6 \end{bmatrix} + \begin{bmatrix} 0 & 0 \\ 0 & 0 \\ 1 & 0 \\ 0 & 0 \\ 0 & 0 \\ 0 & 1 \end{bmatrix} \begin{bmatrix} v_1 \\ v_2 \end{bmatrix} \quad (3)$$

$$\begin{bmatrix} \theta_1 \\ \theta_2 \end{bmatrix} = \begin{bmatrix} 1 & 0 & 0 & 0 & 0 & 0 \\ 0 & 0 & 0 & 1 & 0 & 0 \end{bmatrix} [Z_1 \ Z_2 \ Z_3 \ Z_4 \ Z_5 \ Z_6]^T \quad (4)$$

where the new system inputs v_1 and v_2 has the form

$$\begin{aligned} v_1 &= \frac{K_{21}K_{11}}{JL_{a1}}u_1 - \frac{P_T R R_{a1}}{JL_{a1}} \sin Z_1 - \frac{P_T R}{J} \cos Z_1 Z_2 \\ v_2 &= \frac{K_{22}K_{12}}{JL_{a2}}u_2 - \frac{P_T Y R_{a2}}{JL_{a2}} \end{aligned} \quad (5)$$

The control scheme of Figure 23 has been tested in Simulink environment [37], by using the formulation (3) to (5), to validate the effectiveness of proposed control strategy. Figure 24 shows the simulated results of responses θ_p and θ_y of pitch and yaw motors for unit-step signal of ev_1 and ev_2 inputs, respectively. In particular, Figure 24(a) shows the plot of pitch motor output and Figure 24(b) shows the output plot of yaw motor. The feasibility of the proposed control strategy has been tested by means of numerical simulations. Results have shown efficiency in the system operation in term of response velocity, low-value maximum error in transition-state and low steady-state error.

7 DESIGN CONSIDERATIONS

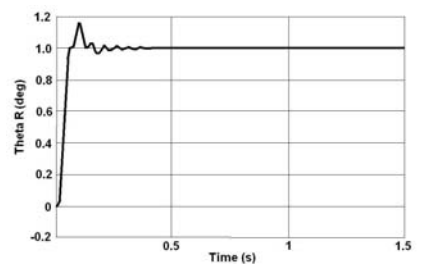
In the operation of the new hexapod, leg mechanisms play an important role. The proposed solution for leg structure increases the robustness of the original design and reduces the robot weight since its operation requires only one actuator per leg. During the motion for the three analyzed operation modes, a leg pitch movement of two DOFs has been obtained by using only one motor. The leg pitch allows operation modes like obstacle overpassing at different vertical position, as shown in Figure 15. Similarly, yaw joint generates a rotation movement of the whole leg structure that provides enough versatility for various operations. During walking simulation in Figure 11, leg yaw is synchronized with pitch to achieve a successful walking. Specifically, in the walking simulation, when the yaw motor rotates the whole leg structure pitch motor lift the leg for obtaining a millipede-like motion.

Moreover, during wheeled operation simulation of Fig. 19, yaw movement locates the leg in specific positions for straight, lateral or diagonal movements. The maximum required torque for leg actuation, of about 100 Nm, can be achieved by a commercial DC motor and a gearbox with a proper reduction ratio. For example, a Kollmorgen 01212 DC motor, [38], with a maximum output torque of 1.18 Nm can be used for the actuation of the robot yaw joints that, in an assembly with a Harmonic Drive CSD-20-160-2A-GR [39] with 160 of reduction ratio and 75 % of efficiency, yields an output torque of 141.6 Nm. The weight of the frameless version of the 01212 DC motor is 0.274 kg and

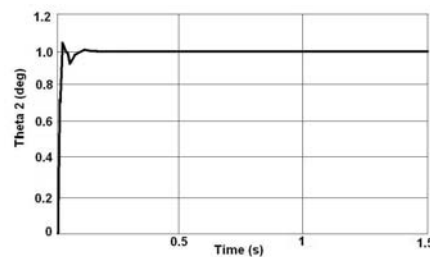
the Harmonic Drive CSD-20-160-2A-GR weight is 0.13 kg. Therefore, the weight of the actuation assembly for the proposed practical application is 0.404 kg that represents a feasible value for the proposed design. The required torque for pitch is notable smaller than that for yaw actuation. Thus, lighter motor and gearbox can be used as solution for pitch actuation in order to reduce weight for robot structure. Including a wheel at foot is an important feature of the new hexapod leg design. The wheel operation increases the versatility of robot that can move in flat terrain in a wheeled mode faster than walking mode. Moreover, the contact between robot feet and floor can be controlled in term of force and friction by using wheel actuator. In fact, peaks of Fig. 13 can be limited by implementing a suitable feed-back control architecture that manages contact force.

Body platform plays an important role in the robot stability. Rectangular shape is the most common shape that is used for legged mobile robots. Nevertheless, the proposed specific shape of robot body platform ensures that the centre of mass of the whole hexapod will be always inside the supporting area. Moreover, holes on body platform surface in Fig. 6 can reduce robot weight with no complex features for manufacturing.

Space-state architecture allows controlling several outputs of a system from several inputs by using a single transference function [34]. Linearization by space-state feedback is a method that can compute no linear expressions with not high computational efforts. The equations of new hexapod legs and motors present no linear expressions with two inputs (motor voltages) and two outputs (pitch and yaw angular positions).



(a)



(b)

Figure 24 Output plots of actuating joints response for a one-unit stimulus: (a) yaw joint; (b) pitch joint.

The proposed space-state algorithm represents a suitable solution for a user-oriented position control. The main goal of the proposed control is to generate accurate movements of robot legs, for all the simulated modes of robot operation, by controlling the voltage supplied to motors. Moreover, the control scheme of Figure 23 can be implemented in practical applications through a commercial controller.

CONCLUSIONS

A new design for leg structure in a hexapod robot is presented as based on previous experiences and prototypes of the existing Cassino Hexapod. The leg mechanism has been designed with a linkage chain that permits a 2-DOFs motion with only one actuator. The feasibility of the proposed design and its operation have been tested through suitable simulation modes of robot operation, which have been used and implemented also by defining a control architecture and the related control algorithms. Results of numerical simulations have proved the feasibility of the proposed design solution that reports enhanced performance also in terms of low-cost easy-operation features.

REFERENCE

- [1] Rosheim M. E., *Robot evolution, the development of anthropotics*. A Wiley-Interscience Publication, 1994.
- [2] Morecki A. and Waldron K.J., *Human and machine locomotion*. Springer Verlag, 1997.
- [3] Carbone G. and Ceccarelli M., *Legged robotic systems*. Cutting Edge Robotics ARS Scientific Book, 2005.
- [4] Zielinska T. and Heng J., Development of a walking machine: mechanical design and control problems. *Mechatronics*, Vol. 12, No. 5, pp. 737 – 754, 2002.
- [5] Zhao S.Y., Lu L., Zhao T.S., Du Y.H. and Huang Z., Dynamic performance analysis of six-legged walking machines. *Mechanism and Machine Theory*, Vol. 35, No. 1, pp. 155 – 163, 2000.
- [6] Reumoat P., Alezandre P. and Ghuya D., Gait analysis and implementation of a six leg walking machine. *Proc. of International Conference Robots in Unstructured Environments*, Pisa, Vol. 2, pp. 941-945, 1991.
- [7] Berns K., *Catalogue of walking machine*. Available on-line at <http://www.walking-machines.org/>, 2010.
- [8] *The old robot web side*. Available online at <http://www.theoldrobots.com/odex.html>, 2011.
- [9] Raibert M., Blankerpoor K., Nelson G., Playter R. and BigDog Team, BigDog, the rough-terrain quadruped robot. *Proc. of 17th World Congress the International Federation of Automatic Control IFAC*, Seoul, pp. 10822-18025, 2008.
- [10] Nonami K. And Huang Q.J., Humanitarian mine detection six-legged walking robot. *Proc. of International Conference on Climbing and Walking Robots*, Madrid, pp. 861-868, 2000.
- [11] Rachkov M., Marques L. and Almeida A., Multisensor demining robot. *Autonomous Robots*, Vol. 18, No. 3, pp. 275-291, 2005.
- [12] Kawaguchi Y., Yoshida I., Iwao K. and Kikuta T., Development of internal gas pipe inspection robot. *Journal of Robotics and Mechatronics*, Vol. 7, No. 5, pp. 371-376, 1995.
- [13] Horodincea M., Doroftei I., Mignon E. and Preumont A., A simple architecture for in-pipe inspection robots. *Proc. of International Colloquium on Mobile and Autonomous Systems*, Magdeburd, pp. 61–64, 2002.
- [14] Wilcox B., Matthies L. and Genery D., Robotic vehicles for planetary exploration. *Journal of Applied Intelligence*, Vol. 2, No. 2, pp.181-193, 1992.
- [15] Holmes P., Full R.J., Koditschek D. and Guckenheimer J., The dynamics of legged locomotion: models, analyses, and challenges. *SIAM Review*, Vol. 48, No. 2, pp. 207-304, 2006.
- [16] Full R.J., Invertebrate locomotor systems. *Comprehensive Physiology*, pp. 853–930, 2011.
- [17] Pfeifer R., Lungarella M. and Iida F., Self-organization, embodiment, and biologically inspired robotics. *Science*, Vol. 318, pp. 1088-1093, 2007.
- [18] Chakraborty N. And Ghosal A., Kinematics of wheeled mobile robots on uneven terrain. *Mechanism and Machine Theory*, Vol. 39, pp. 1273 – 1287, 2004.
- [19] Fraunhofer Institute for Factory Operation and Automation IFF, *SLAIR2 - six legged autonomous intelligent robot 2*. Available online at <http://www.ovgu.de/ieat/robotslab/slair2.php>, 2010.
- [20] Lewinger W.A., Branicky M.S. and Quinn R.D., Insect-inspired, actively compliant hexapod capable of object manipulation. *Proc. of 8th International Conference on Climbing and Walking Robots CLAWAR*, London, 65–72, 2005.
- [21] Altendorfer R., Moore N., Komsuoglu H., Buehler M., Brown Jr. H.B., McMordie D., Saranlı U., Full R. and Koditschek D.E., RHex: a biologically inspired hexapod runner. *Autonomous Robots*, Vol. 11, pp. 207–213, 2001.
- [22] Russell Jr. M., ODEX I: the first functionoid. *Robotics Age Magazine*, pp. 12-18, 1983.
- [23] Gonzalez de Santos P., Jimenez M.A. and Armada M.A., Dynamic effects in statically stable walking machines. *Intelligent and Robotic Systems*, Vol. 23, No. 1, pp. 71-85, 1998.
- [24] Hirose S. and Takeuchi H., Roller-walker: a proposal of new leg-wheel hybrid mobile robot. *Proc. of International Conference on Advanced Robotics*, pp. 917-922, 1995.

- [25] Hirose S. and Takeuchi H., Study on roller-walk (Basic Characteristics and its Control). *Proc. of International Conference on Robotics and Automation*, pp. 3265-3270, 1996.
- [26] Bailey S.A, Cham J.G., Cutkosky M.R. and Full R., Comparing the locomotion dynamics of the cockroach and a shape deposition manufactured biomimetic hexapod. In Rus D. and Singh S. (Eds), *Experimental robotics VII. Lecture notes in control and information sciences*. Springer, Vol. 271/2001, pp. 239-248, 2001.
- [27] Cigola M., Pelliccio A., Salotto O., Carbone G., Ottaviano E. and Ceccarelli M., Application of robots for inspection and restoration of historical sites. *Proc. of International Symposium on Automation and Robotics in Construction*, Ferrara, paper 37, 2005.
- [28] Ceccarelli M., Carbone G., Ottaviano E. and Lanni C., Leg designs for walking machines at LARM in Cassino. *Proc. of Workshop on 'Robotica per esplorazione lunare unmanned'*, Roma, CD Proceedings, 2009.
- [29] Carbone G. and Ceccarelli M., A low-cost easy-operation hexapod walking machine. *Advanced Robotic Systems*, Vol. 5, No. 2, pp. 161-166, 2008.
- [30] Carbone G., Jatsun A., Ceccarelli M. And Jatsun S., Design and simulation of cassino hexapod robot. *Proc. of International Conference on Computers, Rhodos*, pp. 301-314, 2009.
- [31] *LARM webpage*. Available online at <http://webuser.unicas.it/weblarm/larminindex.htm>, 2011.
- [32] MSC.ADAMS, *Documentation and Help*. User CD-ROM, 2005.
- [33] Poli R.C. and Boothroyd G., *Applied engineering mechanics*. Marcel Dekker Inc., pp. 60, 1980.
- [34] Ogata K., *Modern control engineering*. Third Edition, Prentice Hall, pp. 998, 1998.
- [35] RS webpage, *DC Geared Motors*. Available at www.rs-components.com, 2011.
- [36] Karris S.T., *Introduction to simulink with engineering applications*. Second Edition, Orchard Publications, pp. 584, 2008.
- [37] *Kollmorgen RBE (H) series motor catalog*. Available at www.DanaherMotion.com, 2010.
- [38] *Harmonic drive CSD-SHD catalog*. Available online at www.harmonicdrive.com, 2011.

PARAMETRIC RESONANCE IN CANTILEVER BEAM AND ENERGY HARVESTING OUTLOOKS

Elvio Bonisoli* Matteo Scapolan* Maryam Ghandchi Tehrani**

* Politecnico di Torino, Dept. of Management and Production Engineering, Torino, Italy

** Institute of Sound and Vibration Research, University of Southampton, Southampton, U.K.

ABSTRACT

Parametric resonances can occur in internally stressed systems due to the periodic variation of the stiffness in time. Parametric resonance can lead to unstable dynamic behaviour; however, their response is limited by existing nonlinearities in the system, thus resulting in limit cycle oscillations (LCOs). This phenomenon can be exploited in the design of energy harvesters. The amplitude and frequency of the parametric excitation can be adjusted so that the vibration response of internally stressed systems is close to instability. In this paper, a cantilever beam is considered in vertical position and an axial excitation is applied to the base of the beam. The imposed kinematics of the base leads to internal stress along the beam, which produces a variation of the bending stiffness. If the frequency of the base excitation is twice the first natural frequency of the beam, the principal parametric resonances can occur. A quasi-linear FEM approach is adopted, together with a simplified single-degree-of-freedom model of the beam, in order to numerically simulate its dynamic behaviour, to identify unstable conditions and to obtain the Floquet diagram. An analytical approach is developed as well, using a multi-degree-of-freedom model of the beam, considering the system as autoparametric. Harmonic balance method is used to determine the Floquet diagram and to validate the numerical model. Principal parametric resonance is observed experimentally. Harvesting energy from parametric resonance is therefore potentially very efficient, especially if the external source is not directly exploitable. Parametric resonance in this case acts as a power amplification.

Keywords: parametric resonance, Floquet diagram, energy harvester

1 INTRODUCTION

Faraday [1] first observed parametric resonance phenomena in a vertically oscillating fluid container, developing horizontal surface waves. The first model that described this behaviour was presented by Mathieu [2].

Parametric resonance can occur in systems with periodic-time-varying parameter(s) in the classic 2nd order differential equation, with varying mass, damping and stiffness coefficients and external forces acting on the system:

$$m(t) \ddot{x}(t) + c(t) \dot{x}(t) + k(t) x(t) = f(t) \quad (1)$$

The excitation can be externally provided by a forcing function (*external excitation*) or can arise internally from the time variation of the parameters (*self-excitation*).

In contrast to externally excited systems, self-excitation is linked with the homogeneous equation of motion ($f(t) = 0$). Thus, the presence of a periodic time varying parameter in the homogenous equation can act as an excitation, commonly referred to as *parametric excitation*.

Floquet theory is used to solve the homogeneous equation of this kind. For undamped systems, equation (1) is simplified to well-known Mathieu equation,

$$\ddot{x}(t) + (\delta + \varepsilon \cos(\Omega t)) x(t) = 0 \quad (2)$$

Contact author: Elvio Bonisoli, Matteo Scapolan,
 Maryam Ghandchi Tehrani

E-mail: elvio.bonisoli@polito.it
 matteo.scapolan@polito.it
 M.Ghandchi-Tehrani@soton.ac.uk

where the variable stiffness, consists of a constant part δ , which relates to the natural frequency of the system, and a variable part, $\varepsilon \cos(\Omega t)$, which is due to the parametric excitation. The variation of the stiffness leads to an increase or decrease of the elastic potential energy.

Under certain conditions, the energy in the system can grow exponentially in each cycle, leading to unstable behaviour. For undamped systems, when the excitation frequency is about twice the first natural frequency, a small parametric amplitude can result in primary parametric resonance. The damping in the system may not be sufficient to stabilise the unstable system and it may only delay the onset of instability [3].

Nonlinear structural vibrations can however limit the growth of the response, [4], as demonstrated by a model including quadratic and cubic geometric nonlinearities.

Oueini and Nayfeh [5] used this concept to suppress structure vibrations, by using nonlinear velocity feedback control, on a cantilever beam subjected to primary parametric resonance. Linear velocity and position feedbacks are also implemented experimentally, by Ghandchi Tehrani *et al.* [6], to avoid unstable behaviour.

The aim of this paper is to take advantage of parametric instability rather than to avoid it by providing parametric resonance conditions for energy harvesting. [7] and [8] also demonstrates that ten times more power can be harvested from parametric resonance, compared to direct resonance.

Numerical approach using quasi-linear FEM is developed using Lupos, which is an open source FEM software. Harmonic balance method is used to obtain the Floquet diagram and to validate the numerical results. Experiments are carried out to demonstrate instability due to parametric resonance. Geometric nonlinearities are observed in the response of the beam and their effects are investigated on the stability curves. An analysis based on the energy flow is carried out to explain how the potential energy varies when the parametric resonance occurs.

2 PARAMETRICALLY EXCITED BEAM

A beam in vertical position subject to an imposed kinematics of the base is considered as shown in Figure 1. The imposed kinematics is the axial displacement is along the z -axis. The axial acceleration leads to inertial effects, so that an axial load distributes along the beam as shown in Figure 1.

This normal force leads to a variation of the bending stiffness of the beam, which is periodic with the same frequency as the base acceleration (Ω), representing a parametrically excited system.

The characteristics of the beam are hereafter reported:

- length $l = 400$ mm , along z ;
- width $b = 1$ mm , along x ;
- height $h = 10$ mm , along y ;
- density $\rho = 7800$ kg/m³ ;

- Young modulus $E = 207$ GPa ;
- Poisson ratio $\nu = 0.29$.

The first natural frequency of the beam without parametric excitation is found to be $f_1 = 3.9978$ Hz .

The beam is modelled as a single-degree-of-freedom system: this provides an approximate model of the beam and it does not capture the interaction between the axial and the bending motion of the beam.

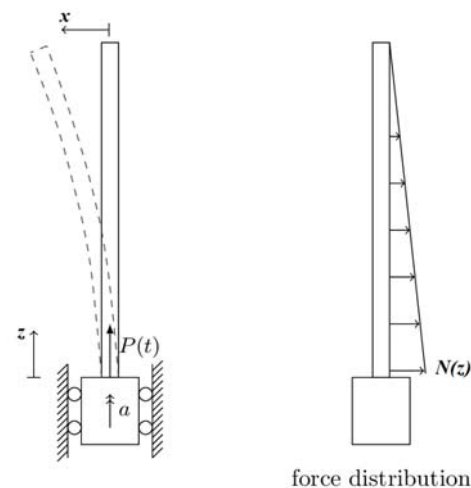


Figure 1 Vertical beam with axes definition and force distribution.

3 NUMERICAL APPROACH

The numerical simulations are carried out on the complete model of a cantilever beam. The stiffness variation is a consequence of the imposed kinematics and a normal force distributes along the beam due to inertial effects.

A parametric software (LUPOS), which is built in Matlab environment, is used to model the system in order to determine the stiffness, damping and mass matrices, to perform modal analysis, and to determining the natural frequencies. The variation of stiffness is modelled in the simulation.

The generic expression of the normal force along the beam is:

$$N(z,t) = AE \frac{\partial u}{\partial z} \quad (3)$$

where A is the cross section, E is the Young modulus and u is the axial displacement, along the z axis.

A solution, for u , with separate variables is considered, as equation (4) shows:

$$u(z,t) = \varphi(z) \eta(t) \quad \text{with} \quad \begin{cases} \varphi(z) = A_1 \cos\left(\frac{\Omega}{c} z\right) + A_3 \sin\left(\frac{\Omega}{c} z\right) \\ \eta(t) = A_2 \cos(\Omega t) + A_4 \sin(\Omega t) \end{cases} \quad (4)$$

where A_i are constants dependent on initial and boundary conditions, Ω is the frequency of the imposed displacement and $c = \sqrt{\frac{E}{\rho}}$ is the sound velocity.

The boundary conditions and the initial ones are as follows:

$$\begin{cases} AE \frac{\partial u}{\partial z} \Big|_{z=l} = 0 \\ u \Big|_{z=0} = Z_0 \cos(\Omega t) \end{cases} \quad \text{and} \quad \begin{cases} u \Big|_{t=0} = Z_0 \\ \frac{\partial u}{\partial t} \Big|_{t=0} = 0 \end{cases} \quad (5)$$

Substituting equation (5) into equation (4) all the constants A_i are determined. The axial displacement is then expressed as:

$$u(z,t) = \left[\cos\left(\frac{\Omega}{c} z\right) + \tan\left(\frac{\Omega}{c} l\right) \sin\left(\frac{\Omega}{c} z\right) \right] Z_0 \cos(\Omega t) \quad (6)$$

and the normal force can be written as:

$$N_0(z) = \frac{AE\Omega}{c} Z_0 \left[\tan\left(\frac{\Omega}{c} l\right) \cos\left(\frac{\Omega}{c} z\right) - \sin\left(\frac{\Omega}{c} z\right) \right] \quad (7)$$

The normal force is maximum at the base of the beam and zero at the other end. The normal force generates an internal stress in the structure, which leads to the stiffness variation.

Proportional damping is considered, so that parametric resonance phenomena are easily detected.

The differential equation using Matlab/Simulink is written in the matrix form as:

$$\begin{aligned} \mathbf{M}_{IKs} \ddot{\mathbf{x}} + \mathbf{C}_{IKs} \dot{\mathbf{x}} + \mathbf{K}_{IKs} \mathbf{x} = \\ = -\mathbf{T}_{IKs}^T \mathbf{M}_{BCs} \ddot{\delta \mathbf{x}}_{im} - \mathbf{T}_{IKs}^T \mathbf{C}_{BCs} \dot{\delta \mathbf{x}}_{im} - \mathbf{T}_{IKs}^T \mathbf{K}_{BCs} \delta \mathbf{x}_{im} \end{aligned} \quad (8)$$

Equation (8) is for the general MDOF system with imposed kinematics. Matrices with IKs subscripts contain only the unknown DOFs. The vectors without subscripts also represent only these DOFs. Matrices with BCs subscripts instead contain all the DOFs: the imposed and the unknown ones, and are obtained from the FEM model. Vectors with *im* subscripts contains only the imposed generalised kinematics DOFs. T_{IKs} is a transformation matrix, and δ contains the relationship between the imposed and the unknown DOFs.

All the matrices are determined from LUPOS. The variation of the stiffness matrix using the harmonic base displacement is written as:

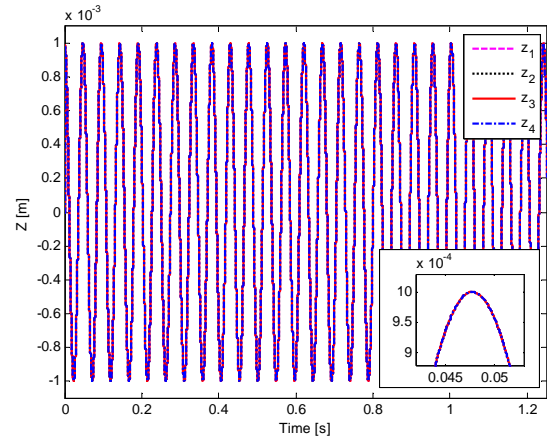
$$\mathbf{K}_{IKs} = \mathbf{K}_{0,IKs} + \sum_i N_{i,0} \Delta \mathbf{K}_{i,0,IKs} \cos(\Omega t) \quad (9)$$

where $\mathbf{K}_{0,IKs}$ is the stiffness matrix without internal stress effect, $N_{i,0} = N_0(z_i)$ are the amplitudes of the normal forces

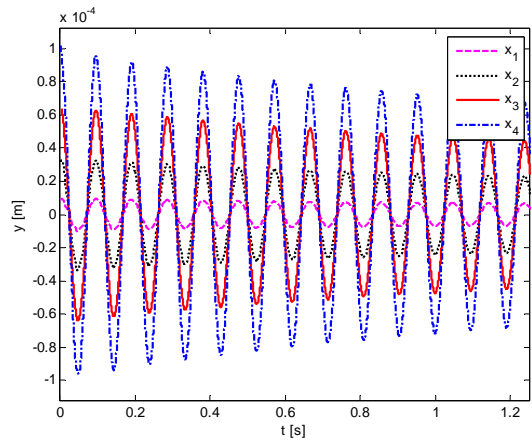
along the generic i^{th} link and $\Delta \mathbf{K}_{i,0,IKs}$ are the matrices containing the effect of an unitary force along the generic i^{th} link.

Figure 2 shows the numerical responses obtained from Lupos at four nodes along the beam in both axial and bending directions when the parametric amplitude of $Z_0 = 1 \times 10^{-3}$ m and the parametric frequency of $\Omega = 2\omega_x$ are considered. The system is stable and the amount of damping in the system can be sufficient to overcome parametric resonance. Increasing the amplitude of the base excitation to $Z_0 = 3 \times 10^{-3}$ m results in destabilisation of the system as can be seen in the bending response in Figure 3(b)

In following figures the locations of the nodes are $z_1 = 1 \times 10^{-3}$ m, $z_2 = 2 \times 10^{-3}$ m, $z_3 = 3 \times 10^{-3}$ m and $z_4 = 4 \times 10^{-3}$ m.

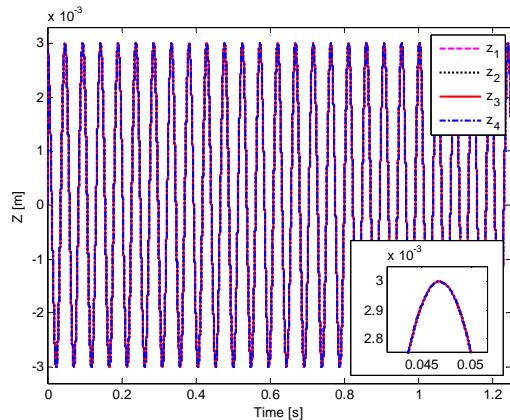


(a)

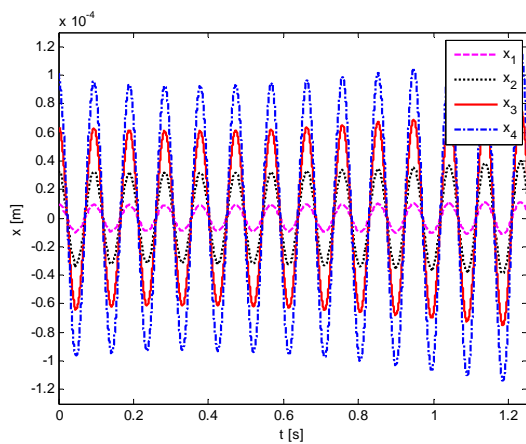


(b)

Figure 2 Time responses in vertical z (a) and horizontal x (b) displacements for $Z_0 = 1 \times 10^{-3}$ m and $\frac{\Omega}{\omega_x} = 2$.



(a)



(b)

Figure 3 Time responses in vertical z (a) and horizontal x (b) displacements for $Z_0 = 3 \times 10^{-3}$ m and $\frac{\Omega}{\omega_x} = 2$.

Simulations are carried out for different values of Z_0 and Ω to provide a map of stable and unstable regions numerically as shown in in Figure 4. Using the numerical method, the transition curves for the higher bending modes of the beam can also be obtained.

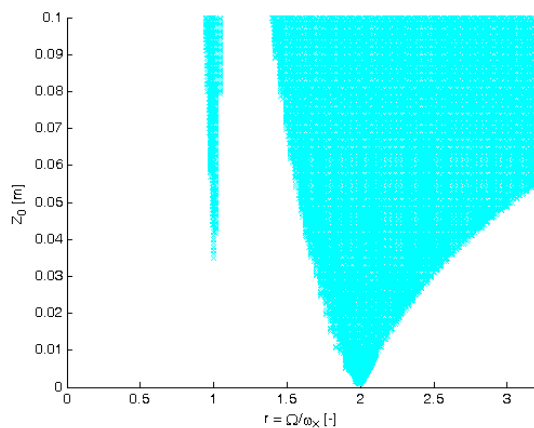


Figure 4 Floquet diagram, numerical.

4 ANALYTICAL APPROACH

The beam is modelled as a two degree-of-freedom system; however, it can be generalised to n-degrees of freedom (MDOF) system. The degrees of freedom correspond to the axial and the bending motion as shown in Figure 2.

The system can be regarded as an autoparametric system and consists of two subsystems, a primary and a secondary subsystem. The primary system is externally forced in axial direction while the secondary subsystem, which describes the bending motion of the beam, is coupled to the primary subsystem due to the internal stresses. The coupling between the two subsystems is represented by the geometric stiffness, which depends on the normal force. The bending stiffness k_x is therefore dependent on the imposed displacement along the axial direction.

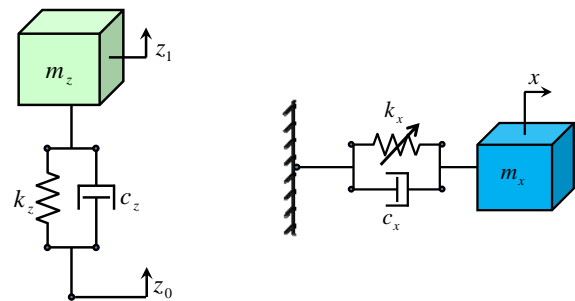


Figure 5 Two degree-of-freedom system corresponding to axial and bending motions.

The dynamic equation of motion in x direction can be written as:

$$m_x \ddot{x} + c_x \dot{x} + k_x(t)x = 0 \quad (10)$$

where m_x , c_x and $k_x(t)$ are the mass, damping and stiffness of the bending DOF.

Imposing the axial displacement, results in the geometric stiffness:

$$k_x = k_{x_0} + N_0 \Delta k_{x_0} \cos \Omega t \quad (11)$$

Neglecting the damping, yields,

$$\ddot{x} + \left(\frac{k_{x_0}}{m_x} + \frac{N_0 \Delta k_{x_0}}{m_x} \cos \Omega t \right) x = 0 \quad (12)$$

The bending stiffness in equation (11) has a constant part (k_{x_0}) and a variable part $N_0 \Delta k_{x_0} \cos \Omega t$, which depends on the amplitude of the normal force N_0 , the excitation frequency Ω , and the variation of stiffness due to a normal unitary force Δk_{x_0} .

Equation (12) is the Mathieu type equation, equation (2), when assuming:

$$\begin{cases} \delta = \frac{k_x}{m_x} = \omega_x^2 \\ \varepsilon = \frac{N_0 \Delta k_{x0}}{m_x} \end{cases} \quad (13)$$

where δ relates to the bending frequency and ε relates to the parametric stiffness.

Considering the axial direction as a SDOF system, the dynamic equation along the z-axis can be written as,

$$m_z \ddot{z}_1 + c_z (\dot{z}_1 - \dot{z}_0) + k_z (z_1 - z_0) = 0 \quad (14)$$

where m_z , c_z and k_z are the mass, the damping coefficient and the stiffness of the axial DOF of the beam.

The normal force hereafter reported can be obtained from simple considerations about the model proposed in Figure 5:

$$N_0 = \frac{m_z \Omega^2 (k_z + ic_z \Omega)}{k_z - m_z \Omega^2 + ic_z \Omega} Z_0 \quad (15)$$

The transition curves in the Floquet diagram can be obtained from solving equation (12) for Z_0 and Ω .

Using the harmonic balance method:

$$x(t) = a_0 + \sum_{n=1}^m a_n \cos \frac{n \Omega t}{2} + \sum_{n=1}^m b_n \sin \frac{n \Omega t}{2} \quad (16)$$

and approximating the response with $m=5$, the transition curves are obtained as shown in Appendix A.

Using equations (12) and (15), the transition curves can be obtained in terms of Z_0 and Ω .

$$\begin{cases} Z_0 = \left(1 - 4 \frac{\delta}{\Omega^2}\right) \frac{\omega_z^2 - \Omega^2}{2\gamma\omega_z^2} \\ Z_0 = \frac{2\delta - \frac{\Omega^2}{2}}{\gamma \frac{\omega_z^2 \Omega^2}{\omega_z^2 - \Omega^2}} \end{cases} \quad (17)$$

where, the parameters in equations (17) are defined as:

$$\begin{cases} \varepsilon = \frac{m_z \Omega^2 (k_z + ic_z \Omega) \Delta k_{x0}}{m_x (k_z - m_z \Omega^2 + ic_z \Omega)} Z_0 \\ \gamma = \frac{m_z}{m_x} \Delta k_{x0} \\ \omega_z^2 = \frac{k_z}{m_z} \\ c_z \approx 0 \end{cases} \quad (18)$$

Figure 6 shows the analytical transition curves for the primary parametric resonance (blue dashed line), together with parametric resonances of higher orders (red solid line).

The cyano points are the ones obtained from the numerical simulation in the previous section, which is in agreement with the analytical approach.

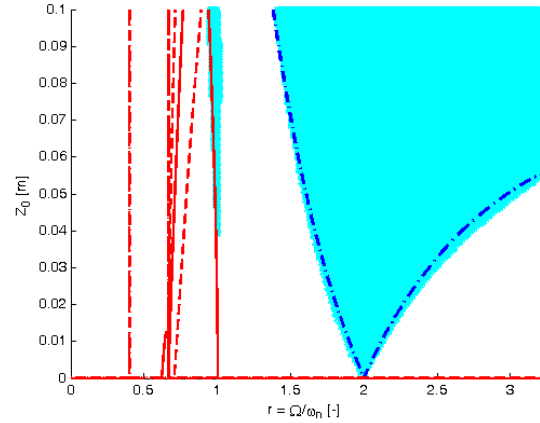


Figure 6 Floquet diagram, numerical (cyan dots) and analytical (blue or red line).

5 EXPERIMENT VALIDATION

A beam is, attached vertically to an electromagnetic shaker, which provides the base displacement along the beam axis as shown in Figure 1. The shaker is driven in an open-loop mode, using an amplifier and an LMS system. It also provides an input voltage to the amplifier of the shaker and it is used for data acquisition. The beam is attached at the centre of the shaker through a plate. Two accelerometers are attached to the beam at each side to maintain symmetry and measure the bending acceleration and one accelerometer is attached to the shaker to measure the axial acceleration.



Figure 7 Experimental beam layout.

To generate parametric resonance, the excitation frequency should be equal to twice the first bending natural frequency of the beam. Modal analysis was carried out to obtain the natural frequencies and the mode shapes of the beam using impact hammer. Several points on the beam were used for impact and the frequency response function (FRF) at each point was constructed, without moving the accelerometers and avoiding system modifications. Figure 8 shows the sum of all the FRFs.

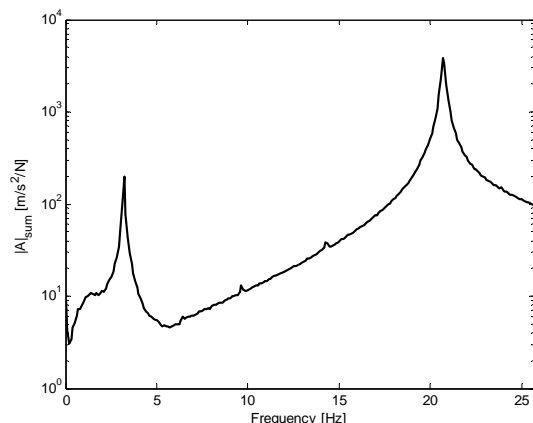


Figure 8 Sum of FRFs to detect natural frequencies.

There are two peaks which correspond to the first two bending modes of the beam. The first natural frequency of the beam is $f_1 = 3.2031\text{Hz}$ and the second is $f_2 = 20.6703\text{Hz}$. There are small peaks between the two modes of the beam, which could be related, possibly to the shaker modes or to the local modes of the structure. The first two mode shapes were identified using *polymax* method.

The above described conditions are closer to an applied force, but it is simple to find the Floquet diagram with F_0 as function of Ω , using equation (19):

$$N_0 = \frac{k_z + ic_z \Omega}{-m_{z0} \Omega^2 + k_z \left(\frac{m_{z0}}{m_{z1}} + 1 \right) + ic_z \left(\frac{m_{z0}}{m_{z1}} + 1 \right) \Omega} F_0 \quad (19)$$

The accelerometers add lumped masses to the beam and even their wires can have some nonlinear effects on the response. The fixture and the shaker also can contribute to non-linearities and are non-ideal constraints. All these factors can result in variations of system parameters, which makes the comparison between the real data and the numerical ones quite complicated, since the transition curves in the Floquet diagram are sensitivities to the system parameters.

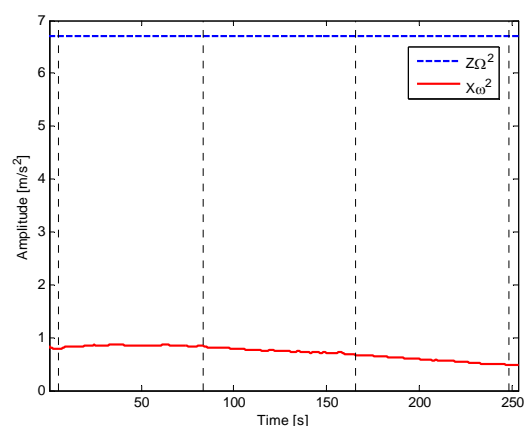
To observe parametric instability experimentally, several experiments were carried out with different excitation frequencies (f [Hz]) and magnitudes (A [V]). The relation between the magnitude of the electric signal sent to the shaker and the force applied to the base of the beam is

obtained from the measured acceleration at the base of the shaker. An initial deflection was given to the beam and the accelerations were measured when the shaker was exciting the beam in the axial direction.

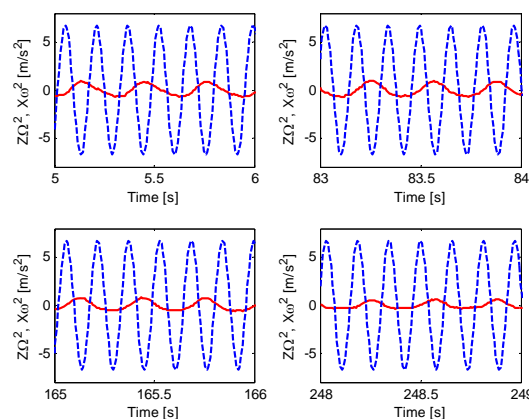
The experimental results show that the system is very sensitive to the frequency of the external excitation.

Figure 9 shows the evolution of the response at an excitation amplitude of $A=1.0\text{V}$ and frequency of $f = 6.400\text{Hz}$, with no parametric instability. The amplitude of the response decays, although at slow rate. It is worth noting that frequency contents have sub- and super-harmonics corresponding to non-single harmonic behaviour.

Figure 9(a) shows the amplitude of the two acceleration signals. Figure 9(b) shows the several time recorded data at different intervals to highlight the evolution of the acceleration signal, both in terms of the amplitude and phase. The blue dashed line is the measured axial acceleration of the beam and the red solid line represents the response of the beam in the bending direction. It can be seen that the beam responds at half of the excitation frequency.



(a)



(b)

Figure 9 Amplitude of accelerations (a) and highlighted accelerations (b). $A=1.0\text{V}$ and $f = 6.400\text{Hz}$.

Figure 10, corresponds to the increase of the excitation frequency by only 5mHz, which is less than 0.08%, indicating the parametric resonance phenomena and increasing of the bending amplitude. No limit cycle oscillation is observed, during the 256 seconds of the recorded data.

Figure 11 shows that, increasing the magnitude of the excitation to $A=3.0V$, parametric resonance occurs at a wider range of frequencies (here $f = 6.380Hz$ is used). Moreover, limit cycle oscillations are observed, due to the large displacements of the beam, leading to nonlinear behaviour. In this case, a steady state condition is reached, since the amplitude is not growing anymore.

CONCLUSION

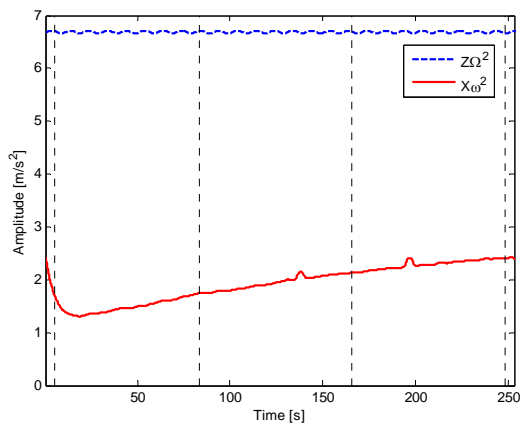
Jia *et al* [7] presented that significant amount of energy can be harvested when parametric resonance is used, about ten times more than the non-parametric case. In addition the frequency bandwidth in which the energy can be harvested is extended as well, especially when parametric resonance is applied together with the direct resonant principle.

Reducing the threshold due to damping phenomena is a key spot to be able to harvest even small vibration amplitudes.

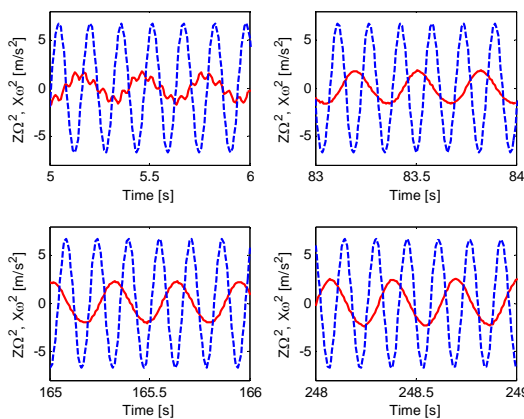
Using piezoelectric actuators, in order to change the bending stiffness of the system, could be helpful to tune the device according to excitation characteristics. This can possibly result in a wider harvestable frequency band and in a more efficient exploitation of the provided energy. Considering the nonlinearities and their effects, in fact, it could be possible to tune the device increasing the bending amplitude in steady state conditions, besides increasing the range of working frequencies.

Energy can be harvested using piezoelectric, electromagnetic or electrostatic approach. The last approach, according to [8], gives a magnitude lower peak power density.

Using piezoelectric approach the harvesting part should be implemented close to the base of the beam, where the strains are maxima. Contrariwise, using electromagnetic approach, it is more profitable to use the free end of the beam, where the displacement is maximum and rare-earth materials allow high power density.

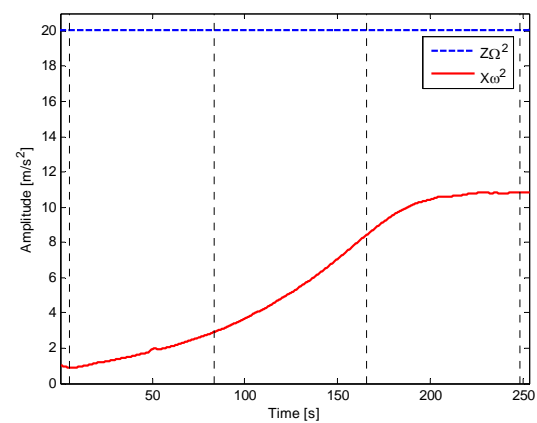


(a)

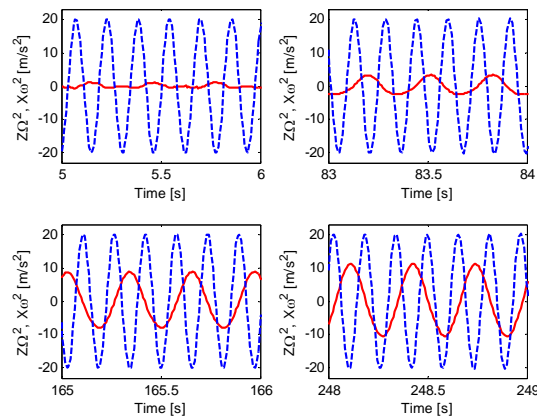


(b)

Figure 10 Amplitude of accelerations (a) and highlighted accelerations (b). $A=1.0V$ and $f = 6.405Hz$.



(a)



(b)

Figure 11 Amplitude of accelerations (a) and highlighted acceleration (b). $A=3.0V$ and $f = 6.380Hz$.

REFERENCES

- [1] Faraday M., On a peculiar class of acoustical figures and on certain forms assumed by a group of particles upon vibrating elastic surfaces. *Philosophical Transactions of the Royal Society of London*, 121, 1831, pp. 299-318.
- [2] Mathieu E., Mémoire sur le mouvement vibratoire d'une membrane de forme elliptique. *Journal de Mathématiques Pures et Appliquées*, 13, 1868, pp. 137-203.
- [3] Nayfeh A. H., Mook D. T., *Nonlinear oscillations*, John Wiley & Sons Inc., 1979.
- [4] Zavodney L. D., Nayfeh A. H., Sanchez N. E., The response of a single degree-of-freedom system with quadratic and cubic non-linearities to a principal parametric resonance. *Journal of Sound and Vibration*, 129, 1989, pp. 417-442.
- [5] Oueini S. S., Nayfeh A. H., Single-mode control of a cantilever beam under principal parametric excitation. *Journal of Sound and Vibration*, 224(1), 1999, pp. 33-47.
- [6] Ghandchi Tehrani M., Kalkowski M. K., Elliott S. J., Active control of parametrically excited systems. *Journal of Intelligent Material Systems and Structures*, submit on July 2014.
- [7] Jia Y., Seshia A. A., Directly and parametrically excited bi-stable vibration energy harvester for broadband operation. *Solid-State Sensors, Actuators and Microsystems*, 2013, pp. 454-457.
- [8] Jia Y., Yan J., Soga K., Seshia A. A., Parametrically excited MEMS vibration energy harvesters. *Digest Tech. Papers Power MEMS '12*, 2012, pp. 215-218.

DEVELOPMENT OF AN ENVIRONMENTAL CONTROL SYSTEM PACK SIMULATION MODEL FOR A MORE ELECTRIC AIRCRAFT

Paolo Maggiore Matteo D. L. Dalla Vedova Lorenzo Pace Marco Tosetti Andrea Piovano

Department of Mechanical and Aerospace Engineering, Politecnico di Torino

ABSTRACT

The aim of this work has been to develop a robust design methodology for the sizing of an electric powered, no-bleed, environmental control system pack for More Electric aircrafts. The results of the design have been tested through virtual verification, and a one-dimensional (1D) simulation model of the entire machine has been created. Starting from the definition of the design requirements, we have proceeded with the analytical sizing, the choice of the components, the 3D digital mock-up of the machine and with the 1D simulation of the system. Finally we have executed a fluidic and thermal analysis of the heat exchangers duct.

Keywords: Electrical environmental control system (E-ECS), Cold Air Unit (CAU), Bleedless system

1 TITLE OF SECTION (E.G. INTRODUCTION)

This work deals with an Environmental Control System (ECS). The ECSs currently found onboard airliners need bleeding of the high pressure air from the engine compressor. However, the More Electric Aircraft configuration includes a bleedless Electrical ECS (E-ECS) [1]. The advantages of a bleedless architecture should be taken into account: first of all, the elimination of the pneumatic system, with all the critical bleed systems, would allow a greater modularity of the conditioning unit, with a reduction in the operating and maintenance costs. In addition, a bleedless configuration does not penalize the overall performance of engines. The goal of the future is to reduce engine fuel consumption. A current disadvantage, however, is the weight of the electric motors and the related power electronics. A design methodology for the dimensioning of an E-ECS will be presented in the following of this paper. The task of the air conditioning and pressurization system is to maintain comfortable conditions on board during all the flight phases in terms of pressure, temperature, chemical composition of the air and humidity.

Modern systems are designed with an open cycle architecture, with partial air recirculation. The core of the system is the environmental control group, which is made up of the Cold Air Unit (CAU) and the hot bypass. The configuration of the group that we intend sizing is bootstrap subfreezing type, with electric compressors. A centrifugal water separator extracts the condensed water upstream of the turbine, and allows expansion to tens of degrees below zero, thus preventing the formation of ice on the blades. This leads to a reduction in the required flow rate and therefore in the CAU size [2]. In order to complete the architecture, it is necessary to add the condenser and a reheater. The cooling air in the heat exchanger duct is moved by the dynamical effect of a NACA intake during the flight and by an electro-fan when the airplane is stationary or moving at low speeds.

2 DESIGN REQUIREMENTS

The first step in the sizing process is the definition of the CAU design requirements. The two packs have to ensure environmental control of the case study, which is a 100 seater regional jet. In particular, the sizing should be conducted considering two extreme environmental conditions: hot weather at sea level, in the equatorial zone, and cold weather at an altitude of 11000 [m]. The ECS pack has to maintain comfortable environmental conditions on board: the comfort intervals must be respected in terms of

Contact authors: Lorenzo Pace¹, Matteo Dalla Vedova²

Corso Duca degli Abruzzi 24 – 10129, Turin, Italy

Email: ¹lorenzo.pace@polito.it

²matteo.dallavedova@polito.it

pressure, temperature, relative humidity and chemical composition. Finally, the ECS group should be designed to be interfaced with a mixer unit that mixes the charge air with the recirculating flow, which is filtered and conditioned by two vapour cycle CAUs. Recirculation is advantageous as it allows a smaller external air flow rate.

Furthermore, it also keeps the relative humidity around acceptable values (~20%) without having to remoisten the dry air generated by the bootstrap cycle. The design requirements for the ECS packs are:

1. Regional jet, 100 passengers
2. Extreme external environmental conditions.

$$z = 0 [m]; p = 1.01325 [bar]; T = 45 [^{\circ}C]; h_{rel} = 80\% \quad (1)$$

$$z = 11000 [m]; p = 0.227 [bar]; T = -56 [^{\circ}C]; h_{rel} = 10\% \quad (2)$$

3. Comfortable condition intervals to be maintained on board:

$$0.7446 [bar] < p < 1.2 [bar]$$

$$10\% < h_{rel} < 35\% \quad (3)$$

$$18 [^{\circ}C] < T < 25 [^{\circ}C]$$

4. Bleedless system architecture, with electrical ECS packs
5. Mixer unit interface

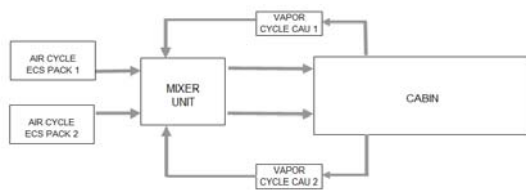


Figure 1. The More Electric ECS configuration.

3 THERMAL POWER BALANCE FOR MAXIMUM COOLING NEEDS

As requested by design requirements, the next step is the calculation of the air mass flow rate to be sent into the passenger cabin, in case of hot environmental conditions.

The environmental boundary conditions are: $z = 0 [m]$, $p = 0.1325 [bar]$, $T = 45 [^{\circ}C]$, $h_{rel} = 80\%$. The first step in CAU sizing is to evaluate the thermal power balance of the entire aircraft, with the final target of evaluating the required flow rate, for each ECS pack.

According to the section 831(a) of the *JAR-25 standard*, for civil aircraft, the minimum fresh air flow rate to ensure input to the cabin is $0.55 [lb/min]$ for each passenger; the global requirement for 100 passengers, including the crew, is therefore a minimum fresh air flow rate of $415 [g/s]$, $207.5 [g/s]$ for the single ECS pack. We thus have a reference value, a requirement to be met, in terms of minimum flow rate.

The authors proceed by calculating this rate in maximum cooling requirement condition on a hot day: the air flow rate relative to the maximum cooling need is greater than in the case of maximum heating need, therefore the former is taken into account for the ECS pack sizing.

The total thermal power exchanged throughout the cabin can be considered as the sum of four contributions [2]: Q_w thermal power entering through the fuselage walls and through the windows, Q_m metabolic thermal power produced by the passengers (empirical formula), Q_e thermal power dissipated by the electrical loads (lights, avionics, entertainment) and Q_s solar radiation that enters through the windows (the side directly exposed to the sun and the shaded side with reflected infrared radiation). Q_w is evaluated via the overall wall heat transfer coefficient U_{wall} . After a preliminary estimation of the external surface area of the aircraft S , it is possible to calculate the overall heat transfer coefficient for fuselage walls, U_w :

$$U_w = U_{wall} \cdot S = 857.5 [W / K] \quad (4)$$

in which h_i is the internal and h_e the external coefficient of convective heat transfer values, from which it is possible to evaluate the overall wall heat transfer coefficient U_{wall} .

The same methodology used for the walls is adopted for all the aircraft transparencies, but first it is necessary to evaluate the total area of passengers' and pilots' windows: 62 $10 \times 15 [inch]$ rectangular windows have been considered. Reference is made to the B737 dimensional drawing to calculate the surface area of the cockpit windows:

$$U_T = U_{trasp} \cdot S = 55.5 [W / K] \quad (5)$$

An estimation of the electrical loads (lights, entertainment, galleys and avionics) puts the power dissipation for a state of the art regional jet, with 100 passengers, at about $\dot{Q} = 10 [kW]$. The metabolic thermal power dissipated by an adult passenger is usually between 70 and 100 $[W]$. The power dissipated by each passenger depends on the environmental temperature inside the cabin. A dissipated power of 100 $[W]$ is conservatively assumed for each passenger. The incoming solar thermal power from solar radiation can be calculated through the formula [3]:

$$Q_s = A \cdot \tau \cdot Q_{si} \quad (6)$$

$$A = \text{total transparencies area } [m^2]$$

$$\tau = \text{transmittance} = 0.83$$

$$Q_{si} = \text{solar radiation incidence } [W/m^2]$$

The incident solar radiation has different values, which depend on the angle of incidence on the surface of the windows. As a first approximation, a maximum standard value is assumed for the window side directly exposed to the sun, and a minimum value for the indirectly exposed side. Once all the contributions have been gathered, it is possible to evaluate the heat balance for a hot day:

$$Q_i = Q_w + Q_e + Q_m + Q_s \quad (7)$$

This provides a total thermal power entry of about 40 $[kW]$.

4 MASS FLOW REQUIREMENT FOR MAXIMUM COOLING NEEDS

It is now possible to evaluate the air flow required to enter the cabin through the distribution system for the air conditioning task. The input air temperature through ventilation inlets T_{inlet} , is fixed at 25 [°C] and the air temperature into the cabin T_{cabin} at 4 [°C].

The total required flow rate may be evaluated by means of the following formula:

$$\dot{m}_p = \frac{Q_t}{c_p \cdot (T_{cab} - T_{in})} \quad (8)$$

where T_{in} is the minimum temperature of the cabin inlet, which should not cause discomfort for the passengers. The inlet temperature to the cabin is usually maintained above zero in order to avoid the formation of ice crystals on the inlet nozzles. Adding a margin of 10%, in order to compensate for any loss of flow rate in the valves or in the joints of the ducts, a total required cooling flow of about 2054 [g/s] is obtained. Assuming the possibility of a recirculating flow, the global flow rate is calculated as the sum of the flow delivered by the air cycle CAUs and of the flow controlled by two circulation systems:

$$\dot{m}_p = \dot{m}_{CAU_a} + \dot{m}_{ric} \quad (9)$$

Only half of the total cabin air is removed in modern aircrafts, while the remaining half is filtered through high efficiency filters. The filters remove all particles greater in size than 0.3 μm : this means that the recirculation air does not contain bacteria, viruses or other solid particles. The air recirculation leads to a decrease in fuel consumption and makes the flight more economical and environmentally friendly. An algebraic system with two unknowns is obtained from thermal power and flow rate balance at the mixer unit: the total flow rate developed by the air cycle CAUs, \dot{m}_{CAU_a} , and the recirculating flow rate, \dot{m}_{ric} , developed by the vapor cycle CAUs. Once the total flow rate is known and the desired temperatures are imposed, it is possible to calculate the two unknowns [3]:

$$\begin{cases} \dot{m}_{ric} = \frac{\dot{m}_T \cdot T_i - \dot{m}_T \cdot T_{CAU_a}}{(T_{ric} - T_{CAU_a})} \\ \dot{m}_{CAU_a} = \dot{m}_T + \dot{m}_{ric} \end{cases} \quad (10)$$

As previously mentioned, the architecture includes two air cycle CAUs to pressurize and condition the outside air, and two vapour cycle CAUs to condition the circulating air. Both types of ECS packs are powered electrically, as the More Electric Aircraft concept is implemented [1].

$$\dot{m}_{singleCAU_a} = \frac{\dot{m}_T + \dot{m}_{ric}}{n^\circ ECS_{packs}} = \frac{\dot{m}_{CAU_a}}{2} \quad (11)$$

The flow rate managed by the single ECS pack, on a hot day has an approximate final value of 395 [g/s].

5 THERMAL POWER BALANCE FOR MAXIMUM HEATING NEEDS

Maximum heating requirements are found for a flight at the altitude of 11000 [m], at Mach = 0.78; however, as proved before, this does not influence the machine sizing as much as the cooling requirement. As in the previous case, a balance of thermal power is necessary to establish the input hot air flow rate to the cabin requirement [2]:

$$\begin{cases} \dot{m}_i = \dot{m}_{CAU_a} + \dot{m}_{by_pass} + \dot{m}_{ric} \frac{\dot{m}_T \cdot T_i - \dot{m}_T \cdot T_{CAU_a}}{(T_{ric} - T_{CAU_a})} \\ T_i = \frac{\dot{m}_{CAU_a} \cdot T_{CAU_a} + \dot{m}_{by_pass} \cdot T_{by_pass} + \dot{m}_{ric} \cdot T_{ric}}{\dot{m}_{CAU_a} + \dot{m}_{by_pass} + \dot{m}_{ric}} \end{cases} \quad (12)$$

with T_i equal to about 50 [°C].

The most relevant term is that of the thermal power exiting through the fuselage walls and through the windows. Once the total exiting thermal power has been estimated (~28 [kW]), it is possible to estimate the global flow rate into the cabin, by imposing an internal temperature of 18 [°C] and a temperature of the input flow of 50 [°C]. From a balance of the thermal power and flow rate, across the mixer unit, three unknown flow rate values are obtained, as the hot bypass has to be added. However, by fixing the percentage recirculation value at 50%, a system in two unknowns (the air cycle flow rate and the bypass one) can be solved; a flow rate of 217 [g/s] means a lower requirement than the hot condition case, at sea level.

6 CENTRIFUGAL COMPRESSORS CHOICE

Once the flow rate managed by the single CAU has been defined, the single-stage centrifugal compressors can be selected for both applications: electric compressors group and Air Cycle Machine (ACM) group. The most extreme environmental conditions of the airplane are analysed, in order to choose the most suitable compressors for both cases. The target pressure in the cabin is that related to an equivalent altitude of $z = 1800$ [m]. The cabin pressure should not be lower than an equivalent altitude of $z = 2400$ [m]. In the previous section, the flow rate controlled by an ECS pack under maximum cooling conditions was calculated as 395 [g/s]; assuming the parallel use of two centrifugal compressors, a flow rate of 197.5 [g/s] has been determined for each ECS pack. It has been observed, from numerous tests carried out on preliminary AMESim® models of the CAU, for such extreme environmental conditions, that the ACM turbine expansion is only effective if the pressure at the inlet of a realistic turbocharger is set at about 4 [bar]. The p_1/p_0 , T_1/T_0 , and p_2 target values being known (where p_0 and T_0 are standard conditions, at sea level), it is possible to calculate the corrected mass flow rate controlled by the compressor and the required compression ratio:

$$\dot{m}_{corr} = \dot{m} \cdot \sqrt{T_1/T_0} \div (p_1/p_0) \quad (13)$$

It is now necessary to look for a family of centrifugal compressors which meet the flow rate and compression ratio requirements. To this purpose, the authors have selected a compressor map to set the 1D simulation submodel and to find the working points of the machine: a centrifugal single stage turbocharger, that is compatible with the previously described requirements, has been chosen. The corrected mass flow rate and the compression ratio required for each compressor are:

$$\dot{m}_{corr} = 207.4 [g/s] ; \beta_c = p_2 \div p_1 = 3.95 \quad (14)$$

The selection has been performed taking into account the required performances even for the case of maximum heating requirement: the compressor that is considered suitable to provide these performances will have to work in a particular range of corrected mass flow rates, and compression ratios, in order to satisfy the maximum needs of cooling and heating. The selected compressors have operating maps that ensure the desired range of corrected air flow rate (400-800 [g/s]) and the desired compression ratios. The corrected speed is compatible with an electric induction motor drive. The compressor maps are now manually converted into data files in order to set all the submodels for the 1D simulation of the entire machine. The working points of the electric compressors are computed by means of the 1D software, superimposing the compressor map onto the external characteristic curve of the circuit. The hypothesized operating point corresponds to a corrected rpm of $n_{corr} \approx 97000 [rpm]$. Once the corrected speed and the temperature ratio are known, it is possible to calculate a required impeller physical speed of:

$$n = n_{corr} \cdot \sqrt{T_1/T_0} = 100340 [rpm] \quad (15)$$

If the real gas transformation in the compressor is approximated with a polytropic evolution, it is possible to calculate the internal compression work, per unit mass. Assuming a mechanical efficiency of $\eta_m = 0.95$, it is possible to estimate, for the hot environmental condition, an absorbed power of:

$$P_{ass} = \frac{\dot{m} \cdot L_c}{\eta_m} = 45 [kW] \quad (16)$$

At maximum cooling needs, the required power is 23 [kW].

7 HEAT EXCHANGERS SIZING

It was decided to size the simplified heat exchangers by means of the *log mean temperature difference* (LMTD) method, in order to obtain predetermined thermal jumps. The exchanged thermal power is expressed as the product of the thermal capacity of each fluid, per time unit, for the temperature variation, but can also be expressed as the product of the medium overall coefficient of heat exchange, for the heat exchange surface area, for the LMTD [4,5]:

$$\dot{Q} = c_{p_c} \cdot \dot{m}_c \cdot \Delta T_c = c_{p_h} \cdot \dot{m}_h \cdot \Delta T_h = U \cdot A \cdot \Delta T_{ml} \quad (17)$$

The experimental methodology first provides the initial setting of the AMESim® models of these components: geometry and effectiveness data from the state of the art of air to air heat exchangers and testing values of mass flow rates can be used for the first simulations. The 1D simulation allows a fast calculation of the first heat exchanger outlet temperature values; subsequently, the LMTD is analytically calculated, using a correction factor F that is derived from the experimental diagram of the cross-flow heat exchangers.

Once the heat exchange area has been calculated, the number and perimeter of each tube, with a rectangular section, can be decided on; the heat exchanger thickness (precooler, intercooler, reheater, condenser) can be estimated. After the first simulations, the thickness values are not compatible with the machine compactness requirement, so the circular procedure is restarted, with more tubes and hypothetical new flow rates.

The sized geometry of the heat exchanger duct is then converted into a CAD drawing for the CFD analysis. Meanwhile, a digital mock-up of the entire ECS group is created in order to have an overall view of a possible installation of all the components.

8 1D MODELING AND ANALYSIS

The one-dimensional lumped parameter model concerning the ECS group is now developed. The used software is based on the bond graph approach, a technique which allows one to study the dynamic interactions between domains belonging to different physical systems, through simple power balances [6].

The physical submodel parameters of all the components have been set on the basis of the maps and geometries that were studied in the sizing procedure. The air inlet is a source of moist air at high pressure and temperature, like a simple engine bleed. The choice of a single cooling duct has determined the series arrangement of intercooler and precooler; the ACM has been integrated in the circuit by means of a rotating transmission shaft. The subfreezing pattern is completed by condenser, reheater and water separator. Two electric compressors have been included with their operating maps.

The next step is the incorporation of simple automatic regulation systems to adjust the temperature level and mass flow rate, through proportional-integrative gains (PI). The regulation of the temperature flow, exiting from the ECS group, acts directly on the opening/closing of the hot air bypass valve. The flow rate regulation system, which is essential for the modulation of the target pressure and aeration in the cabin, requires a certain number of rpm for the electric motors that drive the compressors.

The fan, at the end of ram air duct, is modelled through a 1D pneumatic source flow. Running the 1D simulation model, in the two extreme environmental conditions, it is possible to evaluate the system ability to satisfy the project requirements. In the case of maximum cooling needs, the

outlet flow from the pack reaches the desired temperature, pressure and mass flow rate values in a few tens of seconds. The system regulating the mass flow rate level allows the physical speed of the two compressors which determine the desired flow rate to be automatically calculated. Even in the case of cold environmental conditions, the regulation system brings the temperature and mass flow rate to the required values. The initial jumps in the physical magnitude trends are due to the hot bypass, that is activated 5 [s] after the electric motors start.

It has been observed as the outlet pressure reaches 0.8140 [bar], equivalent to an altitude of 1800 [m], which fulfils the requirement of minimum pressure on board.

9 CFD ANALYSIS AND CONCLUSIONS

Finally, a computational thermo-fluid dynamics analysis has been performed on the cooling duct of the first and second heat exchangers. The objective was to compare the results of the analytical sizing method (and 1D simulation) with CFD ones, and to optimize the geometry of the duct.

Due to high computational costs, it was decided to only simulate the cooling side of the heat exchangers, while the hot side, relative to the charge air flow, was simply described through a constant heat flow, uniformly distributed over the thermal exchange surface. Thus the authors have preferred to simulate the cooling duct flow in order to optimize the distribution of fluid in the heat exchangers zone.

Pre-processing, processing, and post-processing phases have been performed through a CFD solver, CD-adapco STAR-CCM+®. The pre-processing phase [7] generates an unstructured calculation mesh and splits the fluid domain into polyhedral cells. A mesh thickening is set in the heat exchange area, where there is a transition to turbulence, in order to regularize the propagation of the volume cells. Prismatic layers are opportunely set on the wall to describe the kinetic and thermal boundary layers. A mesh sensitivity analysis has been carried out.

After the generation of the mesh, the boundary conditions are set: mass flow inlet for the duct entry, to simulate the flow accelerated by the electric fan, pressure outlet, for the exit, and heat flux on the precooler and intercooler. The extreme environmental condition simulated is the hot one, considering the aircraft standing on the runway: the physical model of the fluid is defined.

The iterative calculations are run in the processing phase, simultaneously monitoring the convergence of the iterative calculation residues and of the physical quantity values (p, T, \dot{m}) mediated in various sections of the cooling duct. Finally, the simulations results are compared in terms of average temperature at the outlet section of the cooling duct.

The expected temperature, according to the LMTD sizing method and relative 1D simulation, is 456 [K]. The CFD monitor plot shows a regime temperature of 442 [K] (area averaged value).

However, it should be taken into account that the results are influenced by different factors: the analytical sizing is affected by the correction factor F for experimental cross-flow heat exchangers, while the CFD analysis accuracy is affected by the mesh refinement level and by the simplifying assumption of constant heat flux.

Nevertheless, it is possible to say that the results of the analytical 1D calculation and CFD simulation are in good agreement, with a deviation of less than 5% (Fig. 2 and 3).

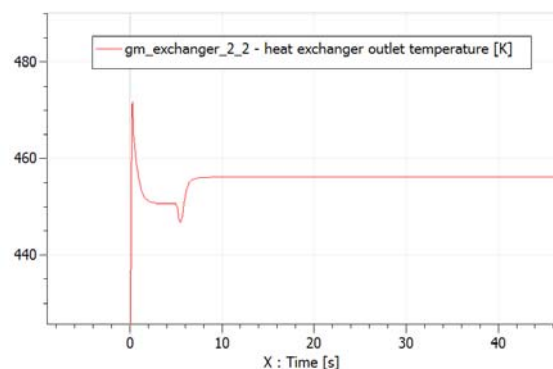


Figure 2. Heat exchanger duct outlet temperature (1D)

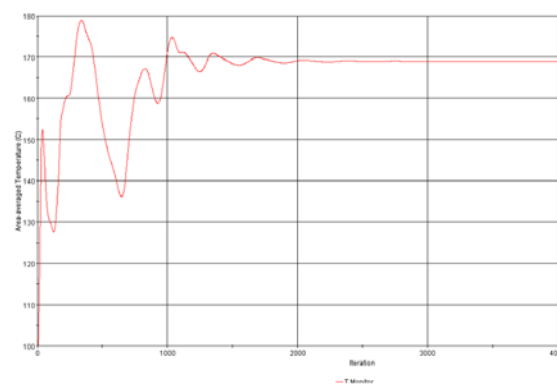


Figure 3. Heat exchanger duct outlet temperature (CFD)

REFERENCES

- [1] Rosero J.A., Ortega J.A., Aldabas E. and Romeral L., Moving towards a more electric aircraft, *Aerospace and Electronic Systems Magazine IEEE*, Vol. 22 No. 3, 2007.
- [2] Chiesa S., *Impianti di bordo per aeromobili: impianti pneumatico, condizionamento, anti-ghiaccio e A.P.U.* C.L.U.T, Torino, 1995.
- [3] Rebecchi B., *A Review of aircraft cabin conditioning for operations in Australia*. Aeronautical Research Laboratories, Melbourne, Victoria, Australia, 1980.
- [4] A.Çengel Y., *Introduction To Thermodynamics And Heat Transfer*. McGraw-Hill, New York, 1997.
- [5] Shah R.K., *Fundamentals of heat exchanger design*. John Wiley & Sons, New Jersey, 2003.
- [6] LMS Imagine, *AMESim Rev. 9 Reference Manual*. 2009.
- [7] Cd-Adapco, *Star-CCM+ User Manual*. 2010.

MBSE MODELLING ENVIRONMENT AND MULTI-OBJECTIVE OPTIMIZATION OF THERMAL CONTROL STRATEGIES FOR MULTIFUNCTIONAL STRUCTURES

Michele Cencetti Eleonora Zeminiani Paolo Maggiore Matteo D. L. Dalla Vedova

Mechanics and Aerospace Engineering Department – Politecnico di Torino

ABSTRACT

A thermo-mechanical-electronic multifunctional structure prototype has been modelled and optimized through the use of Model Based System Engineering (MBSE) platform. The model focuses on the description of thermal and electrical phenomena, but leaves aside structural issues. It couples a 3D thermal network with representations of different possible thermal control laws, namely ON-OFF control, proportional logic, proportional-integral-derivative strategy, and the usage of Positive Temperature Coefficient heaters. The parametric model has been already validated and correlated through a comparison with simple physical solutions, and then with the actual results of a thermal-vacuum test. A model-based approach has been used to model and properly define the main features of the overall problem. Multi-objective optimization (based on genetic algorithms) has then been used to define the best heater layout options, to identify the best control strategy in terms both of panel isothermia and energy consumption, and finally to fine-tune the parameters of the selected control strategy. In particular the main objective focused also on the use of a model-based modelling environment for the definition and set-up of an optimization problem. The study has led to the definition of an optimal thermal control solution. The optimization results show that the simultaneous adjustment of the geometrical layout, as well as the control strategy and its parameters can lead to significant energy savings.

Keywords: Multi-objective Optimization, Thermal Control, System Modelling, Multifunctional Structures

1 INTRODUCTION

This paper presents the results of a research study related to the use of a Model Based System Engineering (MBSE) environment for a multi-objective optimization applied to the thermal control of Multifunctional Structures (MFSs), as reported in [37]. The main aim of this work concerns the feasibility of such connection in order to assess actual advantages and possible drawbacks. Over the last few years the design phases of space systems and equipment have begun to play an increasing key-role in the development of effective products. This situation is mostly due to the increased call for more complex missions beside reduced development time and costs.

At the same time the projects requirements often enforce that risks and quality should be kept at a high standard levels. On the basis of previous considerations an effective definition of system design in the preliminary project phases becomes even more important. In this particular context the MBSE methodology shows promising capabilities for the management of system complexity, making the integration easier across different domains, improving also the related collaboration (e.g. through the traceability of requirements) [1] and [2]. One of the main improvements related to a Model-based approach is the sharing of a unique system model between different disciplines. This feature allows softening all the problems that come out from data exchange process. MBSE emerging technology addresses more resources on system capabilities analysis with the opportunity to enhance even more its performances. Currently many efforts are directed towards a definition of a well-established system data structure from the first preliminary designs to the more

Contact author: Paolo Maggiore

Corso Duca degli Abruzzi, 24 – 10129 Torino Italy
Email: paolo.maggiore@polito.it

advanced ones. The effective integration of design variables trade-off or optimization studies over various domains is one of the most challenging research topics.

Analyses of this type need also to be realized during the advanced development phases when the design architecture is more detailed but there are still some project variables that may be chosen. At the current time there is not a well-defined and scalable process for the evaluation of system performances and requirements verification from the initial phases to the advanced ones. From a model-based point of view MDO methods can be used to assess the overall system performances, pointing out the improvements that may be achieved [3], [4] and [5]. The activities related to the evaluation of the methodology, procedures and tools to be implemented and used are now one of the most interesting topics within the System Engineering (SE). Basically, MFSs are components that cover many roles within a single piece of hardware, shading the clearly defined boundaries that characterize traditional subsystems. Generally speaking, MFSs have already proved to be a promising technology, especially in aeronautics and space fields [11]. Various MFS solutions have been evaluated not only for demonstration satellites [12] and [13], but also for aeronautic systems (mainly, antennas) and UAV (Unmanned Aerial Vehicle) systems [14]. Many kinds of multifunctional structures exist, and they can be classified on the basis of the subsystems they integrate together: it is possible to cite thermo-structural panels, radiation hardened structural panels, and structural panels with embedded batteries [15] and [16] and/or electronics [17] as examples. The case study considered in this paper refers to a demonstrator breadboard called ABB (Advanced Bread Board), which can be seen in Figure 1.

ABB can be classified as belonging to a particular group of an extensive family of MFS, that is, of thermo-structural panels with distributed electronics and a health monitoring network. The system consists of a high thermo-mechanical performance Carbon/Carbon sandwich panel equipped with two independent and symmetrical monitoring circuits. Each monitoring circuit is composed of a motherboard made with Polyimide flex circuitry technology, a flat and flexible ribbon cable, 37 commercial Dallas DS18B20 thermal sensors and several electronic items (mainly surface mounted on the motherboards) to supply energy and manage the sensors themselves. Wires are substituted by copper strips embedded in the printed circuits. The monitoring subsystems are based on Dallas 1-Wire protocol

and are therefore able to read the chain of direct-to-digital temperature sensors available throughout the panel thanks to a single flat ribbon cable including just two copper strips and built with the same technology of the motherboards.

The overall dimensions of the rectangular substrate panel are $1000 \times 500 \times 21.5$ mm. The motherboards measure 150×150 mm each, they are flexible and very thin ($45 \div 47$ μm). Heaters are added on each motherboard in order to simulate thermal loads as well as to protect the surrounding circuitry during cold conditions in thermal tests. A DC/DC converter feeds the three heaters directly embedded on each motherboard. Five additional heaters have been added on the upper face of the panel, in order to control the temperature distribution on the upper skin and maintain the electronics in its operational range. The ABB demonstrator was manufactured and tested in 2010 [18].

The scope of this work was to speculate upon the ABB concept, by investigating further developments that could improve the design of this class of multifunctional structures, assessing at the same time the use of a model-based approach for the management of all the related data. In particular such an approach has been used to enhance the thermal control performance of the outer smart layer of the ABB, in order to both reduce the amount of energy required and obtain a uniform in-plane temperature distribution. This objective has been pursued adopting multi-objective optimization techniques [19], [20] and [21]. Over the last two decades, multidisciplinary design methodologies have reached greater maturity, and are now capable of facing new technological challenges. The features offered by software optimization tools allow an effective exploration of a larger number of configurations within the design space which ensure also a reduction of the time with respect to the traditional approaches. The automatic management of design variables can therefore also be exploited to analyze the response of highly non-linear systems, while ensuring the simulation of a large number of design configurations.

Multidisciplinary and multi-objective optimization is now a promising method that can be used to manage increasing system complexity, to support product development, considering program objectives and constraints. Literature shows that there are not many published works on the multidisciplinary design of MFS. There are few recent papers related to the thermal design of such systems [22], [23], [24] and [25]. Those that consider multi-objective optimizations for the thermal aspects of multifunctional

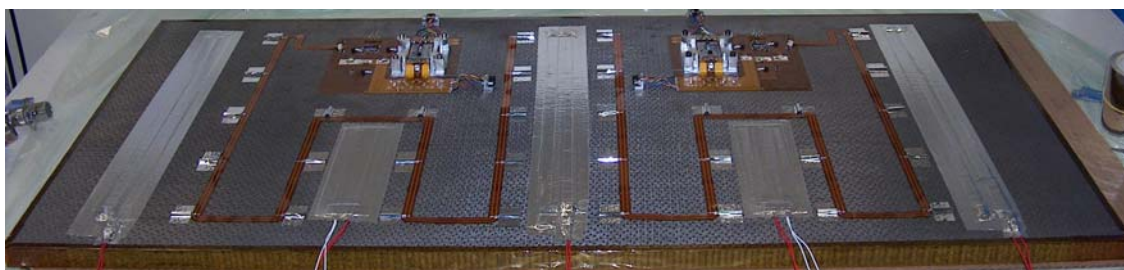


Figure 1 Advanced Bread Board.

structures are even rarer, and they focus in particular on fluidic heat transport [26] and [27] or on the optimization of the mechanical components of multifunctional structures [28], [29] and [30]. These are mainly studies on topology optimization of particular components [28], or studies on core architectures for sandwich structures [29].

Some of them also consider the thermal properties of the structural parts [28]. This paper is instead focused on the application of a model-based approach for the management of a multi-objective optimization for the selection of thermal hardware layout and control logic of spaceborne multifunctional structures. In particular the main objectives of the optimization are addressed towards the minimization of energy consumption and, to a lesser extent, to the achievement of a good temperature distribution. Moreover, the work includes a quantitative demonstration of the benefits that can be achieved with PID (proportional-integral-derivative) thermal control logic. Up to now, PID thermal control has only been proposed in a few specific cases with very sensitive payloads [31], [32] and [33] in order to satisfy demanding thermal requirements, and has never been optimized as a control law for a whole multifunctional assembly to save energy.

2 3D THERMAL MODELLING OF A STRUCTURE DEMONSTRATOR

The reference panel structure has been basically conceived for space applications and is made of two Carbon/Carbon skins separated by a Carbon/Carbon honeycomb core. The upper skin of ABB is equipped with two separate monitoring circuits. Each monitoring circuit is made of a bendable motherboard, a flat one-wire cable, a certain number of thermal sensors, and several electronic items. Each motherboard contains small heaters, piloted with a simple “on-off” technique, in order to ensure compliance with the operational range of the circuitry. Since these small heaters are not able to cover the whole thermal range applied during thermal vacuum tests, additional tape heaters have been embedded to the upper surface to manage its temperature distribution and protect the electronics. In an improved design, a sheet built with the same technologies used to manufacture the ABB motherboards, and which is able to cover all the structure, will form the outer smart layer of the multifunctional structure. This extended smart layer will avoid the addition of independent heaters, while enabling a proper distribution of embedded heaters and therefore enhancing thermal control and energy consumption of the multifunctional structure. The first part of this work concerns the definition of the thermal model relative to this particular case of multifunctional panel. In particular the overall system has been implemented through the support of a model-based infrastructure for the definition of its main features. Such system model allowed formalizing the characteristics used during this study, providing a common base for a consistent and shared representation of the equipment. Such information can

potentially be linked to different analyses models with the final aim to simulate the responses of the system for a specific domain.

In this case the analysis environment selected for the definition and link with the system model is Matlab-Simulink® (The MathWorks, Inc. 2008): this choice was motivated by the flexibility offered by the tool workspace and, in particular, by the possibility of an easy integration of different thermal control strategies. When setting up the thermal model, attention mainly focused on the determination of the energy consumption of the thermal control heaters, and of the thermal gradient on the panel. As far as the energy requirements for a particular heater arrangement and the operational requirements of the electronics are concerned, it is useful to understand which configuration allows the associated consumption to be reduced as much as possible. In fact, the resources available on board the space system are limited, and an appropriate thermal control design strategy should consider their savings. After the definition of the quantities of direct interest, it is possible to move on to the construction of the model. In the present study, a simple but flexible lumped parameter model has been considered, and the laws associated with the electrical analogy of thermal systems have been implemented. The three-dimensional model is essentially divided into 2 layers representing the upper and the lower skins of the multifunctional panel, respectively.

The model is made of 160 thermal nodes for the upper skin and an equal number for the lower skin. This value represents a proper balance between the representativeness of the thermal description for the real ABB panel and easiness of modeling. In addition, other nodes necessary for the definition of the boundary conditions have been included. These are needed to model the radiative heat transfer between the nodes of the lower skin and the surrounding environment (namely, the cold shrouds of a thermal vacuum chamber). The radiative heat transfer phenomenon with other elements has not been considered for the upper surface, as the presence of an MLI (Multi Layer Insulation) blanket and, therefore, of a negligible heat outflow involving such regions. Each node identifies a specific portion of the material. In the discretization scheme that has been adopted, part of the core material is assigned to the nodes of the upper skin and the other portion is instead assigned to the lower skin. The thermal resistance values between the individual nodes are evaluated from the real material properties, with reference to the values obtained experimentally during previous laboratory tests. The same procedure was adopted for the evaluation of the nodal thermal capacity. For the sake of clarity, the CAD geometry of the panel is represented in Figure 2, which also includes the layout of the main integrated electronic components and the nodes of the upper skin, in translucent grey, while the lower region ones are represented in black, consistently with the above mentioned description of the model. The quantities involved in the modeling activity have also been identified in the representation.

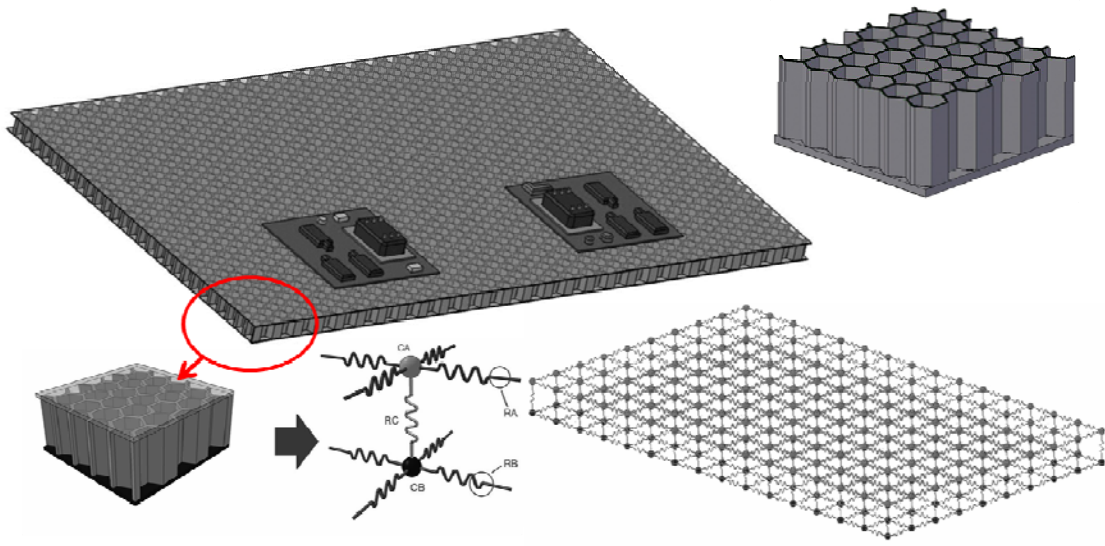


Figure 2 Advanced Bread Board modelling.

Figure 2 shows 3D-CAD representations of the lumped model, and highlight the implementation of the previous discretization on the whole system. Each of these thermal resistances is computed with the expression:

$$R_T = \frac{L}{\lambda \cdot S} \quad (1)$$

where L is the geometrical distance between the nodes characterized by heat exchange, λ is the thermal conductivity (under the assumption of material homogeneity along the conductive path), and S defines the transverse surface area for the heat flux. The calculation of the involved quantities refers to the three-dimensional representation always shown in Figure 2, which is a schematic visualization of one of the basic elements into which the structure is discretized.

The picture, in particular, schematically represents a portion of the real geometry of the structure, and, for convenience, the upper skin has not been visualized. In order to have an idea of the resolution of the model, the base of the depicted element represents a square surface portion of the panel with a 5 cm side. In the same figure, the cross-section, which is responsible for the passage of the heat flux in the transverse direction, is indicated with a black solid line: this section is associated with the definition of the thermal resistance along the core. The knowledge of the thermal resistance value between two nodes is used to define the power flow between these nodes, once the temperature difference is known.

$$q_T = \frac{1}{R_T} \cdot (T_i - T_j) \quad (2)$$

All the heat flows in the system have been calculated by implementing the same relationship in the Simulink® environment (by building a block diagram).

After the definition of the heat fluxes, a set of energy balance equations has been implemented: starting from the known heat fluxes, it is possible to define the time rate of the change in the nodal temperatures, which also depends on the associated heat capacity. As far as the heat capacity is concerned, the model refers to the following expression:

$$C_T = m \cdot c_{SP} \quad (3)$$

where m identifies the mass of the sub-volume, while c_{SP} identifies the specific heat that characterizes the material. Then, according to the heat capacity values associated with each node, it is possible to write the relation referring to the balance equations, which is given in the following expression:

$$\sum q = C_T \cdot \frac{\partial T}{\partial t} \quad (4)$$

The flux is positive when it flows into the node. Again, in a similar way to what is done for the definition of the flows, it is necessary to introduce a balance equation for each node in the system. In addition to the previous relations, the equations associated with the heat exchange through radiation, which are necessary for the characterization of the boundary flows, should also be considered:

$$q_{boundary} = \frac{1}{R_D} \cdot (T_i^4 - T_j^4) \quad (5)$$

where R_D identifies the thermal resistance for heat transfer through radiation, that is:

$$R_D = \frac{1}{A \cdot \sigma \cdot \varepsilon} \quad (6)$$

where A refers to the surface involved in the radiation exchange, σ identifies the Stefan-Boltzmann constant and ε is the emissivity.

The radiative view factors are considered equal to unity throughout the model. Since the Carbon/Carbon panel used as a thermo-mechanical substrate for ABB is a tailored product, physical properties were not readily available in literature. The demonstrator underwent specific thermal and mechanical tests to determine its characteristics.

The features of interest for thermal modeling purposes are the in-plane thermal conductivities ($k_x = 40$ W/mK; $k_y = 40$ W/mK), the through-the-thickness thermal conductivity ($k_z = 1.5$ W/mK), the density ($\rho = 1700$ Kg/m³), and the specific heat ($c_{sp} = 710$ J/KgK). The geometrical characteristics involved in the computation of the thermal parameters are the dimensions of the basic discretization element (side $l = 5$ cm; thickness $t = 2.1$ cm), the equivalent skin thickness accounting both for the real skin and for its associated portion of the core ($s = 5$ mm), the in-plane distance between the centroid of two adjacent elements ($L_p = 5$ cm), and the through-the-thickness distance between the centroid of two corresponding elements ($L_t = 2$ cm).

As for the present model, the thermal resistances associated with the structure of the panel are all of the same magnitude, although they can in principle be differentiated from each other when considering other structural configurations. For the same reason, the diffusive heat capacities associated with the nodes of the panel were all taken equal to each other, but they could be distinguished on the basis of the design requirements. The definition of the numerical characteristics of the in-plane resistances refers to the following values:

$$R_A = R_B = \frac{L}{k_x S} = \frac{L}{k_y S} \quad (7)$$

$$R_A = R_B = \frac{0.05}{40 \cdot 0.00025} = 5K/W$$

where the values for conduction path length L and flow section S perpendicular to the heat flux were estimated on the basis of the discretization adopted in the model. The following value has been estimated for the heat transfer along the core:

$$R_C = \frac{L}{k_z \cdot S} = \frac{0.02}{1.5 \cdot 0.00072} = 18.5K/W \quad (8)$$

In this case, the flow section and the length of the conductive path were also evaluated from the physical discretization. The values of the thermal capacities of the diffusive nodes have been computed according to the following relations:

$$C_A = C_B = V_A \cdot \rho_A \cdot c_{SP} \quad (9)$$

$$C_A = C_B = 0.05 \cdot 0.05 \cdot 0.005 \cdot 1700 \cdot 710 = 15.1 J/K$$

The estimated values can undergo changes, if the experimental results on a real panel are taken into account in order to offer greater validity to the model and simulations.

3 SYSTEM MODEL REPRESENTATION OF THE MULTIFUNCTIONAL PANEL

System modeling activities are currently moving from a document-centric perspective towards a Model-Driven Architecture (MDA) [6]. The functionalities offered by such an approach allow to better monitor and manage systems characterized by increasing complexity and involving a wide range of domains. In this context the MBSE initiative plays an important role in the formalization of processes, methods and tools used as support means for system engineering discipline [7]. A clear definition of these concepts is one of the leading elements that identify an effective model-based system from a not well designed one. MBSE emerging methodology provides the technologies used to design, analyze and verify the product structure and behavior [8]. In this case such an approach has been used to support the definition and formalization of the information available for the multifunctional panel. In this way it is potentially possible to manage large-scale system across all the life-cycle phases, combining the various needs and objectives coming from different engineering segments. In our case the system model has been linked with the thermal model developed within Matlab-Simulink[®] environment. The model-based paradigm followed in this study is basically built from the relationships between the concepts of process, method and tool [9]. A central system model can be used to store the main properties of the multifunctional structure, providing the basis for thermal analyses and simulations.

Such an MBSE methodology can be integrated with MDO techniques for rapid prototyping during the early phases of space system project (phases A/B). The integration of the functionalities offered by an MDO tool within an MBSE framework provides the basis for the proper management of the design variables from the early development phases to the more advanced ones. In this way it is possible to deeply explore the design space, reducing the possibility to neglect better solutions. MDO techniques can drive the decision-making process, relying on a well-defined framework where the design variables and other information are formalized and stored. In this context multidisciplinary analyses represent an instrument that helps to pilot design decision, highlighting where system responses may be enhanced. Introducing a partial automation for the exploration of system solutions it is possible to show some benefits, for example identifying new configurations and alternatives. Poor improvements in the design are often closely related to the industry mechanism of knowledge sharing as well as the lack of time. In an increasingly challenging field the choice is often directed towards conservative solutions. Configurations that require little changes are preferred with respect to design that are not previously identified or evaluated while MDO methods can help to consider new solutions and assess their performances.

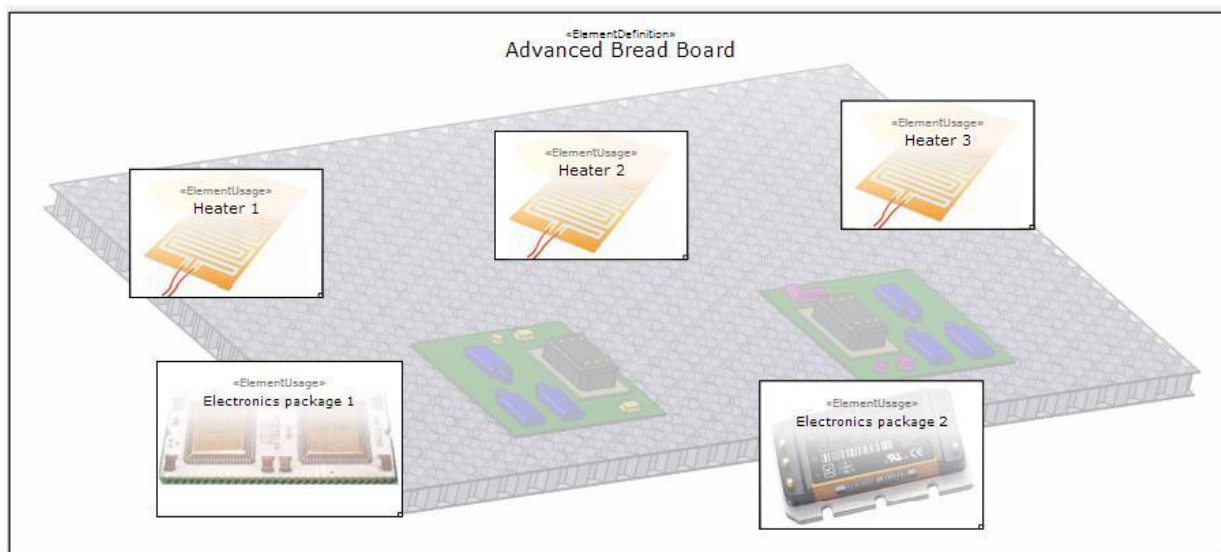


Figure 3 Architectural representation of the Advanced Bread Board represented.

A model-based framework has been used to describe the composition of the multifunctional panel, providing the definition of both its structural and behavioral model. Mission environment, system components and their behavior are modeled during this phase. The MDO methods, available from an external environment and linked with the modeling framework, can be used to manage some analyses once data are gathered in the same place.

System high level architecture is modeled following the model-based philosophy introduced in the first part of this study. In this phase the components properties and the relationships between equipment are defined within the same modeling environment. Once the project and a related baseline are created it is possible to gradually add other information regarding the functional as well as the topological architecture of the system. The first action performed regards the formalization and definition of available requirements with the possibility to after relate these ones with system components. Secondly the functional decomposition is supported within the same framework, ensuring a clear identification of space system functions. Space system topology is modeled starting from the definition of the architecture main characteristics and the parameters related to external environment features (e.g. introducing the information related to the operating conditions). Once the parameters under evaluation are clearly identified they are linked as design variables with the aim to handle their physical data with MDO strategies. These objects are mainly needed for the characterization of the boundary conditions that allow the proper setting the simulation models. Elements definition within the modeling framework allows linking the same object to different domain-specific simulation models. Each discipline can map a series of various simulation objects to the same unique component representation, depending on specific

needs. This step can be partially automated on the basis of detail level of the project. The simulation models such other properties related to the same object can then be used to set-up the analyses managed by an external MDO environment.

Lumped parameters model is used to compute the thermal behavior of the related element, employing Matlab environment as solver platform. Network models are used to compute the temperature and thermal flux values that characterize the linked element. Also the thermal control equipment, in this case strictly related to the electrical power subsystem, was coded with Matlab language.

In this sample scenario the thermal control equipment performs one of the needed functions for components survival. The simulation model is mapped to the same descriptive representation but it enhances the characteristics coming from different engineering domains. Environment properties (e.g. boundary conditions) are modeled in the same framework and used to set-up the various simulations, considering in particular the integration with an optimization framework. For example the heaters properties are included within the definition of components themselves and they have to be defined the first time the considered object is instantiated (basically following the philosophy of the object oriented methodology [10]). The main advantages related to such an approach are related to the fact that the information contained within these objects can then be used to evaluate the response in the simulation environment.

The modeling framework allows creating the schematic representation of components and connections of the contained objects from the definition of the single element to their behavior. Figure 3 shows an example of the high level ABB reference panel as modeled within a model-based environment. Components connections can be created, checked and monitored as the system design moves

towards more detailed phases. As information increase it is possible to perform some preliminary evaluation about the space system response with respect to the boundary conditions. Some design variables can be identified starting from the scenario definition.

They are basically represented by the thermal control elements configurations, their characteristics and positioning. In the following paragraphs a detailed description of the involved simulation models is not provided since the main objective of the current work is addressed towards the assessment of the integration between a modeling environment and a framework providing MDO strategies. Some of the parameters that are managed within the model-based workspace, exploiting the MDO functionalities provided by an external environment, are synthetically reported in the following lines (they mainly refer to the thermal control characteristics).

One of these design variables is related to the control logic rule, considering in this case two possible approaches (proportional and on-off).

Another design variable is the number of active heaters during the specific simulation run which is strictly related to the surface covered with such heating devices. The last design variable is represented by the maximum supplied power to each single heating element, limiting the power associated to the corresponding saturation. The simulation responses are instead focused on the variables reported in the following lines. One of such quantities is the overall energy consumption corresponding to a specific thermal control configuration.

The other output variable is a temperature uniformity index which has been introduced for comparison purposes on the temperature distribution over the panel surface. In this case

three objective functions are then been considered: the energy absorbed by the control devices, the temperature uniformity index over the panel (in-plane distribution, upper skin) and the number of active heating elements.

The constraints associated to this problem (defined on the basis of operational conditions) are the profiles of the operating electronics, the location of the electronic units, and compliance with the operational temperature ranges of the electronics. System performances evaluations are realized on the basis of the previously defined variables and constraints. These ones are directly linked with the requirements definition that has been introduced in the first part. In the reference case considered the structural requirements mainly concern the thermal loads and the evaluation of static and dynamic behavior on the structure.

The test case is based on the simulation of two computing blocks that solve specific analysis models. In particular the word “block” refers to the functional element that provides simulation capabilities. Their generation is driven by the information available at a particular design phase and they basically contain the analysis code that refers to a specific discipline (for our purpose we have considered the integration with Matlab environment but other external tools and framework can also be taken into account). These models can be linked to the corresponding objects stored in the descriptive system model once they have been implemented with the support of discipline-specific tools. Such connections allow to partially set-up different surveys and system analyses, leading to a more effective process of data exchange, exploiting all the advantages that can be provided by a MDO environment at the same time. The simulation models are linked with the system modeling environment as shown in Figure 4 where the functional

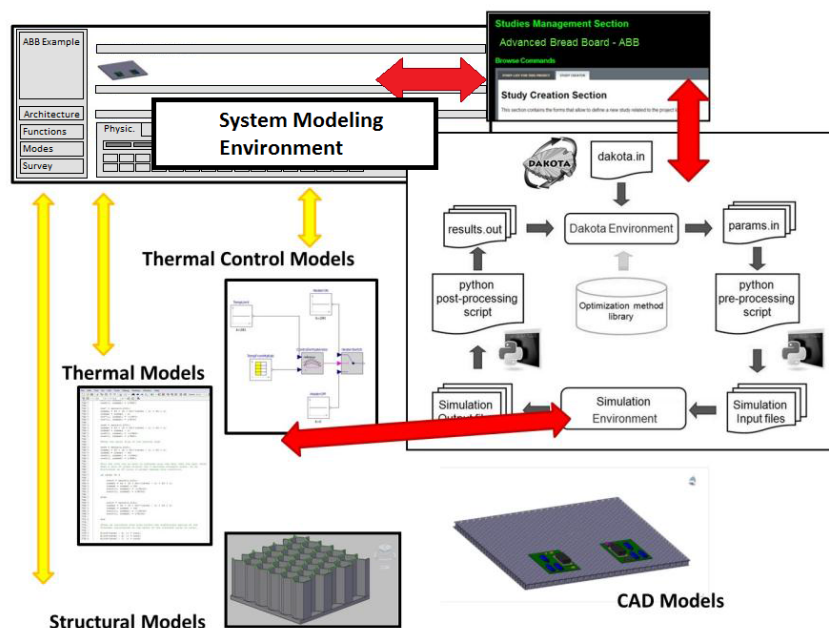


Figure 4 Overview of the functional relationships between simulation environment and prototype web-application.

connections with the web-based applications are summarized (the related pattern follows the current implementation of the MBSE modeling environment). Results are mapped with Python scripts to a MDO environment, allowing such an external framework to properly handle the simulation processes through the analyses themselves (trade-off, sensitivity analysis, optimization cycle, etc...). Figure 5 reports how the results related to different environments are mapped within the framework. After their construction and validation, the thermal and control models were in fact integrated in a software environment that was capable of managing optimization through an automatic manner: DAKOTA project [36]. Such software has been basically used as a process manager. It has no role in the physical modeling and in the simulation of the structure and its response (which is done, as already reported, in Matlab/Simulink®). DAKOTA takes care of executing series of analysis, while properly updating design variables according to an optimization algorithm. The evolutionary strategies used in the manuscript belong to a subset of alternative offered by the framework itself, and they drive the convergence process by evaluating the results of the Matlab® simulations and changing the model parameters accordingly. Before the beginning of the optimization process, it was necessary to obtain preliminary knowledge on the influence of different parameters on the overall MFS performance (energy consumption and temperature uniformity). Initially, after the integration of the thermal management model with the

design variables space, some Design of Experiments processes were conducted.

Results coming from the optimization cycles are represented briefly reported in Figures 6 and 7 to show what has been generated from the single algorithm run. What it is important to underline for the main scope of the current work is the fact that they are basically generated though the support provided by the information stored within the system model.

Figure 6 shows the results of three different non gradient-based algorithms used to solve the reference optimization problem. Each sub-figure reports the value of the maximum power related to the heating devices as the optimization cycle proceeds. In this case the parameters associated to the control thermal (energy consumed, thermal control law and heating elements location) are managed within the specific run on the basis of objective functions.

Figure 7 shows instead some of the plots that can be obtained from the available simulation results.

In particular they provide the main pattern of the Pareto front for the three algorithms under evaluation. In this case the charts report the Pareto front information about the temperature uniformity index and the number of active heaters. Red points refer to design solutions that do not satisfy the constraints while the blue ones represent the configurations corresponding to non-dominated solutions. The black points represent instead the design points that are compliant with the constraints but do not represent optimal solutions.

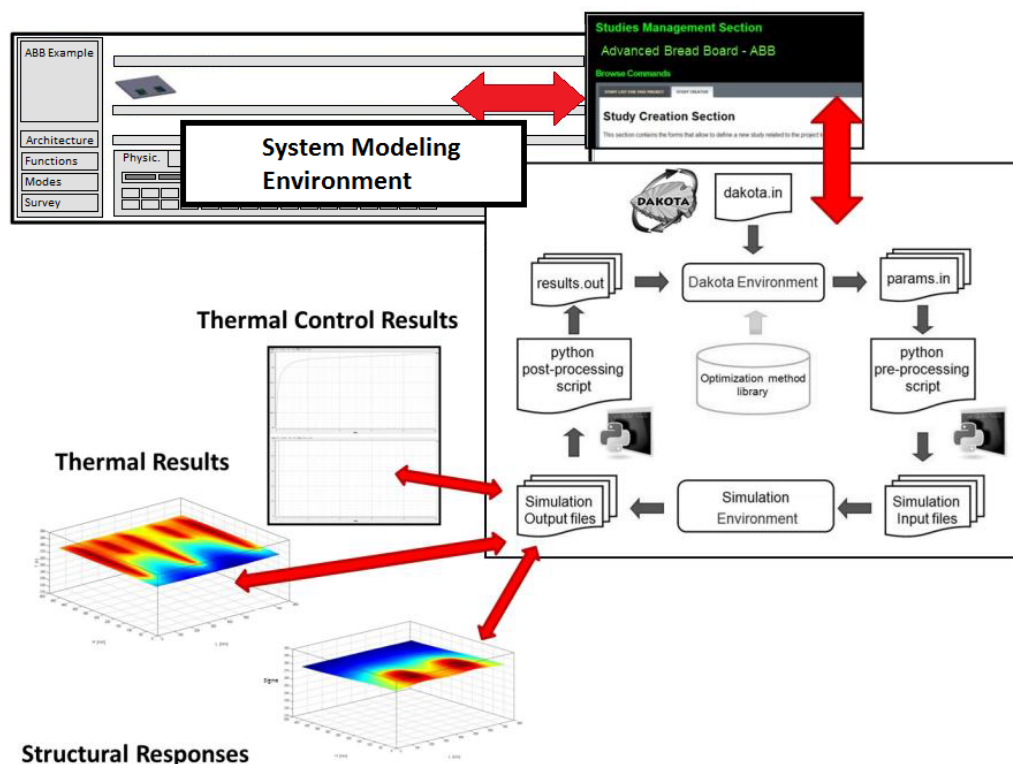


Figure 5 Overview of the data flows between the simulation environment and the MDO workspace.

4 LAYOUT OPTIMIZATION

It was possible to achieve a two-fold objective with the first optimization studies: to optimize the layout of the thermal control heaters in an improved ABB design, and to evaluate the different solution methods available in iSight. The design variables considered in this preliminary phase were the layout of the nodes considered to host control heaters, the maximum power supplied to the control elements (i.e., the power supplied by the control element under a saturation condition), and the type of control logic (ON=OFF or proportional). The solution algorithm was allowed to choose how many and which of the 160 potential control heaters would be activated. Moreover, the maximum power was allowed to range between a minimum value of 2 W and a maximum of 12 W. These limits reduce the calculation time, by restricting the analysis to values that are compatible with current technologies for space applications.

Two objective functions were considered: the energy absorbed by the control equipment, and the evaluation of the temperature uniformity along the panel (in-plane distribution, upper skin). The value of the involved energy was computed at the end of a fixed simulation time. The purpose of this objective was to minimize the overall value obtained from the simulations. The goal for the index representing the uniformity of temperature along the panel, which was evaluated in the final condition (even though it is potentially possible to consider its values at any time point during simulation), was once again minimization. The assessment of temperature uniformity was obtained by analyzing the thermal gradient along the panel. In particular, the figure of merit is the average modulus of the bi-dimensional temperature distribution gradient:

$$UnifTemp = \frac{1}{N_n} \sum_{i=1}^{N_n} \|\nabla T_i\| \quad (10)$$

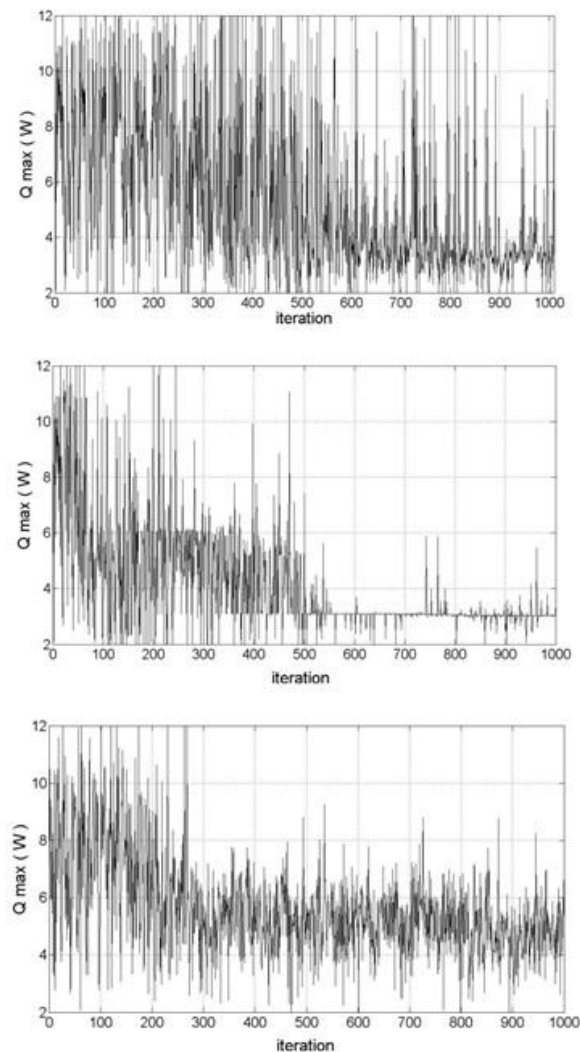


Figure 6 History data of the maximum power of heating elements as iterations proceed.

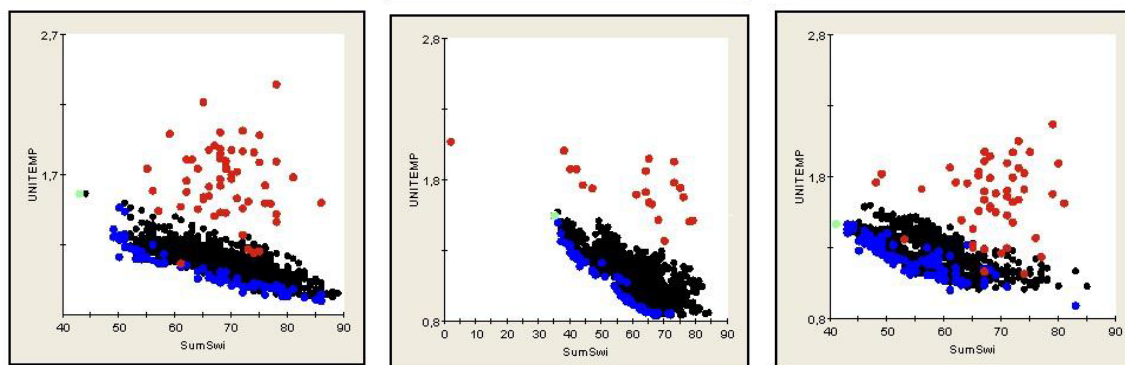


Figure 7 Pareto front plots corresponding to objective functions associated to the temperature uniformity index and total number of the heating elements.

In the multi-objective situation, considering the following weight factors: 0.6 for energy consumption, 0.2 for heaters number and 0.2 for uniformity temperature index, it was possible to give more emphasis to the minimization of energy consumption, rather than to the maximization of temperature uniformity. As far as the constraints introduced into the system, on the basis of the above considerations are concerned, the three adopted quantities were the profiles of the operating electronics, the positioning of the electronic units, and compliance with the operative temperature range for the electronics. The definition of the operating profile for the electronics is given through the time-history of the dissipations coming from the units onboard the two motherboards. These dissipations are arbitrarily chosen, and imposed on ABB via the regulation of the DC/DC converters feeding the two circuits. A proper power profile, dissipated on the two motherboards, made of piecewise linear functions with 50W of peak has been considered in this work. The position of the units of the electronic groups is considered fixed on the panel. Respect of the temperature requirements of the electronic units was also enforced: exiting from the operational temperature range was not allowed, even for a limited time interval. The maximum allowable temperature was 320 K and the minimum temperature was 270 K. Evaluation of violations of this constraint condition was made by estimating the *ConVio1* and *ConVio2* variables for the two zones covered by electronics (respectively, left and right motherboards). *ConVio1* and *ConVio2* are computed by summing up the absolute value of constraint violation for each time step during the simulation, i.e. by evaluating the violation $|\Delta T|$ (for a single time step and for all electronic nodes) and then summing up all $|\Delta T|$ during the simulation:

$$|\Delta T|_{time.step.i} = \begin{cases} T_{MIN} - T_{ele} & \text{if } T_{ele} < T_{MIN} \\ T_{ele} - T_{MAX} & \text{if } T_{ele} > T_{MAX} \end{cases} \quad (11)$$

$$ConVio = \sum_i |\Delta T|_{time.step.i}$$

where T_{MAX} and T_{MIN} are upper and lower operative temperature limits, and T_{ele} is the generic temperature T_i of node i belonging to one of the two electronic motherboards (subscript 1 or 2 has been omitted for ease of reading). In addition to the aforementioned constraints, the temperature of the boundary nodes that are interfaced with the bottom skin elements was set uniformly equal to 95 K and kept constant over time. This definition reflects the boundary conditions applied during laboratory tests in a thermal-vacuum chamber.

Six different optimization cycles were run with these variables, constraints and objectives, each of which was based on a different solution algorithm: Archive-Based Micro Genetic Algorithm (AMGA), Adaptive Simulated Annealing (ASA), Evolutionary Optimization Algorithm (Evol), Multi-Island Genetic Algorithm (Multi-Island GA), Neighborhood Cultivation Genetic Algorithm (NCGA), and Non-dominated Sorting Genetic Algorithm (NSGA-II). The research used an available set of optimization tools: the selected algorithms all belong to the evolutionary family, because this category is more suitable for non-linear functions problems in which the design space includes discontinuous variables. The time required by the six algorithms to resolve the problem was very similar (~17 hours, except for ASA, 19.5 hours, and Evol, 18 hours, on a Quad-Core, 3 GHz, 12 MB cache processor).

The real ABB panel hosts the equivalent of 38 active (heater) nodes, and their distribution is shown in Figure 8, while some of the different layouts obtained with the optimization studies are reported in Figure 9. In these figures, the dark grey squares represent the footprints of the motherboards, while the light grey squares indicate the presence of heaters. The numerical optimization results are summarized in Table I. The solution of the problem with six different optimization algorithms leads to six different optimal solutions. Therefore, for each one of the aforementioned optimization algorithms, Table I presents a description of search settings and results. The first column on the left specifies the names of the algorithms.

Then, a second column contains the main configuration parameters of the algorithms themselves (being evolutionary algorithms, their search behavior is dictated by these settings). Finally, the next four columns present the characteristics of the optimal solution found by each algorithm. Three columns out of five describe the value assigned automatically by the optimization algorithm to the free parameters: control logic (ON=OFF vs. proportional), number of active heaters (0÷142), and maximum power that can be dissipated on each single heater patch (2÷12 W). The last two columns on the right give the value of the objective functions for the optimal solution: total energy required to keep the structure inside the operative temperature range during the whole simulation, and temperature uniformity index. As a basis for comparison, the actual ABB configuration, with the ON=OFF control logic, requires 0.0576 kWh of energy and results in a temperature uniformity index equal to 2.02.

Summing up, the combined effect of an optimized heater layout and a proportional control logic leads to a saving in energy consumption of between 26.6% (Evol) and 39.6% (NCGA), and an improvement in temperature uniformity of 20.3% (ASA) to 39.6% (NSGA-II).

As mentioned before, the algorithms used for the optimization are evolutionary, as opposed to analytical, because they work well for problems with non-linear functions and discontinuous variables. The nature of the algorithms influences the heater distributions, which are scattered even if the ABB geometry is symmetric. Another reason of asymmetry is the difference in power dissipation between the right and left motherboards. The heaters' layouts are therefore irregular for the combined effect of the heuristic search which tries to reach the highest temperature uniformity while complying with the operative temperature ranges, and at the same time keeping into account the asymmetric and time-varying thermal loads.

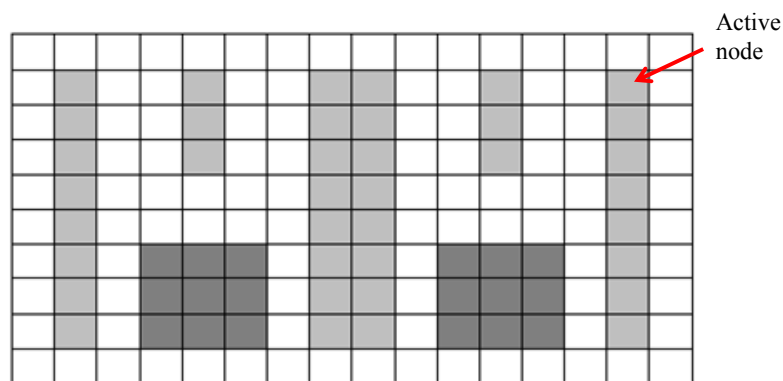


Figure 8 Original 38 active (heater) nodes of the ABB panel.

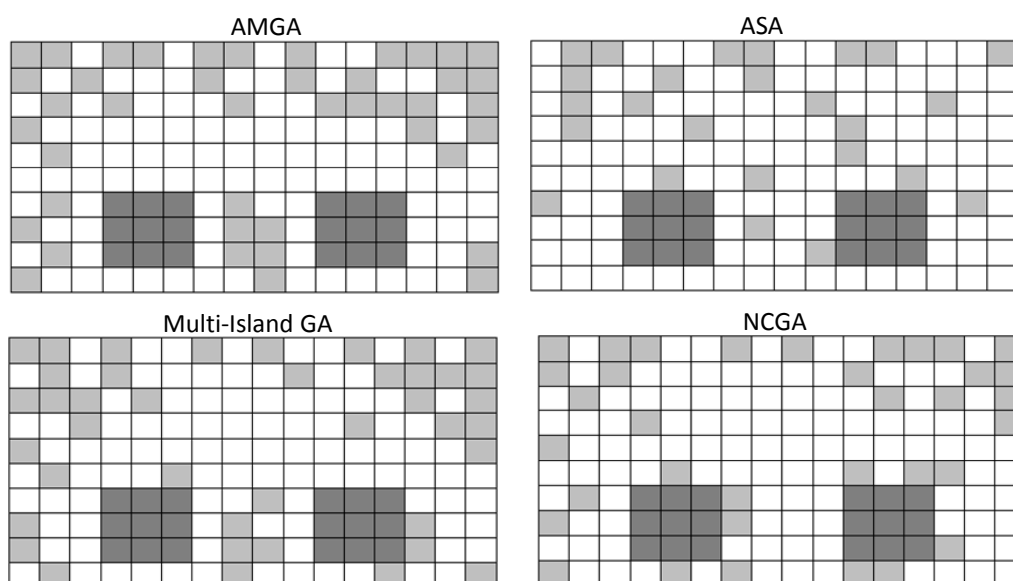


Figure 9 Optimized heaters layouts.

Furthermore, the results of the various algorithms are different one from the other both because every algorithm has its own search rules, and because the search path, even for the same algorithm, is partially casual.

Notably, a good outcome of this study is the fact that almost all the different algorithms identified the same areas that needed to be controlled via heaters (i.e. opposite corners of the top half of the panel and borders around electronic motherboards).

This fact both confirms the reliability of the computed solutions and offers a useful indication to select a finite number of layouts (as will be illustrated in more detail in the Section on “Comparison of the Control Strategies”).

Table I - Results of heater layout optimizations.

Name of Algorithm	Parameters and figures of merit of the optimum solution				
	Control logic	Active heaters	QH_{\max} (W)	Energy (kWh)	T Uniformity Index
AMGA	Prop.	43	5.733	0.0380	1.56
ASA	Prop.	25	11.32 9	0.0385	1.61
Evol	Prop.	48	9.163	0.0423	1.40
Multi-island GA	Prop.	41	8.369	0.0407	1.47
NCGA	Prop.	35	5.183	0.0348	1.55
NSGA-II	Prop.	37	5.980	0.0370	1.22

However, the geometrical arrangements of the heaters found thanks to the optimization are not readily implementable with standard thermal hardware; being too scattered, the heater patches would create a problem in terms of wire harness congestion. The benefits foreseen with such a layout have motivated further investigation and have given rise to a new concept for the smart thermal control layer of Multifunctional Structures, which would allow the exact heater distribution resulting from optimization to be reproduced. This new concept, with a distributed heater architecture, is currently under study in order to solve issues related to cable length, routing, and connection to the power distribution unit. The remainder of this study will only deal with layouts that could be implemented with already existing and proven hardware.

5 DESCRIPTION OF THE THERMAL CONTROL LOGICS

At the present time, but with a few exceptions, thermal control heaters on board satellites are piloted with an ON=OFF tactic. Even though this approach offers some undeniable advantages, in terms of simplicity and reliability, it is clearly not optimal for energy saving policies or for applications with strict temperature stability requirements.

Therefore, to encourage migration towards more energy efficient control strategies, the authors selected three additional logics and compared them in order to identify the benefits and drawbacks: although the ON=OFF logic was maintained, a proportional scheme, a PID (Proportional, Integral, Derivative) controller, and PTC (Positive Temperature Coefficient) heaters were added. The ON=OFF control is centered on a control temperature (T_{ctrl}) and has a sharp hysteresis loop (between $T_{ctrl} - 5$ K and $T_{ctrl} + 5$ K). The proportional rule is also quite simple: it is based on two reference temperatures, a limit one (T_{lim}) and a threshold one (T_{th}): when the node temperature is lower than the limit value, the heater is turned on at maximum power, on the other hand, when the node temperature is higher than the threshold value, the heater is turned off. Linear behavior, which decreases the dissipated power from QH_{\max} to 0, lies in-between. The PID controller is not described in detail here, since this control mechanism, which is based on a feedback loop, is well known and used extensively in many engineering fields. The controller is assumed in its ideal parallel form, in which the proportional, integral and derivative contributions have three different and independent coefficients:

$$u(t) = K_p e(t) + K_i \int_0^t e(\tau) d\tau + K_d \frac{d}{dt} e(t) \quad (12)$$

where $u(t)$ is the command signal, $e(t)$ is the error signal and K_p , K_i , and K_d are the tuning gains. The three multiplicative constants are the same for each heater on the panel. A fixed set point temperature (T_{sp}) is used to compute the error signal and is compared with the node temperature. A saturation law for $u(t)$ has also been added, in order to represent the physical limitation of the maximum power that can be dissipated on a single heater. PTC heaters are resistors that exhibit a slightly negative temperature-coefficient in the lower part of their temperature range, a sharp rise in resistance around the Curie point, and a negative coefficient again at higher temperatures. Their $R(T)$ curve is like a steep sigmoid and it is theoretically defined by four characteristic parameters: the *zero power resistance* at 25°C (the resistance value measured at 25 °C in such conditions that the change in resistance due to the internal generation of heat is negligible, $[R_{25}]=\Omega$), the *minimum resistance* (the minimum zero power resistance of the component, measured at the temperature in which the coefficient becomes positive, $[R_{min}]=\Omega$), the *switching temperature* (at which the resistance is twice the minimum resistance, $[T_b]=K$), and the *temperature coefficient of resistance* (the value of the slope of the resistance-temperature curve in the increasing resistance range, $[\alpha]=\%/K$).

$$\alpha = \frac{100}{(T - T_b)} \ln \left(\frac{R}{R_b} \right) \quad (13)$$

PTC components can be tailored to the user's needs and their $R(T)$ curve can be determined via experimental testing. To reduce the complexity of the problem, a fixed $R(T)$ curve, expressed as the interpolation of fixed data, has been assumed and T_b has been kept as a parameter (indicated as T_{rise}). In conclusion, a block model was built for each of the four aforementioned logics. The blocks are all gathered in the same subsystem, and the Simulink[®] model is able to switch between the possible controllers by operating a four-port switch.

6 COMPARISON OF THE CONTROL STRATEGIES

A certain number of possible heater configurations has been obtained from the first optimization study (see Section regarding "Layout Optimization: Variables, Objectives, Constraints and Comparison of Algorithms"). These layouts are obviously not immediately applicable as engineering solutions, since they are too granular. Therefore, two realistic arrangements have been taken from those scattered maps that include a total of 25 to 48 heaters: 29 active nodes were distributed in a compatible manner with commercially available rectangular Kapton or tape heaters. The two discrete layouts depicted in Figure 10 have been obtained as follows, keeping into account the results of the six different optimization runs. At first the different solutions were superimposed to each other, to identify those areas selected more often by the algorithms: see Figure 11, where white means no selection, pale grey means selected in just one layout, and black means selected in all six layouts. Then, inside these preferred areas identified by darker colors, the 29 active nodes were selected, keeping into account several aspects.

The first aspect was an effort to replicate the overall heaters distribution suggested by the algorithms, but using less active nodes. The second point was the fact that, having a significant reduction in the number of active patches, it was more appropriate to place them nearer to the electronic motherboards with respect to the solutions identified by the algorithms, because this would prevent an excessive number of temperature constraint violations (on the cold side) during the optimization runs. In the end it was also considered that the actual implementation would be performed by means of standard foil heaters (in tape or patch form), which would in turn require a pair of wires for each separate "heating island"; therefore, to minimize harness burden (number and routing of wires), the distribution should be as linear as possible, without odd shapes, cutouts, or too many small isolated patches.

The decision was therefore to lay a significant number of heaters in the top-right area, a smaller amount in the top-left area, and two frames around the motherboards. A degradation in panel isothermia is very likely to be introduced into the problem with this set up; however, these adjustments are necessary to obtain a viable design.

Once the distribution of the active nodes has been fixed on the upper sandwich skin (as shown in Figure 10), an optimization activity for the adjustment of the parameters of the thermal control laws was started. The definition of the problem is reported in Table II. The problem has been solved with an NCGA algorithm, based on a population size equal to 10, a number of generations equal to 20, single point crossover with a crossover rate equal to 1.0, and a mutation rate equal to 0.01.

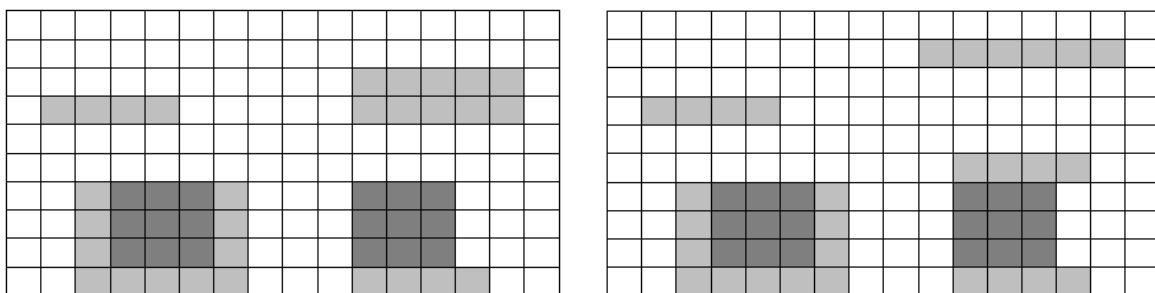


Figure 10 Two discrete layouts obtained keeping into account the results of the six different optimization runs.

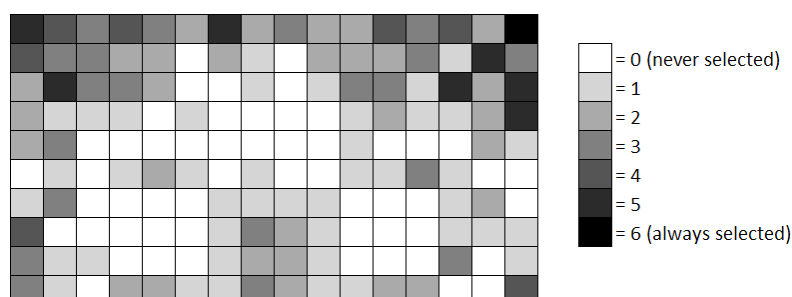


Figure 11 Superimposition of the different layouts (White = never selected; Black = always selected).

The optimization process identified an optimal solution, characterized by a PID control law with $T_{sp} = 275$ K, applied to heater layout number 2. The maximum power for each heater is 4.08 W. The energy consumption with this configuration is about 0.0303 kWh, while the temperature uniformity index is 2.21. A reduction of ~ 1 W on the smallest allocated QH_{max} and a total energy saving ranging from 4.5 to 12 Wh were obtained with respect to the solutions in the Section on “Layout Optimization: Variables, Objectives, Constraints and Comparison of Algorithms”. On the other hand, a relevant increase in the temperature uniformity index was measured, reflecting a worse solution from the isothermality point of view. However, this is mainly due to the correction that has been applied to the heater layout in order to make it feasible from the engineering point of view.

Table II - Optimization of the thermal control law.

Variables			
Name	Min. value	Max. value	Description
CONTRACT	1	4	Control law selector. Can only assume integer values (#).
HTRLAYO UT	1	2	Heater layout selector. Can only assume integer values (#).
QHMAX	2	12	Maximum power allowable for one heater. Real value (W).
TEMINIS	265	275	ON+OFF law center temperature. Real value (K).
TLIM	250	270	Proportional law limit temperature. Real value (K).
TTH	270	290	Proportional law threshold temperature. Real value (K).
TSP	275	280	PID controller reference temperature. Real value (K).
TRISE	275	280	PTC heater switching temperature. Real value (K).
Constraints			
Name	Bounds	Description	
CONVIO1	<0	If positive, quantifies the extent of temperature range violation for electronics on the left side.	
CONVIO2	<0	If positive, quantifies the extent of temperature range violation for electronics on the right side.	
Objectives			
Name	Direction	Description	
ENE	minimize	Energy required to feed the heaters during the whole simulation. Measured in kWh.	
UNIFTE MP	minimize	Index for in-plane temperature evenness. Dimensionless quantity.	

The optimum points reported in Section “Layout Optimization: Variables, Objectives, Constraints and Comparison of Algorithms” were obtained using a proportional logic, while the best solution identified in this Section refers to a PID controller whose coefficients have been determined with the Ziegler-Nichols method ($K_p=8.4$, $K_i=67.2$, $K_d=0.1$). Table III shows a numerical comparison. The columns labeled as “Proportional” summarize the results of the old optimum point, i.e. the optimal solution of the study presented in Section “Layout Optimization: Variables, Objectives, Constraints and Comparison of Algorithms”. The first row contains data generated by the NCGA algorithm, while the second row refers to the “Evol” algorithm. The columns labeled as “PID” report the results of the new optimum point obtained in this Section. The columns labeled as “Comparison” present the variations between the old and new values, both in absolute (on the left) and percentage (on the right) terms. With respect to the figures in the actual ABB design mentioned in Section “Layout Optimization: Variables, Objectives, Constraints and Comparison of Algorithms”, the new optimal solution characterized by layout n.2 and a PID control offers a 47% reduction in energy consumption, while the increase in the temperature uniformity index is now a small 9%.

The best feasible points identified with the optimization study are all based on the PID logic, therefore these cases were isolated and the influence of the T_{sp} value on the global MFS performance was explored. It is clear that a positive correlation of this parameter exists both for the total energy consumption and for the unevenness of the in-plane temperature distribution (see Figure 12). The two clearly distinct sets that can be observed in Figure 12 b) are due to the two different layouts. In these pictures, black dots represent feasible solutions, while grey dots are feasible solutions which maximize one of the objective functions. The only white dot is the overall optimal solution. Regarding Figure 12 a), the horizontal axis shows the set point temperature (measured in Kelvin), while the vertical axis shows the total energy consumption (measured in kWh). As concerns Figure 12 b), the horizontal axis shows the set point temperature (measured in Kelvin), while the vertical axis shows the temperature uniformity index (dimensionless quantity). The results obtained confirm that, if it is not possible to embed a predictive “description” of the system to be controlled in the controller, a PID logic is surely a good choice. Like many other feedback logics, it will solely rely on a “reactive” mechanism, but the performance will be much better. Unfortunately, PID strategies are best employed in *linear symmetric* problems, in which the variable to be controlled can be corrected both with positive and negative commands: in this case, since there is no active cooling piloted by the PID, is it only possible to affect the variables with positive commands (increasing temperature), while

overshoots can only be minimized with an over-damped configuration, but cannot be actively corrected. Nonetheless, it is interesting to investigate the possibility obtaining further benefits from the PID controller through a better tuning of its parameters: this is the content of the next section.

7 PID CONTROLLER OPTIMIZATION

After the encouraging results shown in the previous section, focus was concentrated on the best configuration in an attempt to obtain further improvements. To this aim, another optimization study, which is summarized in Table IV, was performed. This time only the Proportional-Integral-Derivative logic was adopted, and its six parameters (the heater layout, the maximum power fed to one heater, the PID set point temperature and the three PID constants) were left free for possible changes.

The problem has been solved with a Neighborhood Cultivation Genetic Algorithm (NCGA), based on a population size of 20, a number of generations equal to 50, single point crossover with a crossover rate equal to 1.0, and a mutation rate equal to 0.01. The NCGA run lasted 17.27 hours and produced 959 feasible designs from over 1001 evaluations. The genetic algorithm identified a Pareto set of solutions. The solution characterized by the values reported in Table V was selected according to the authors' discretion, giving mostly preference to one of the objectives, the minimization of energy, but also seeking a less penalizing solution under the temperature uniformity point of view. After discarding all the unfeasible solutions (those with a violation of constraints), the remaining options have been ordered by increasing energy consumption and then by decreasing temperature uniformity index.

The best results in terms of energy were obviously not the best in terms of isothermia, and a decision was taken to

allow a penalization at the third decimal place in the energy consumption figure (+1.25%) in change for an improvement of the first decimal place in the temperature uniformity figure (-4.44%).

Therefore the choice was given to the solution listed in Table V, which is the first option in ranking order allowing the aforementioned tradeoff with positive effect on the temperature uniformity index. Its energy consumption was 0.0278 kWh, while the temperature evenness index was 2.16. This result, in comparison with the PID solution in Section "Comparison of the Control Strategies", reduces the energy consumption by another 8%, while the enhancement of the isothermal condition of the panel is only about 2%. The small improvement obtained, in terms of temperature uniformity, confirms that this figure of merit mainly depends on the heater distribution, rather than on the thermal control law. Table V summarizes the benefits obtained with the optimization of the PID parameters.

Table III - Comparison of the optimal solutions.

Total energy (kWh)		Temperature uniformity (#)					
Prop.	PID	Comparison		Prop.	PID	Comparison	
		Abs.	%			Abs.	%
NCGA: 0.0348	0.0303	-0.0045	-12.93	NCGA : 1.55	2.21	+0.66	+42.58
Evol: 0.0423		-0.0120	-28.37	Evol: 1.40		+0.81	+57.86

The columns labeled "Previous optimum" summarize the results of the old optimum points, i.e. the optimal solutions presented in Sections "Layout Optimization: Variables, Objectives, Constraints and Comparison of Algorithms" and "Comparison of the Control Strategies".

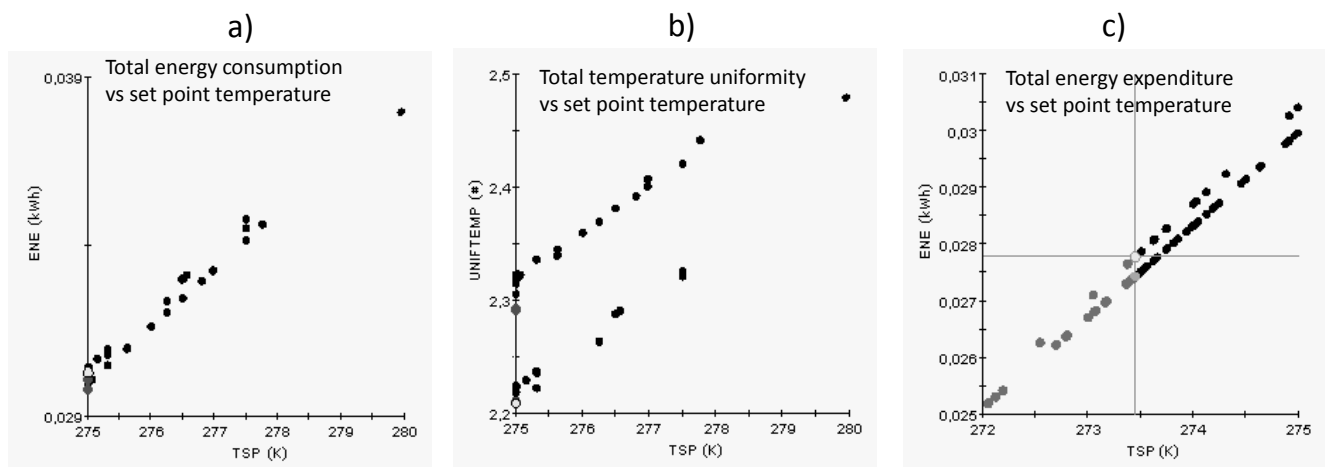


Figure 12 Energy consumption and temperature uniformity during the optimization runs.

The first row contains data generated by the NCGA algorithm in Section “Layout Optimization: Variables, Objectives, Constraints and Comparison of Algorithms” (listed as Opt. 1 for brevity); the second row refers to the “Evol” algorithm in the same Section “Layout Optimization: Variables, Objectives, Constraints and Comparison of Algorithms”; the third row includes the solution obtained in Section “Comparison of the Control Strategies” (listed as Opt. 2 for brevity). The columns labeled “New optimum” report the results of the new optimum point obtained in this Section via NCGA. The columns labeled “Comparison” present the variations between the previous and new optima, both in absolute (on the left) and percentage (on the right) terms. In comparison with ABB, the new design allows a 52% reduction in energy consumption, and limits the increase in temperature uniformity index to 7%. From the energy saving point of view, it could be possible to obtain some further small improvements (about one percentage point, that is < 1 W) by selecting heater layout number 1, but at the same time this choice would deteriorate the UNIFTEMP index. Since the enhancement of the energy budget would be minimal, it would be better to choose the solution that allows a smoother temperature distribution on the upper skin. The presence of a feasible solution with lower energy expenditure can be noticed in Figure 12 c). In this picture, the light grey dot is a feasible solution which minimizes the temperature uniformity index. Black dots (upper right quadrant) are feasible solutions, while dark grey dots (bottom left quadrant) are unfeasible solutions (with non-zero constraint violation). The only white dot is the overall optimal solution, and grey lines are just visual aids to locate the optimum and read the value of its parameters on the two axes. The horizontal axis shows the set point temperature, measured in Kelvin, while the vertical axis shows the total energy consumption, measured in kWh. To obtain a preliminary perception of how much the evolutionary search algorithm can influence the localization of the solution, a second genetic algorithm based optimization was carried out with AMGA (Archive-based Micro Genetic Algorithm) with an initial size of 80, a population size of 80, a number of function evaluations equal to 1000, a crossover probability equal to 0.9, and a mutation probability equal to 0.5. The computation lasted 17.18 hours. This second search identified an optimal solution that is very similar to the previous one: a maximum required energy of 0.0277 kWh, and a temperature uniformity index of 2.16. Therefore, the advantages obtained compared to an ON-OFF or proportional rule are almost identical to those shown in Table VI. This fact confirms the reliability of the previously identified optimum point. The PID parameters of this solution are summarized in Table VII. As a final check, the stability of the best control law was verified via a dedicated simulation. The results confirm that the temperature behavior is free of undesired oscillations.

In order to assess the robustness of the improvement obtained with the PID logic, white noise was injected upstream from the controller input in a dedicated dynamical model of the panel. This noise would roughly simulate a general EMI/EMC problem that affects, for example, the sensors.

As a result, the system response obviously shown some oscillations in the regulated temperatures (of the order of $1 \div 2$ K), but the overall energy consumption did not change: only small negligible fluctuations were registered with a noise power - i.e. height of the noise PSD - of 0.01 or 0.1.

Table IV - Optimization based on variations of the PID parameters: problem statement.

Variables			
Name	Min. value	Max. value	Description
HTRLAYOUT	1	2	Heater layout selector. Can only assume integer values (#).
QHMAX	5	7	Maximum power allowable for one heater. Real value (W).
TSP	272	275	PID controller reference temperature. Real value (K).
KPPID	-8.4	-6	PID controller proportional gain. Real value ($W K^{-1}$).
KIPID	-67	-47	PID controller integral gain. Real value ($W K^{-1} s^{-1}$).
KDPID	-0.08	-0.03	PID controller derivative gain. Real value ($W s K^{-1}$).
Constraints			
Name	Bounds	Description	
CONVI01	<0	If positive, quantifies the extent of the temperature range violation for the electronics on the left side.	
CONVI02	<0	If positive, quantifies the extent of the temperature range violation for the electronics on the right side.	
Objectives			
Name	Direction	Description	
ENE	minimize	Energy required to feed the heaters during the whole simulation. Measured in kWh.	
UNIFTEMP	minimize	Index for in-plane temperature evenness. Dimensionless quantity.	

Table V - PID controller parameters in the NCGA optimum solution.

HTRLAY OUT	QH _{MAX} (W)	TSP (K)	KPPID (W K ⁻¹)	KIPID (W K ⁻¹ s ⁻¹)	KDPID (W s K ⁻¹)
2	5.82	273.45	-6.72	-47.07	-0.06

Table VI - Comparison of the new optimum solution with previous optimal results.

Total energy (kWh)				Temperature uniformity (#)			
Previous optimum	New opt.	Comparison		Previous optimum	New opt.	Comparison	
		Absol.	%			Absol.	%
NCGA Prop. (Opt. 1) 0.0348	0.0278	-0.0070	-20.12	NCGA Prop. (Opt. 1) 1.55	2.16	+0.61	+39.36
Evol Prop. (Opt. 1) 0.0423		-0.0145	-34.28	Evol Prop. (Opt. 1) 1.40		+0.76	+54.29
NCGA PID (Opt. 2) 0.0303		-0.0025	-8.28	NCGA PID (Opt. 2) 2.21		-0.05	-2.26

Table VII - PID controller parameters in the AMGA optimum solution.

HTRLA YOUT	QH _{MAX} (W)	TSP (K)	KPPID (W K ⁻¹)	KIPID (W K ⁻¹ s ⁻¹)	KDPID (W s K ⁻¹)
2	5.19	273.42	-6.34	-61.36	-0.05

CONCLUSIONS

A light, reliable thermal model based on electrical analogy for a multifunctional structure prototype has been created and validated. The parametric model also comprises the description of four different control laws for heater activation: ON=OFF logic, a proportional scheme, a proportional-integral-derivative controller, and positive temperature coefficient heaters. This model has been used to perform multiple runs, with parameters that were determined via Design of Experiments and multi-objective optimization algorithms, in order to enhance the design of the multifunctional structure prototype.

The optimization problems had the objective of establishing the best heater layout, the best control law and its parameters, and of evaluating the performance of the system in terms of total energy consumption and in-plane temperature uniformity.

The study has been able to suggest heater layouts which are more efficient than those obtained with conventional designs: energy consumption can be reduced by a percentage ranging from 26.6% to 39.6%, and temperature uniformity can be improved by 20.3% to 39.6%.

The results also highlighted that limitations in heater layout flexibility have a great effect on the ability of the Thermal Control System to maintain a fine regulation of the temperature distribution. It is clear that the granularity of the heating patches allowed in the genetic optimization can lead to a better control of the in-plane temperature distribution. However, the solutions offered by the algorithms are difficult to put into practice with standard (commercially available) thermal hardware, and the technology needed for a simple and straightforward implementation of the exact optimal layout is still under development. Therefore, a finite number of engineering viable layouts were chosen from the optimization outcomes, and subsequently used for the rest of the study. These simplified outlines introduce an acceptable degradation of panel isothermia, but allow easy manufacturing with a reduction of 17 ÷ 38 % of the total heater area. This result clearly shows the advantage that can be obtained with a systematic optimization of the thermal control design. Furthermore, multi-objective optimization techniques have been used, in a quantitative study, to substantiate the convenience of upgrading the thermal control strategy from a simple ON=OFF logic to a more complex one. In particular, the work has been successful in quantifying the performance improvement that can be obtained with a proportional or proportional-integral-derivative law. Moreover, the analysis has shown the advantages of an optimized proportional-integral-derivative controller. The energy savings, for the case under study, can reach 34 % compared to a proportional law, and settle around 52 % if compared with the ON=OFF strategy. These benefits justify the drawback in terms of design complexity, and suggest that, as a general rule, a remarkable improvement of the design can be obtained at the cost of just few hours of computational time (less than 24 hours on a Quad-Core, 3 GHz, 12 MB cache processor). At the end of the process, the multi-objective optimization was able to produce an alternative design that halved the energy consumption and maintained an acceptable temperature distribution with a reduction of 24 % in the required thermal hardware (heater area).

ACKNOWLEDGMENTS

The study presented in this paper, which was carried out at Politecnico di Torino, is based on a demonstrator breadboard that was designed and built by Thales Alenia Space - Italia. The Authors wish to thank the DESI Thermal Systems group of Thales Alenia Space - Italy for the disclosure of the ABB technical data and of the technologies developed in the framework of the ROV-E EC FP-7 Project.

REFERENCES

- [1] Spangelo S. C., et al., Applying Model Based Systems Engineering (MBSE) to a Standard CubeSat, *IEEE Aerospace Conference*, 2012.
- [2] Bajaj M., Zwener D., Peak R., Phung A., et al., SLIM: collaborative Model-Based Systems Engineering Workspace for Next-Generation Complex Systems, *IEEEAC Paper #1404*.
- [3] Robinson T. D., Eldred M. S., Willcox K. E., and Haines R., Surrogate-Based Optimization Using Multifidelity Models with Variable Parameterization and Corrected Space Mapping, *AIAA Journal*, Vol. 46, No. 11, pp. 2814-2822, 2008.
- [4] Markish J., and Willcox K., Value-Based Multidisciplinary Techniques for Commercial Aircraft System Design, *AIAA Journal*, Vol. 41, No. 10, pp. 2004-2012, 2003.
- [5] Willcox K., and Wakayama S., Simultaneous Optimization of a Multiple-Aircraft Family, *Journal of Aircraft*, Vol.40, No. 4, pp. 616-622, 2003.
- [6] Gasevic D., Djuric D., Devedzic V., *Model Driven Engineering and Ontology Development*, 2nd ed., Springer-Verlag, 2009.
- [7] Estefan J. A., Survey of Model-Based Systems Engineering (MBSE) Methodologies, *INCOSE MBSE Focus Group*, 2008.
- [8] Fuchs J., Multi-disciplinary MBSE Approach in Industrial Phases, *Infotech@Aerospace 2012*, AIAA, pp. 2012-2532, 2012.
- [9] Martin J. M., *Systems engineering guidebook: a process for developing systems and products*, CRC Press, 1997.
- [10] Friedenthal S., Object Oriented Systems Engineering, Process Integration for 2000 and Beyond, *Systems Engineering and Software Symposium*, New Orleans, LA, Lockheed Martin Corporation, 1998.
- [11] Chona R., Aerospace Structures for the 21st Century An Air Force Perspective on Research Needs, *Proc., 46th AIAA/ASME/ASCE/AHS/ASC SDM Conference*, Austin, TX, 2005.
- [12] Gibson, R. F. (). "A review of recent research on mechanics of multifunctional composite materials and structures, *Composite Structures*, Vol. 92, pp. 2793-2810, 2010, doi:10.1016/j.compstruct.2010.05.003.
- [13] Jang S. T., Oh D. S., Kim J. K., Kang K. I., Cha W. H., Rhee S. W., Development of multi-functional composite structures with embedded electronics for space application, *Acta Astronautica*, Vol. 68, Issues 1-2, pp. 240-252, 2011.
- [14] Piascik B., Vickers J., Lowry, D., Scotti S., Stewart J., Calomino A., Materials, Structures, *Mechanical Systems, and Manufacturing Roadmap*, National Aeronautics and Space Administration (NASA) Technology Area 12 Roadmap, 2010.
- [15] Roberts S. C., Aglietti G. S., Structural performance of a multifunctional spacecraft structure based on plastic lithium-ion batteries, *Acta Astronautica*, Vol. 67, pp. 424-439, 2010. doi:10.1016/j.actaastro.2010.03.004
- [16] Schwingshack C. W., Aglietti G. S., Cunningham P. R., Parameter Optimization of the Dynamic Behavior of Inhomogeneous Multifunctional Power Structures, *AIAA Journal*, Vol. 44, No. 10, pp. 424-439, 2006, doi:10.2514/1.18599.
- [17] Schatzel D.V., Multi-Functional Spacecraft Structures Integrating Electrical and Mechanical Functions, *Proc., IEEE Aerospace Conference*, Big Sky, MT, pp. 1-6, 2007, doi: 10.1109/AERO.2007.352644.
- [18] Gottero M., Sacchi E., Zeminiani E., Development of Multifunctional Structures at Thales Alenia Space – Italia, *Proc., NATO RTO AVT-171 Workshop*, Antalya, Turkey, paper n. 17, 2010.
- [19] Branke J., Deb K., Miettinen K., Roman Slowinski R., *Multiobjective Optimization – Interactive and Evolutionary Approaches*, Springer-Verlag, 2008, ISBN-10: 3-540-88907-8.
- [20] Collette Y., Siarry P., *Multiobjective Optimization – Principles and Case Studies*, 1st ed., Springer-Verlag 2003, ISBN-10: 3-540-40182-2.
- [21] De Weck O., Willcox K., *MIT MSDO Lecture Notes*, Massachusetts Institute of Technology OpenCourseWare, 2010 <http://ocw.mit.edu/courses/engineering-systems-division/esd-77-multidisciplinary-system-design-optimization-spring-2010/index.htm>
- [22] Zhang, S., Cao, X., Luan, Y., Ma, X., Lin, X., Kong, X. (2011). "Preparation and Properties of Smart Thermal Control and Radiation Protection Materials for Multi-functional Structure of Small Spacecraft." *Journal of Materials Science & Technology*, Vol. 27, Issue 10, October 2011, pp. 879-884.
- [23] Foster J.A., Aglietti G.S., The thermal environment encountered in space by a multifunctional solar array, *Aerospace Science and Technology*, Vol. 14, pp. 213-219, 2010, doi:10.1016/j.ast.2009.12.008.
- [24] Queheillalt D. T., Carbajal G., Peterson G.P., Wadley H. N. G., A multifunctional heat pipe sandwich panel structure, *International Journal of Heat and Mass Transfer*, Vol. 51, pp. 312-326, 2007, doi:10.1016/j.ijheatmasstransfer.2007.03.051
- [25] Rawal S. P., Barnett D. M., Martin D. E., Thermal Management for Multifunctional Structures, *IEEE Transactions on Advanced Packaging*, Vol. 22, No. 3, pp. 379-383, 1999, doi: 10.1109/6040.784489
- [26] Williams, A. D., Underwood, R. L., Arritt, B. J. (2010). "Biologically Inspired Multifunctional Composite Panel with Integrated Thermal Control." *Proc., 51st AIAA/ASME/ASCE/AHS/ASC*

- Structures, Structural Dynamics, and Materials Conference, Orlando, FL.
- [27] Roper C. S., Multiobjective optimization for design of multifunctional sandwich panel heat pipes with micro-architected truss cores, *International Journal of Heat and Fluid Flow*, Vol. 32, pp. 239-248, 2010, doi:10.1016/j.ijheatfluidflow.2010.07.002
- [28] Challis V.J., Roberts A.P., Wilkins A.H., Design of three dimensional isotropic microstructures for maximized stiffness and conductivity, *International Journal of Solids and Structures*, Vol. 45, 2008, pp. 4130-4146, 2008.
- [29] Tan X.H., Soh A.K., Multi-objective optimization of the sandwich panels with prismatic cores using genetic algorithms, *International Journal of Solids and Structures*, Vol. 44, 2007, pp. 5466-5480, 2007.
- [30] Valdevit L., Jacobsen A.J., Greer J.R., Carter W.B., Protocols for the Optimal Design of Multi-Functional Cellular Structures: From Hypersonics to Micro-Architected Materials, *Journal of The American Ceramic Society*, Vol. 94, Issue Supplement s1, pp. s15 - s34, 2011, doi: 10.1111/j.1551-2916.2011.04599.x.
- [31] Pan C., Youshan Q., Huijuan L., Jiahai T., Design and Implementation of Cooling System for Focal Plane Assembly of Observation Camera in Astronomical Satellite, Proc., *1st IEEE International Conference on Electronics, Communications and Control (ICECC)*, Ningbo, China, 2011.
- [32] Leroy C., Maisonneuve M., Piat M., Trouilhet J.F., Pearson D., Camier C., Guibert S., Simulation of the Planck-HFI thermal control system, Proc., *SPIE (International Society for Optics and Photonics)*, Marseille, France, Vol. 7017, pp. 701713-1 - 701713-8, 2008.
- [33] Valentini D., Vacance M., Battaglia D., Pieper B., Niot J.M., GOCE Instrument Thermal Control, Proc., *36th International Conference on Environmental Systems*, Norfolk, VA, SAE Technical Paper 2006-01-20442006, 2006, doi:10.4271/2006-01-2044
- [34] The MathWorks, Inc., *Matlab®/Simulink® Software Package*, Ver. 7.7.0.471 (R2008b), (CD-ROM) Natick, MA, 2008.
- [35] Dassault Systèmes Simulia Corp, *iSight Software Package*, Ver. 4.5-1." (CD-ROM), Cary, NC, 2010.
- [36] Adams B.M., Bohnhoff W.J., Dalbey K.R., Eddy J.P., Eldred M.S., Gay D.M., Haskell K., Hough P.D., Swiler L.P., *DAKOTA, A Multilevel Parallel Object-Oriented Framework for Design Optimization, Parameter Estimation, Uncertainty Quantification, and Sensitivity Analysis: Version 5.0 User's Manual*, Sandia Technical Report SAND2010-2183, December 2009.
- [37] Zeminiani E., Cencetti M., Maggiore P., Multi-objective Optimization of Thermal Control Strategies for Multifunctional Structures, *Journal of Aerospace Engineering*, vol. 27, 2014, ISSN 0893-1321.

THE MECHANISM OF CRACK INITIATION AND PROPAGATION IN METALLIC ENGINEERING MATERIALS

Hoang Van Thang

City University London, U.K.

ABSTRACT

This paper investigates crack initiation and crack propagation in metallic engineering materials. The role of metal structure, temperature and surrounding environmental conditions and loading conditions on the crack initiation and propagation of metals will be reviewed. The purpose of this article is to have full understanding of crack mechanism in metals in order to have solutions for preventing it.

Keywords: metallic material crack; crack initiation; crack propagation

1 INTRODUCTION

Crack in metals is a significant concern in every sector of engineering. Every year human and material losses have come from failures in engineering that result from the formation and propagation of the crack in metals. As a result it is important to know about crack initiation and crack propagation in metallic engineering materials to find the solutions for preventing it.

2 DEFINITION OF METALLIC MATERIALS

In nature, all metallic materials are crystalline structures in which atoms are arranged in some regular geometrical pattern. For poly-crystalline metals, there will be a mass of separate crystals irregular in shape but interlocking with each other in a sample of metal. The interface between two crystallite/grains is called the grain boundary. For single crystal metals, the entire sample is a continuous and unbroken crystal lattice without any grain boundaries. Inside a crystal, faults or distorted regions or in other words crystallographic defects are named dislocations. Slip is the process of movement of dislocations under an applied stress. Grain boundaries stop the dislocation movements through the material when the material is subjected to external forces and therefore it is able to increase the strength of material by reducing its grain size.

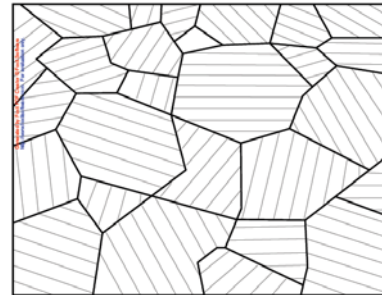


Figure 1 Schematic of grain boundaries and related randomly arranged crystal planes [3].

3 THE MECHANISM OF CRACK INITIATION AND CRACK PROPAGATION IN THE MODES OF FAILURE OF METALLIC MATERIALS

3.1 BRITTLE AND DUCTILE FRACTURE

3.1.1 Crack formation

Micro-cracks in the metal can be formed by the result from the presence of minute inclusions. The inclusion is usually strong and hard to shear therefore at the interface between metal and inclusion a minute fissure will develop when slip in the metal occurs and dislocations pile up at the metal/inclusion interface. Micro-cracks can also be formed in the case a grain boundary stops the movement of dislocations therefore a pile-up will happen and a micro-crack is created (Fig 2). Another way to initiate a crack is due to the movement of dislocations along close-packed or other planes within a crystal.

Contact author: Hoang Van Thang

City University London, U.K.
Email: hvanthang@gmail.com

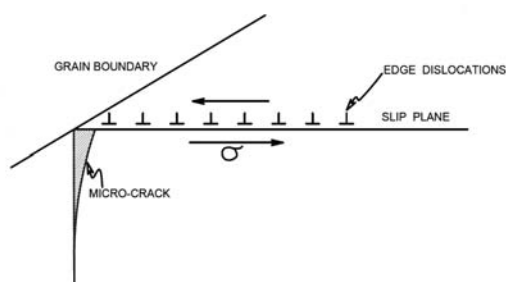


Figure 2 Crack formation at a grain boundary [1].

The crack will be initiated by the pile up of these dislocations at the intersections of slip planes [1].

3.1.2 Brittle fracture

Brittle fracture refers to the fracture without or very limited plastic deformation, cracks run rapidly through a stressed metal. While in ductile fracture occurs with a large amount of plastic deformation [4]. Brittle fracture happened when the atoms are separated completely and suddenly. The tests with identical specimens have shown that the necessary stresses for such separation are very variable and relatively small to the theoretically-calculated value. Therefore there may be some factor influencing the test results. In 1920, A. A. Griffith suggested that from minute flaws the brittle fractures were propagated in brittle solids. He also presented that in his tests the freshly-drawn glass fibres had the strength nearly to the theoretical value and that when the diameter of the fibre decreases then the fracture stress increases. However the strengths of the fibres would be significantly decreased if these fibres contacted with another substance or the atmosphere. This gives a suggestion that surface perfection has considerable role on the strength of glass fibre and that the glass fibre would be weakened if minute surface irregularities are present.

For brittle metals these principles are also applied that mean the existence of microscopic flaws in the metals cause low fracture strength and the size-dependence of strength in metals. According to [1] Griffith has also found that at tip of a crack the applied tensile stress will generate a stress concentration and the relation between the applied tensile stress S and the concentrated stress S_c are:

$$S_c = 2S\sqrt{\frac{c}{r}} \quad \text{or} \quad \frac{S_c}{S} = 2\sqrt{\frac{c}{r}} \quad (1)$$

In which c is the width of the crack and r is the radius of curvature of the crack tip. For example the crack with the width of 10^{-4}m and the tip radius of 10^{-10}m then the ratio of S_c/S will equal 2.10^3 . This means that the concentrated stress at crack is greater than the applied stress in thousand times. Otherwise for a constant of applied tensile stress S when a crack propagates in a brittle material the value of S_c/S will continuously increase because the value of c is increased. Therefore the failure surely happens.

In the case of compression, the applied compressive stress will transmit through the cracks and tend to close up present fissures. The failure finally happens because the high compressive forces generate tensile components

enough magnitude to create failure along crystallographic planes in the fissure region.

Brittle fractures can happen because of cleavage along trans-crystalline planes and by crack propagation along grain boundaries. In the latter case the fracture is termed inter-crystalline fracture. The attendance of grain boundary films of a rigid brittle second phase in some cases could cause this type of fracture.

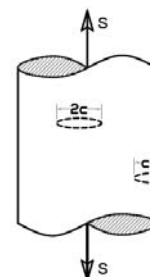


Figure 3 Tensile stress on a brittle fracture [1].

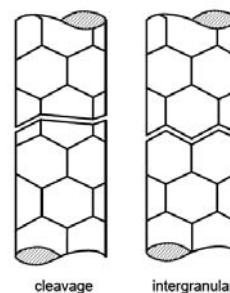


Figure 4 Trans-crystallite and inter-crystallite brittle fracture [4].

Cracks in brittle fracture run nearly perpendicular to the applied stress. This leads to the surface of breaking is quite flat. In addition, the surfaces of fracture of metals usually have a pattern. This pattern could be lines and ridges that starts from the crack origin and spreads out on the surface of crack. In some another metals such as steels have pattern of chevrons or V shape [2].

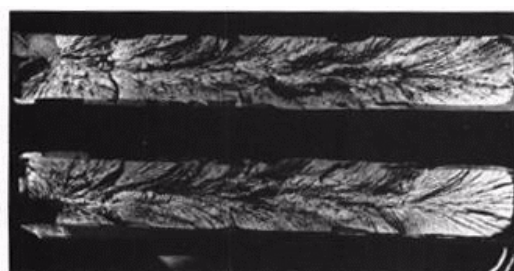


Figure 5 Chevron Fracture Surface [2].

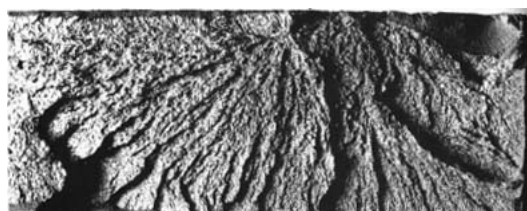


Figure 6 Radiating Ridge Fracture Surface [2].

3.1.3 Ductile fracture

For ductile metals, the fracture happens along with large amounts of plastic deformation. The crack tip radius is likely to increase when the plastic deformation starts occurring and thus the concentrated stress S_c in the Griffith's automatically decrease. The fracture only happens by increasing the loads to make additional strain. This process is called strain hardening. The fracture of almost all ductile poly-crystalline materials usually follows the formation of a neck. Crack starts at the neck centre on a plane nearly perpendicular to the axis of the applied stress. From the starting point, the crack spreads out toward the test sample edges. The fracture finally happens rapidly along a surface, making with the axis of the stress an angle of about 45° .

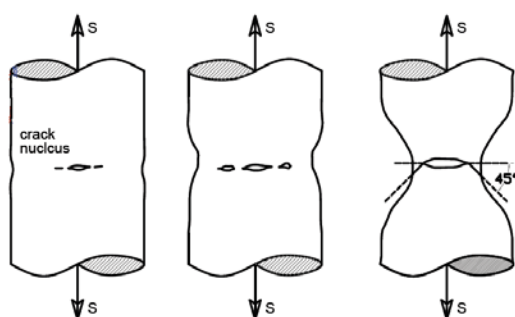


Figure 7 The nucleation and development of a crack in a ductile material [1].

In the case that inclusions are present in the metals, voids/micro-cracks are usually initiated at inclusions. Ductile fracture will follow the grain boundaries or, in other words, fracture is intergranular ductile fracture if the inclusion density is higher on grain boundaries than within the grains. However, ductile fracture usually running through grains that is called trans-granular ductile fracture [4].

3.2 FATIGUE

Fatigue is a common failure in metals. Fatigue occurs when cyclic loading is applied to a metal. For this type of failure, maximum stresses are less than the tensile stress, and may be less than the yield stress of the metal. The relationship between the cyclical stress (S) and the number of cycles to failure (N) is shown in S-N curve. The cyclic stress corresponding to an infinite number of cycles to failure is called the fatigue limit S_D . Fatigue that happens in a corrosive environment is called corrosion fatigue. It is the result of combination between corrosion and repeated cyclic loads that leads to the mechanical degradation of the metal. The failure of metals with high strengths such as steels, aluminium alloys and titanium alloys usually has significant contribution of environmental action. The S-N curve in the case of corrosion fatigue has no fatigue limit and the endurance limit SN is applied instead. The endurance limit is the maximum stress that a metallic material subjected to corrosion fatigue can sustain for a specific number of stress cycles N .

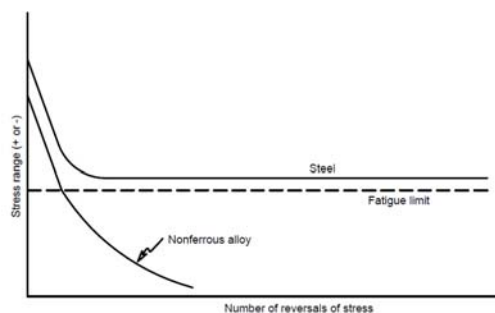


Figure 8 S-N curve and fatigue limit [5].

In fatigue failure the cracks start making up at some point on the outside surface and afterwards propagate gradually into the material in a direction nearly normal to the main tensile axis. This makes the cross-sectional area reduce and reduces the loading withstanding capacity of the material. The fatigue failure finally has to occur. During each loading cycle, a fatigue crack "front" develops a very small increment shown as a minute ripple line on the fracture surface. From the original point of crack, the ripple lines will spread out as a series of concentric arcs.

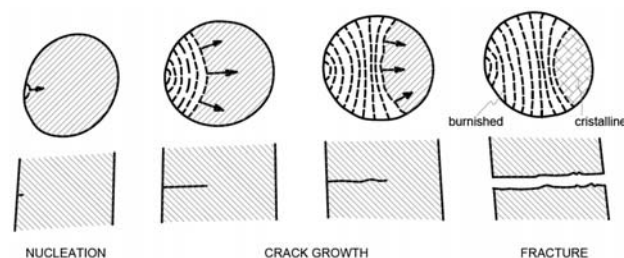


Figure 9 The progress of fatigue failure [1].

It can be seen that the development of fatigue failure includes three periods. These are nucleation, crack growth and ultimate catastrophic failure. As the crack propagation is in a very gradual way and the nature of the fatigue load is pulsating then the two fractured surfaces rub with each other and get burnished. Ultimate fracture of the component is due to the remaining undamaged cross section no longer has the capacity to withstand the loads. This occurs in a very rapid way without rubbing between two surfaces and therefore two fractured surfaces are in crystalline appearances. According to [4] details for fatigue design are given in BS 5400: Part 10. They are grouped in eight categories of B, C, D, E, F, F2, G and W. For welded joints there will be at least five potentials for fatigue cracks to develop. These locations are at two ends, at the weld toe in each of the two parts jointed and in the weld itself. Fatigue cracks in plain steel initiate at the surface either at irregularities on the surface or at corners of cross-sections. However, if welds are present, fatigue failure will commonly happen at the welds because the welded joints have much lower fatigue strength. In steel with regions of stress concentration such as at rivets or bolt holes, fatigue failure will normally start at these stress concentration.

Another case of fatigue is fretting fatigue in which due to fluctuating loads there will be a small displacement (5-50 μm) happens to mechanical components that should be in contact without error. This early crack initiation reduces the fatigue properties. An example for this type of fatigue is in the dovetail joint.

3.3 CREEP

Creep is another type of failure of metals. However, creep occurs during a long period of time when the metals are subjected to the stresses that are smaller than the yield strength of the material. Creep will increase with increasing of temperature and will be very dangerous if the metal is stood with the heating near its melting point. Creep fracture in metallic materials develops in three stages: primary, secondary and tertiary creep. In the stage of primary creep, strain happen in a relatively rapid way. For secondary creep, strain is in a slower rate than in first stage and for tertiary creep, strain rate increases again and fracture finally happens.

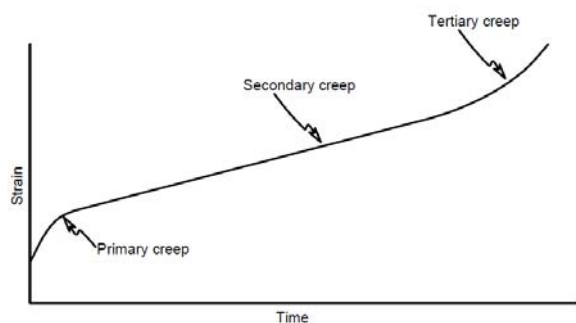


Figure 10 Three stages in creep fracture [5].

The mechanism of creep can be explained as follows: In the primary stage of creep deformation occurs quickly because of the movement of dislocations. However these dislocations soon pile-up at various barriers and the creep rate is decreased (work hardening). This is the secondary stage of creep. However at a high enough temperature dislocation movement can surmount some barriers and this process is called “dislocation climb” and the secondary stage continue occurring. When a large amount of dislocations concentrates at grain boundaries micro-cracks appear and the final failure happens. This is the tertiary of creep.

3.4 CORROSION

The metals can also be in failure due to chemical reactions with its ambient environment. For this type of failure, corrosion is named. The corrosion of metals may be divided into *dry corrosion* and *wet corrosion*. Dry corrosion is the oxidation happening at elevated temperatures while wet corrosion needs the presence of an electrolyte (a solution containing free ions) to happen [5]. In the dry oxidation, the oxidation process immediately recommend when the metal is exposed to the air. The covalent-type bonds are established at the contact surface of the metals and oxygen and result in oxide films.

The oxide film grows much more quickly at high temperature. Outside films tend to crack and fresh metal continue being exposed to the air and the oxidation is continued [3]. For wet corrosion results from a tendency of ionization (dissolution) of metals as metals are place in an electrolyte. This ionization process may be represented as:

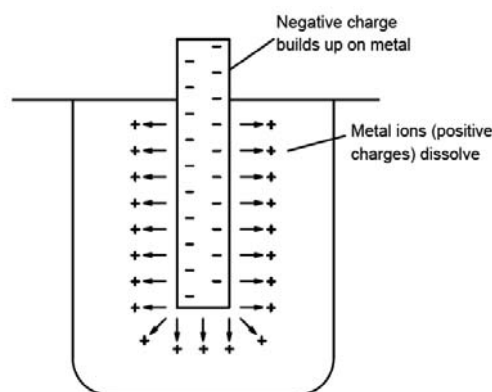
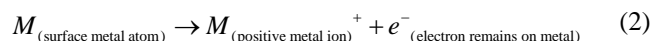
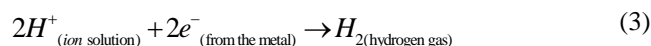


Figure 11 Tendency for metals to dissolve in water[3].

When the positive metal ions dissolve into the solution the metal becomes negatively charge because the electrons remain on it. The process continues until the negative charge is enough to stop further positive ions escaping from the metal. This value of negative charge of the metal is called electrode potential [3]. The corrosion will only continue if electrode potential is reduced to allow more positive ions to leave the metal. In acidic corrosion, this can be done by hydrogen ions presenting in solution:



At the point of corrosion, hydrogen gas is given off and the bubbles may be visible. Electrolytic corrosion happens when two metals with different electrode potentials are immersed in the same electrolyte and are electrically connected. In Table I the metals below hydrogen have smaller tendency than hydrogen to dissolve (ionize) into the solution whereas other metals above hydrogen have greater tendency than it to dissolve. The metal with more negative electrode potential is called the “anode” and is attacked. Another which has the more positive electrode potential is called the “cathode”. The cathode remains un-attacked and depending on the nature of cathode metal, the solution and the presence of dissolved oxygen in the solution the reaction at the cathode may be deposition of metal or formation of OH⁻ hydroxyl ions or liberation of hydrogen [5]. In the example shown in Figure 12, zinc is the anode while copper has the role of the cathode. It is necessary to note that corrosion rates increase with the increasing of the temperature because when the temperature is raised then thermal energy is increased and therefore all chemical activities are accelerated.

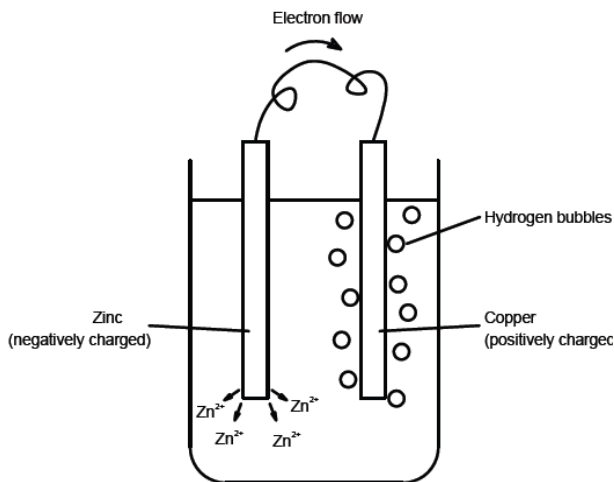


Figure 12 Electrolytic corrosion resulting from zinc and copper rods immersed in aqueous solution [3].

Table I - Standard electrode potentials of pure metals [3].

<i>Metal</i>	<i>Electrode potential (V)</i>
Magnesium	-2.4
Aluminium	-1.76
Zinc	-0.76
Chromium	-0.65
Iron (ferrous)	-0.44
Nickel	-0.23
Tin	-0.14
Lead	-0.12
Hydrogen (reference)	0.00
Copper (cupric)	+0.34
Silver	+0.80
Gold	+1.4

CONCLUSIONS

The above has mentioned about crack initiation and its propagation in different modes of failures in metallic engineering materials. The structure of metals, the temperature and surrounding environmental conditions and loading conditions play important roles in the crack initiation and propagation of metals. The understanding of the mechanism of the crack in metals can help to prevent it. For example in the case of corrosion, it can be seen that wet corrossions can be stopped by keeping the metal dry by coatings. To avoid human and material losses caused by failures in metals, it is necessary to study about the crack of metals carefully to have solutions for protecting the metal.

REFERENCES

- [1] Higgins R.A., *Engineering Metallurgy*. Hodder and Stoughton, London, 1983.
- [2] Callister W.D., *Materials Science and Engineering: An Introduction*. John Wiley & Sons, New York, 2007.
- [3] Taylor. G.D., *Materials in Construction*. Longman, Harlow, 2000.
- [4] Simpson R., *Steel Designer's Manual*. Blackwell Scientific Publications, Oxford, 1992.
- [5] University of Dundee, *Civil Engineering Materials*. Macmillan, London, 1976.

AN UNDERACTUATED FINGER FOR A ROBOTIC HAND

Francesco Penta Cesare Rossi Sergio Savino

Dipartimento di Ingegneria Industriale, Università di Napoli – “Federico II”- Napoli, Italy

ABSTRACT

In the paper a study on an underactuated finger for a robotic hand is presented. The mechanical hand, of which the finger is a part, is an underactuated device made of five fingers, each one having three phalanxes, operated by non-extendible tendons; thus it can be used both as robot grasping end-effector and as human prosthesis.

The mechanical behavior of the finger was studied by means of an energetic or variational approach. The latter model permits an easier computing of the constraint reaction applied to the tendon end when the displacement is imposed.

Results are presented obtained both by the proposed model and by a simulation multilink code.

Finally an early experimental prototype is also shown.

Keywords: Mechanical finger, Robotic Hand, Hand Prosthesis, Gripper

1 INTRODUCTION

The gripping tasks are the ones that most have been assigned to automated systems, and are always a field of study and investigation in order to achieve even better performance.

A poor adaptability to the geometric characteristics of the object does not guarantee the maintenance of the grip in the presence of external disturbances (weight force, inertia forces, sudden loads, etc.). Whereby the grip may not be stable. The deficiency of degrees of freedom results in the inability on the part of the hand, to wrap around the grasped object during a generic task of taking.

If the geometric characteristics of the robotic hand remain unchanged whatever the object that you want to grab, it follows that the area of contact between the object and the hand is limited, therefore the hand in general must exert greater grip forces to ensure a grip stable.

So, the problem is to obtain an articulated movement of the fingers, able to adapt to the generic form of the object, although it has no a high number of actuators able to govern the various d.o.f.

A solution is to use a particular type of mechanisms: the mechanisms under-actuated in which some active joints are replaced by springs or mechanical stops.

Underactuated mechanisms are mechanical systems with fewer control inputs than degrees of freedom [1].

These mechanisms are often employed in mechanical systems in order to allow for the passive accommodation of environmental constraints and disturbances while reducing sensing and hardware complexity.

In the field of prosthetic hands, underactuated mechanisms have been significantly applied, and many projects have been developed in recent years, [2-5]. The hand prostheses are designed primarily for gripping tasks while maintaining a high ease of control. For this reason the use of underactuated mechanisms was always greater. In the field of robotic hands, the research has produced several sophisticated mechanical hands, [6], but with a great number of actuators and a complex control system. In recent studies underactuated mechanisms have been increasingly used in projects of robotic hand.

Underactuated finger mechanism is beneficial in the anthropomorphic applications in which it reduces the finger size, weight and power consumption due to the less number of actuators compared to its number of degree of freedom.

Anthropomorphic hand finds its application in humanoid robots and prosthetic hands.

Most of the research on underactuated mechanism is limited to grasping function only such as in [7-8]. Human finger can also pinch with the fingertip to hold an object like holding a pencil during writing or to handle other small and thin items, as proposed in [9]. Obviously more researches are implemented to study the ability of an

Contact author: Cesare Rossi

E-mail: cesare.rossi@unina.it

underactuated mechanism to passively adapt to environmental constraints, [10].

The design choices are made based on a prototype of an underactuated robotic hand with a tendon driven actuation system and implemented with differential mechanisms [11-13].

The main subsystem of such a hand is the finger which, like the human, is constituted by three phalanges joined by fork joints and moved by an actuator tendon and a recalling tendon.

2 THE UNDERACTUATED ROBOTIC HAND

In the figures 1 and 2 the design of the robotic hand is shown. It essentially consists in simple elements that guarantee the cheapness and simplicity of operation. In particular, the hand is composed by five fingers, each made of three phalanxes hinged to each other by linchpins, which represent the different articulations of a human finger. The finger is closed by means of an inelastic tie-rod as shown in figure 2.

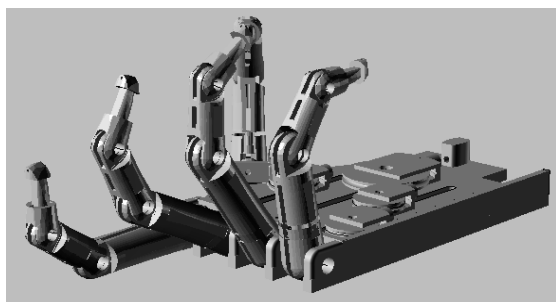


Figure 1 Prospective view of the hand mechanism

The five fingers constituting the human hand prosthesis (or, generally the grasping device), are fixed on a base. The inelastic tie rod, passing through distribution pulleys distributes the gripping tension between the thumb and index finger. In this way, the gripping tension is distributed between the fingers.

Since the tendons are inelastic, the pulley mechanism will permit the fingers to adjust themselves to the grasped object size and shape.

The rotation of the pulleys, in fact, will occur at any contact of each phalanx with the gripped object. Once each phalanx enters into contact with the gripping object, the finger is aligned in such a way to tighten the object and ensure its grip. Thanks to the larger pulleys installed on the palm of the hand, the force is distributed also to the other fingers; the set will move up until each phalanx is in contact with the object to be taken, achieving the gripping.

The repartition of the actuating force F allows to reach a configuration in which for each finger the force is:

- $F/4$ on thumb;
- $F/4$ on index;
- $F/4$ on middle finger;
- $F/8$ on ring finger;
- $F/8$ on little finger.

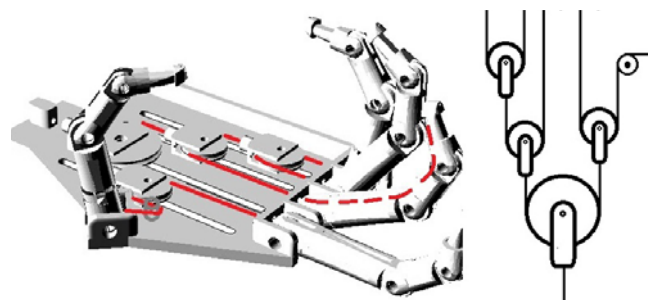


Figure 2 Prospective view and working principle of the hand mechanism

The tendon flows within the three phalanges and its traction generates the winding of the finger itself around the object to grasp. When one of the phalanges meets the object that obstructs the movement, the other phalanges, under the action of the actuator tendon, continue to fold.

When the grip of the finger is completed, and all the phalanges collide against the object, the system of differential mechanisms transfers the movement only to the other elements that can still move. Such a solution provides a secure grip of the objects.

Finally some springs will permit to each of the fingers to loosen the grip when the actuator is released.

In conclusion thanks to this particular pulley system, that allows the fingers to adjust themselves to the object shape, the 15 d.o.f. mechanism is moved by a single actuator.

2.1 THE FINGER

The finger is, naturally, one of the main components of the hand. The evaluation of the phalanxes rotation during the gripping as a function of the tendon displacement is, of course, the first goal to be achieved in order to design the entire hand.

The finger model can be obtained starting from geometrical considerations as in [12] or by means of an energetic or variational approach as proposed in the following. The latter model permits an easier computing of the constraint reaction applied to the tendon end when the displacement is imposed.

The behavior of a single tendon finger made of rigid phalanxes mutually constrained by hinges can be modeled by the plane holonomic system reported in fig. 3.

Its Lagrangian coordinates are identified in the relative rotations between each couple of consecutive phalanxes and in the absolute rotation of the proximal one.

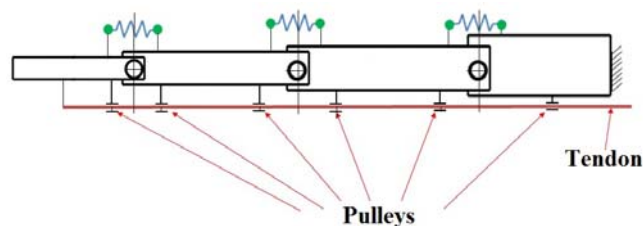


Figure 3 – Scheme of the finger.

To study the system equilibrium by the proposed energetic or variational approach, both the displacement u of the tendon end and the springs elongations have to be expressed as function of the coordinates φ_i .

We assume that the tendon is inextensible and has zero bending stiffness. When the system, starting from the reference or initial configuration ($\varphi_i = 0$), reaches the generic configuration labeled by the coordinates vector $\boldsymbol{\varphi} = [\varphi_0, \varphi_1, \varphi_2]$, the tendon end moves by

$$u = L_0 - \sum_{i=0}^n z_i, \quad (1)$$

where z_i is the actual length of the free tendon path between the consecutive phalanx i and $i+1$ (fig. 4) and L_0 is the sum of the free paths z_{0i} in the reference configuration.

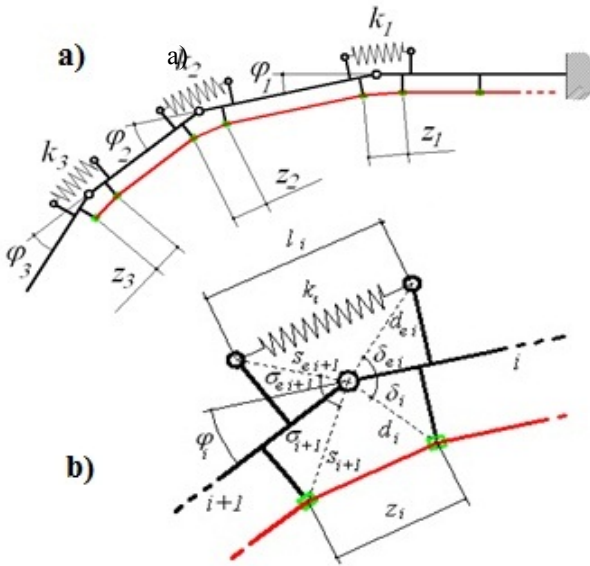


Figure 4 Deformed configurations of the finger (a) and of the phalanxes i and $i+1$ (b).

In fig. 4b) the deformed configuration of a couple of consecutive phalanxes is schematically shown together with the phalanxes geometric parameters defining the actual value of z_i . Being the distances d_i and s_{i+1} fixed for any system configuration $\boldsymbol{\varphi}$, the path length z_i varies only with the relative rotation φ_i according to:

$$z_i = \sqrt{d_i^2 + s_{i+1}^2 - 2d_i s_{i+1} \cos(\Phi_{0i} - \varphi_i)}, \quad (2)$$

with $\Phi_{0i} = \pi - (\delta_i + \sigma_{i+1})$, where δ_i and σ_{i+1} are the angles that d_i and s_{i+1} make respectively with the axes of the phalanxes i and $i+1$.

For the elongations of the elastic elements, similar consideration to those made for the path lengths z_i can be made. Denoting by d_{ei} and s_{ei+1} the fixed distances of the spring ends from the hinge center and by δ_{ei} and σ_{ei+1} the angles that d_{ei} and s_{ei+1} make respectively with the phalanxes axis i and $i+1$, the actual length of the spring is given by:

$$l_i = \sqrt{d_{(e)i}^2 + s_{(e)i+1}^2 - 2d_{(e)i} s_{(e)i+1} \cos(\Phi_{(e)0i} - \varphi_i)}, \quad (3)$$

where $\Phi_{(e)0i} = \pi - (\delta_{(e)i} + \sigma_{(e)i+1})$, and the actual elongation of the spring i is

$$\Delta l_i = l_i - l_{0i}, \quad (4)$$

with l_{0i} spring initial length.

From eq (1) and (2), it is easily desumed that, when a virtual increment $d\varphi_i$ of the Lagrangian coordinate φ_i takes place, we have the following virtual change of the tendon end displacement u :

$$du_i = -dz_i = \frac{d_i s_{i+1} \sin(\Phi_{i0} - \varphi_i)}{\sqrt{d_i^2 + s_{i+1}^2 - 2d_i s_{i+1} \cos(\Phi_{0i} - \varphi_i)}} \cdot d\varphi_i. \quad (5)$$

Furthermore, for any $d\varphi_i$ we observe only virtual changes of the elongation Δl_i of the spring i , the expression of which is obtained differentiating eq. (3):

$$d(\Delta l_i) = dl_i = \frac{d_{(e)i} s_{(e)i+1} \sin(\Phi_{(e)0i} + \varphi_i)}{\sqrt{d_{(e)i}^2 + s_{(e)i+1}^2 - 2d_{(e)i} s_{(e)i+1} \cos(\Phi_{(e)0i} + \varphi_i)}} \cdot d\varphi_i. \quad (6)$$

If the finger is operated by controlling the tendon displacement u , its equilibrium configuration $\boldsymbol{\varphi}$ has to satisfy the stationary condition of the elastic strain energy E , that is:

$$dE = d\left(\sum_{i=0}^n \frac{1}{2} K_i \varphi_i^2\right) = \sum_{i=0}^n K_i \cdot \varphi_i \cdot d\varphi_i = 0 \quad \forall d\varphi_i, \quad (7)$$

with K_i stiffness of the spring i , and the following constraint equation for u :

$$g(\boldsymbol{\varphi}) = u(\boldsymbol{\varphi}) - \bar{u} = L_0 - \sum_{i=0}^n z_i - \bar{u} = 0, \quad (8)$$

where \bar{u} is the prescribed value of the u displacement.

To solve the equilibrium problem defined by eq. (7) and (8), we follow the Lagrange multiplier method. Solution of (7) and (8) is equivalent to searching for the stationary point of the function $\bar{E}(\boldsymbol{\varphi}, \lambda)$ given by:

$$\bar{E}(\boldsymbol{\varphi}, \lambda) = E(\boldsymbol{\varphi}) - \lambda \cdot g(\boldsymbol{\varphi}), \quad (9)$$

where λ is an unknown Lagrange multiplier. By differentiating previous equation with respect to the Lagrangian coordinates φ_i and equating the result to zero, the following set of equilibrium conditions is obtained

$$K_i \cdot \Delta l_i \cdot \frac{d\Delta l_i}{d\varphi_i} - \lambda \frac{\partial g}{\partial \varphi_i} = 0, \quad i = 0, 1, \dots, n, \quad (10)$$

whose solution has to verify also the constraint equation (8). On the other hand, by differentiating this latter with respect to φ_i and taking account of eq(5), we have:

$$\frac{\partial g}{\partial \varphi_i} = \frac{\partial u}{\partial \varphi_i} = \frac{du_i}{d\varphi_i} = -\frac{dz_i}{d\varphi_i}. \quad (11)$$

Substituting this result in the eq (5) after having multiplied it by $d\varphi_i$, the following identity is obtained between the strain energy change of the spring i and the virtual work of λ :

$$K_i \Delta l_i \frac{d(\Delta l_i)}{d\varphi_i} \cdot d\varphi_i = \lambda \cdot du_i; \quad (12)$$

since, for any $d\varphi_i$, λ does virtual work due to the displacement du_i , it can be identified as the constraint reaction applied to the tendon end when the displacement \bar{u} is imposed.

3 EXAMPLES OF THE RESULTS

By means of the model presented above, a number of computations were made, some are presented in the following. Then a model by a multilink simulation code was also built in order to verify the previous results. Finally a working prototype was built to test the entire system.

3.1 COMPUTED RESULTS

In fig. 5 the results computed by the proposed model are reported. In the figure the rotation of the phalanxes are plotted versus the tendon displacement. Since the latter depends on the length of the phalanxes, it was reported as non-dimensional respect to the 2nd phalanx length.

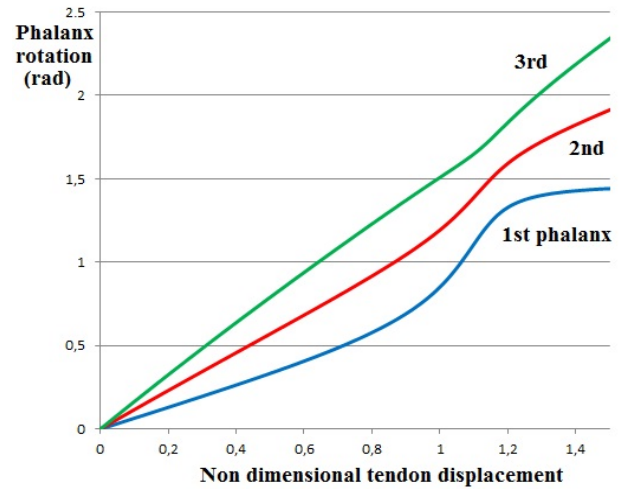


Figure 5 Rotation of the phalanxes versus the tendon displacement.

In figure 6 the force exerted from the tendon versus the tendon displacement is reported.

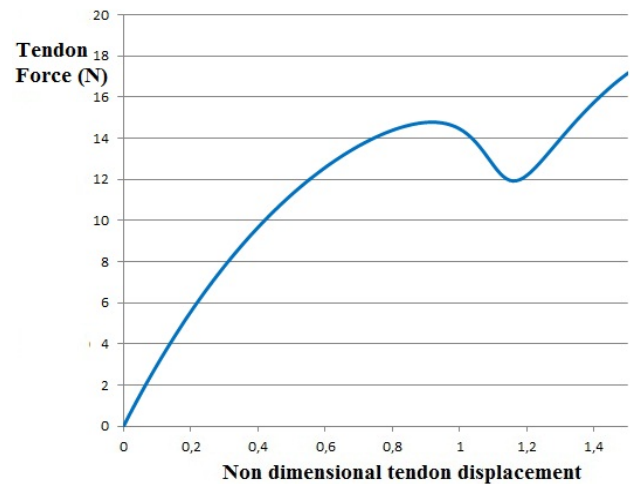


Figure 6 Tendon displacement versus the tendon displacement.

The latter represents an example since the force obviously depend on the springs stiffness and on the length of the phalanxes, while the shape of the curve strongly depends on the kinematics, hence on the position of the hinges, of the tendon pulleys and of the springs ends.

3.2 SIMULATION RESULTS

In fig.7 a view of the multilink model is shown; the latter was made by Working Model 2DTM. It is essentially made by three rigid bodies linked by hinges; three springs simulate the stiffness of the elements that represent the devices that will extend the finger when the tendon is released; finally a pulley system will schematize the tendon. In the figure a finger configuration achieved with about $\frac{3}{4}$ of the tendon displacement is shown; for comparison, the finger extended in the reset position is also reported.

In the same figure a diagram showing the rotation of each of the three phalanxes versus the tendon displacement is also reported.

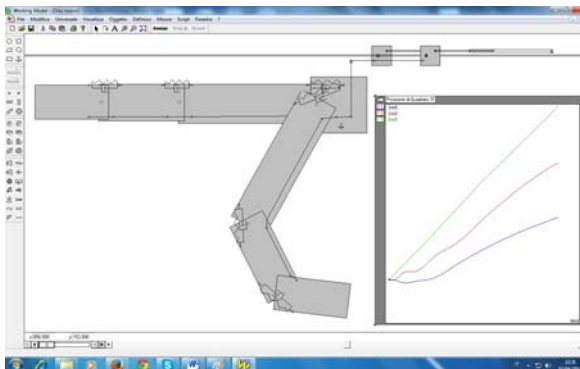


Figure 7 WM 2D™ Model.

How it is possible to observe, the results obtained by means of the simulation practically coincide with those computed that are reported in the previous paragraph.

3.3 EARLY PROTOTYPE

A first prototype was designed and built in order to verify the practical feasibility of both the underactuated finger and the whole device. In the figures 1 and 2 the CAD assembly was already reported, while in the figures 8 and 9 the first prototype is shown.

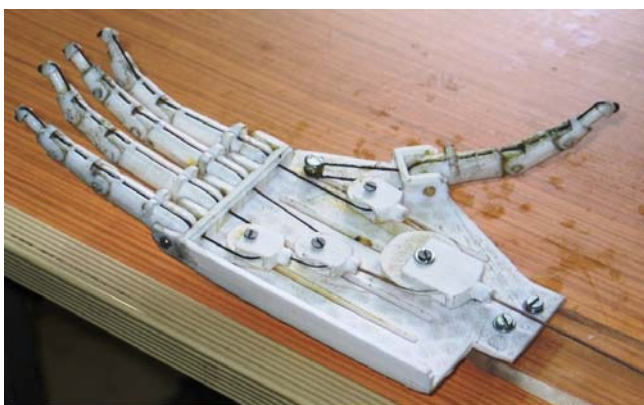


Figure 8 First prototype.

In the upper part of figure 8 the hand with the fingers completely released is reported while in the lower part the fingers are completely clamped.

In figure 9, the hand prototype grasping a rather complex object is shown; the latter is represented by a trigger operated spray bottle. In the lower part of the figure a particular of the finger wrapping is shown.

How it is possible to observe, despite the one presented is just a first prototype, so that many particulars should be still tuned up, the grasping of the object is already rather satisfactory. Moreover, from the figure it is possible to observe that the bottle is lifted from the table and all is operated just by the wire connected to the larger pulley. Finally, it can be observed how the index finger can rather easily operate the trigger of spray bottle.



Figure 9 Grasping of a spray bottle.

CONCLUSIONS

A model, based on a variational approach, of an underactuated finger operated by non-extendible tendons was presented. The latter is conceived as a part of an underactuated grasping device that can be used as a robotic grasping tool or an human hand prostheses and permits an easier computing of the constraint reaction applied to the tendon end when the displacement is imposed.

The mechanical behavior of the finger was studied by means of the proposed model and the results practically are in good agreement with those obtained by means of a multilink model made by Working Model 2D™.

A first prototype of the human hand prostheses is also presented, showing encouraging results for what the practical feasibility of the device is concerned.

REFERENCES

- [1] He Bin Liu Wen Zhen ; Lv Hai Feng. A Survey on Underactuated Mechanisms, *Advanced Computer Control (ICACC)*, 2010, 2nd International Conference on, Volume 4, pp 551 – 555.
- [2] Massa B., Roccella S., Carrozza M.C., Dario P., 2002. Design and Development of an Underactuated Prosthetic Hand, *Proceeding of the 2002 IEEE International Conference On Robotics and Automation*, Washington DC, May 2002.
- [3] Roccella S., Carrozza M.C., Cappiello G., Dario P., Cabibihan J.J., Zecca M., Miwa H., Itoh K., Matsumoto M., Takanishi A., 2004. Design, fabrication and preliminary results of a Novel anthropomorphic hand for humanoid robotics: RCH-1, *Proceedings of 2004 IEEE/RSJ International Conference on Intelligent Robots and Systems*, Sendai, Japan, September 28 - October 2, 2004.
- [4] S. Roccella, M.C. Carrozza, G. Cappiello, J.J. Cabibihan, C. Laschi, P. Dario, H. Takanobu, M. Matsumoto, H. Miwa, K. Itoh, A. Takanishi, 2007. Design and Development of Five-Fingered Hands for a Humanoid Emotion Expression Robot, *International Journal Of Humanoid Robotics*, 2007, n. 4, pp. 181-206.
- [5] Cipriani C., Controzzi M., Carrozza M. C., 2011. The Smart Hand Transradial Prosthesis, *Journal Of Neuroengineering And Rehabilitation*, 2011, n. 8.
- [6] Grebenstein M., Chalon M., Hirzinger G., and Siegwart R., 2010. Antagonistically Driven Finger Design for the Anthropomorphic DLR Hand Arm System. *IEEEERAS International Conference on Humanoid Robots* Nashville, TN, USA, December 6-8, 2010.
- [7] Laliberte, T. and C.M. Gosselin, 2001. Underactuation in space robotic hands. *Proceeding of the 6th International Symposium on Artificial Intelligence and Robotics and Automation in Space*, June 18-22, Canadian Space Agency, St-Hubert, Quebec, Canada, pp. 1-8.
- [8] Laliberte T., Birglen L., and C. M. Gosselin, 2002. Underactuation in robotic grasping hands. *Machine Intelligence & Robotic Control*, Vol. 4, No. 3.
- [9] Norsinnira Zainul Azlan and Yamaura Hiroshi, 2010. Underactuated Anthropomorphic Finger Mechanism for Grasping and Pinching with Optimized Parameter. *Journal of Computer Science*, vol 6, pp. 928-933.
- [10] Balasubramanian R. and Dollar A. M., 2011. A Comparison of Workspace and Force Capabilities between Classes of Underactuated Mechanisms. *2011 IEEE International Conference on Robotics and Automation Shanghai International Conference Center*, May 9-13, 2011, Shanghai, China.
- [11] Fiore P., Niola V., Pisani G., Rossi C., Savino S., Troncone S., 2013. A model of a robotic hand based on a tendon driven mechanism, *Proc. of 22th International Workshop on Robotics in Alpe-Adria-Danube Region*, Portorož, Slovenia, September 11-13, 2013.
- [12] Rossi C., Savino S., 2013. Mechanical Model of a Single Tendon Finger, *Proc. of ICNAAM 2013: 11th International Conference of Numerical Analysis and Applied Mathematics*, Rhodes, Greece, Sep 21-27, 2013.
- [13] Rossi C., Savino S. A Study of a Robotic Hand with Tendon Driven Fingers. *Robotica*, ISSN: 0263-5747, in press.

TEMPLATE FOR PREPARING PAPERS FOR PUBLISHING IN INTERNATIONAL JOURNAL OF MECHANICS AND CONTROL

Author1* Author2**

* affiliation Author1

** affiliation Author2

ABSTRACT

This is a brief guide to prepare papers in a better style for publishing in International Journal of Mechanics and Control (JoMaC). It gives details of the preferred style in a template format to ease paper presentation. The abstract must be able to indicate the principal authors' contribution to the argument containing the chosen method and the obtained results. (max 200 words)

Keywords: keywords list (max 5 words)

1 TITLE OF SECTION (E.G. INTRODUCTION)

This sample article is to show you how to prepare papers in a standard style for publishing in International Journal of Mechanics and Control.

It offers you a template for paper layout, and describes points you should notice before you submit your papers.

2 PREPARATION OF PAPERS

2.1 SUBMISSION OF PAPERS

The papers should be submitted in the form of an electronic document, either in Microsoft Word format (Word '97 version or earlier).

In addition to the electronic version a hardcopy of the complete paper including diagrams with annotations must be supplied. The final format of the papers will be A4 page size with a two column layout. The text will be Times New Roman font size 10.

2.2 DETAILS OF PAPER LAYOUT

2.2.1 Style of Writing

The language is English and with UK/European spelling. The papers should be written in the third person. Related work conducted elsewhere may be criticised but not the individuals conducting the work. The paper should be comprehensible both to specialists in the appropriate field and to those with a general understanding of the subject. Company names or advertising, direct or indirect, is not permitted and product names will only be included at the discretion of the editor. Abbreviations should be spelt out in full the first time they appear and their abbreviated form included in brackets immediately after. Words used in a special context should appear in inverted single quotation mark the first time they appear. Papers are accepted also on the basis that they may be edited for style and language.

2.2.2 Paper length

Paper length is free, but should normally not exceed 10000 words and twenty illustrations.

2.2.3 Diagrams and figures

Figures and Tables will either be entered in one column or two columns and should be 80 mm or 160 mm wide respectively. A minimum line width of 1 point is required at actual size. Captions and annotations should be in 10 point with the first letter only capitalised *at actual size* (see Figure 1 and Table VII).

Contact author: author1¹, author2²

¹Address of author1.

²Address of author2 if different from author1's address
E-mail: author1@univ1.com, author2@univ2.com

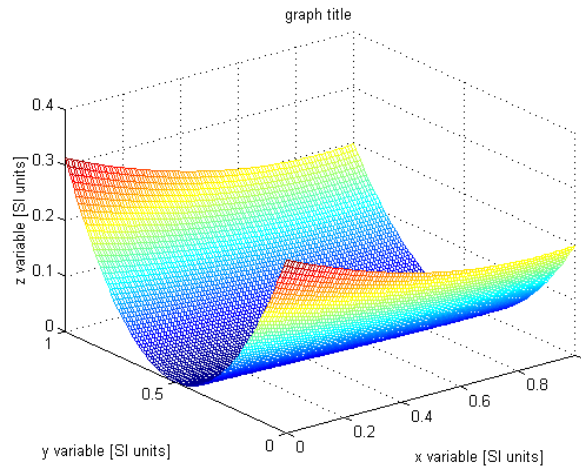


Figure 1 Simple chart.

Table VII - Experimental values

Robot Arm Velocity (rad/s)	Motor Torque (Nm)
0.123	10.123
1.456	20.234
2.789	30.345
3.012	40.456

2.2.4 Photographs and illustrations

Authors could wish to publish in full colour photographs and illustrations. Photographs and illustrations should be included in the electronic document and a copy of their original sent. Illustrations in full colour ...

2.2.5 Equations

Each equation should occur on a new line with uniform spacing from adjacent text as indicated in this template. The equations, where they are referred to in the text, should be numbered sequentially and their identifier enclosed in parenthesis, right justified. The symbols, where referred to in the text, should be italicised.

- point 1
 - point 2
 - point 3
- 1. numbered point 1
- 2. numbered point 2
- 3. numbered point 3

$$W(d) = G(A_0, \sigma, d) = \frac{1}{T} \int_0^{+\infty} A_0 \cdot e^{-\frac{d^2}{2\sigma^2}} dt \quad (1)$$

3 COPYRIGHT

Authors will be asked to sign a copyright transfer form prior to JoMaC publishing of their paper. Reproduction of any part of the publication is not allowed elsewhere without permission from JoMaC whose prior publication must be cited. The understanding is that they have been neither previously published nor submitted concurrently to any other publisher.

4 PEER REVIEW

Papers for publication in JoMaC will first undergo review by anonymous, impartial specialists in the appropriate field. Based on the comments of the referees the Editor will decide on acceptance, revision or rejection. The authors will be provided with copies of the reviewers' remarks to aid in revision and improvement where appropriate.

5 REFERENCES (DESCRIPTION)

The papers in the reference list must be cited in the text. In the text the citation should appear in square brackets [], as in, for example, "the red fox has been shown to jump the black cat [3] but not when...". In the Reference list the font should be Times New Roman with 10 point size. Author's first names should be terminated by a 'full stop'. The reference number should be enclosed in brackets. The book titles should be in *italics*, followed by a 'full stop'. Proceedings or journal titles should be in *italics*. For instance:

REFERENCES (EXAMPLE)

- [1] Smith J., Jones A.B. and Brown J., *The title of the book*. 1st edition, Publisher, 2001.
- [2] Smith J., Jones A.B. and Brown J., The title of the paper. *Proc. of Conference Name*, where it took place, Vol. 1, paper number, pp. 1-11, 2001.
- [3] Smith J., Jones A.B. and Brown J., The title of the paper. *Journal Name*, Vol. 1, No. 1, pp. 1-11, 2001.
- [4] Smith J., Jones A.B. and Brown J., *Patent title*, U.S. Patent number, 2001.

International Journal of Mechanics and Control – JoMaC
Published by Levrotto&Bella
TRANSFER OF COPYRIGHT AGREEMENT

<p>NOTE: Authors/copyright holders are asked to complete this form signing section A, B or C and mail it to the editor office with the manuscript or as soon afterwards as possible.</p>	<p><i>Editor's office address:</i> Andrea Manuello Bertetto Elvio Bonisoli <i>Dept. of Mechanics</i> <i>Technical University – Politecnico di Torino</i> <i>C.so Duca degli Abruzzi, 24 – 10129 Torino – Italy</i> <i>e_mail: jomac@polito.it</i> <i>fax n.: +39.011.564.6999</i></p>
--	---

The article title:

By: _____

To be Published in *International Journal of Mechanics and Control JoMaC*
Official legal Turin court registration Number 5320 (5 May 2000) - reg. Tribunale di Torino N. 5390 del 5 maggio 2000

- A Copyright to the above article is hereby transferred to the JoMaC, effective upon acceptance for publication. However the following rights are reserved by the author(s)/copyright holder(s):
1. All proprietary rights other than copyright, such as patent rights;
 2. The right to use, free or charge, all or part of this article in future works of their own, such as books and lectures;
 3. The right to reproduce the article for their own purposes provided the copies are not offered for sale.
- To be signed below by all authors or, if signed by only one author on behalf of all co-authors, the statement A2 below must be signed.*

A1. All authors:

SIGNATURE _____ DATE _____ SIGNATURE _____ DATE _____

PRINTED NAME _____ PRINTED NAME _____

SIGNATURE _____ DATE _____ SIGNATURE _____ DATE _____

PRINTED NAME _____ PRINTED NAME _____

A2. One author on behalf of all co-authors:

"I represent and warrant that I am authorised to execute this transfer of copyright on behalf of all the authors of the article referred to above"

PRINTED NAME _____

SIGNATURE _____ TITLE _____ DATE _____

B. The above article was written as part of duties as an employee or otherwise as a work made for hire. As an authorised representative of the employer or other proprietor. I hereby transfer copyright to the above article to *International Journal of Mechanics and Control* effective upon publication. However, the following rights are reserved:

1. All proprietary rights other than copyright, such as patent rights;
2. The right to use, free or charge, all or part of this article in future works of their own, such as books and lectures;
3. The right to reproduce the article for their own purposes provided the copies are not offered for sale.

PRINTED NAME _____

SIGNATURE _____ TITLE _____ DATE _____

C. I certify that the above article has been written in the course of employment by the United States Government so that no copyright exists, or by the United Kingdom Government (Crown Copyright), thus there is no transfer of copyright.

PRINTED NAME _____

SIGNATURE _____ TITLE _____ DATE _____

CONTENTS

- 3 An Experimental Test Validation of a New Planetary Transmission**
G. Balbayev, M. Ceccarelli and K. Ivanov
- 9 A Design and Simulation of an Articulated Leg for Hexapod Robots**
N.E. Nava Rodríguez, G. Carbone and M. Ceccarelli
- 23 Parametric Resonance in Cantilever Beam and Energy Harvesting Outlooks**
E. Bonisoli, M. Scapolan and M. Ghandchi Tehrani
- 31 Development of an Environmental Control System Pack Simulation Model for a More Electric Aircraft**
P. Maggiore, M.D.L. Dalla Vedova, L. Pace, M. Tosetti and A. Piovano
- 37 MBSE Modelling Environment and Multi-Objective Optimization of Thermal Control Strategies for Multifunctional Structures**
M. Cencetti, E. Zeminiani, P. Maggiore and M.D.L. Dalla Vedova
- 57 The Mechanism of Crack Initiation and Propagation in Metallic Engineering Materials**
H. Van Thang
- 63 An Underactuated Finger for a Robotic Hand**
F. Penta, C. Rossi and S. Savino

next issue titles will be from the papers of:

RAAD 2014

23th International Workshop on Robotics in Alpe-Adria-Danube Region

Smolenice Castle, Slovakia

3 - 5 September 2014